MICROSTRUCTURE AND SINTERING MECHANISM OF SiC CERAMICS REINFORCED WITH NANOSIZED ZrO₂

Eszter Bódis,[a]* Ádám Fábián,[a] Krisztián Bán,[b] Zoltán Károly, [a] Szilvia Klébert,[a] Anna Mária Keszler,[a] Péter Fazekas,[a] János Szépvölgyi[a]

Silicon carbide-based (SiC) ceramics has attracted quite broad attention due to their excellent mechanical, chemical and thermal properties. However, their widespread industrial application is hindered by difficulties in sintering and poor fracture toughness of sintered bodies. In this work, we present an alternative way to produce SiC-based ceramics with improved microstructure and mechanical properties. We incorporated ZrO₂ nanofibres into the ceramic matrix to achieve a combined reinforcing effect of partially stabilized zirconia, namely fibre and phase transformation strengthening. For comparison, we also prepared silicon carbide ceramics containing yttria stabilized zirconia (YSZ) particles. SiC-based green bodies containing 5, 10 and 15 wt % ZrO₂ nanofibres and particles, respectively, were subjected to spark plasma sintering (SPS) at relatively low (1700 °C) temperatures with high heating and cooling rates. The effects of nanofibres on mechanical properties were studied by determining the Vickers hardness and Young's modulus of sintered ceramics from instrumented indentation tests. The microstructural patterns were investigated, as well.

*Corresponding Authors: Eszter Bódis
　　　E-Mail: bodis.eszter@ttk.mta.hu
[a]　Institute of Materials and Environmental Chemistry, Research Centre for Natural Sciences, Hungarian Academy of Sciences, Magyar tudósok krt 2., H-1117, Budapest, Hungary
[b]　Department of Automobiles and Vehicle Manufacturing, Faculty of Transportation Engineering and Vehicle Engineering, University of Technology and Economics, Műegyetem rkp. 3, H-1111, Budapest, Hungary

Introduction

Silicon carbide-based (SiC) ceramics are considered as a high-performance engineering material because of their low density, high strength (~550 MPa) even at high temperatures, great hardness (~26 GPa), good oxidation resistance, high thermal conductivity (~120 W m^{-1} K^{-1}) and low thermal expansion coefficient ($4·10^{-6}$ K^{-1}).[1] The covalent bonds among constituting atoms result in a very hard and strong material. Therefore SiC-based ceramics are being used in several applications even in extreme condition. However, due to the strong covalent bonds and the low self-diffusion coefficient SiC can be fully sintered only above 2000 °C. To have high density ceramics at lower temperature sintering aids, mainly oxides, are required.[2] Similarly to most ceramics, SiC is also brittle due to its low fracture toughness.[3] Thus, it is essential to incorporate certain reinforcing materials into the SiC matrix. Many studies focus on increasing the mechanical properties of SiC using different ceramic particles[4-5] or more recently carbon nanostructures, like carbon nanotubes (CNT), carbon fibres or graphene sheets.[6-8] However, carbon tends to be oxidized in air at elevated temperatures and it destroys the properties of such ceramics composites.[9] To avoid the degradation of reinforcing materials in air at elevated temperatures and to reach high thermal stability, application of oxide-type reinforcing material seems appropriate.

ZrO₂ ceramics have been widely utilized in harsh environments and load-bearing conditions due to their high fracture toughness (~9.3 MPa·m$^{1/2}$), high melting point (2680 °C), excellent bending strength and good wear resistance. In many ceramic composites zirconia may enhance the fracture toughness by stress-induced, tetragonal (t) to monoclinic (m) phase transformation. Numerous papers have reported on increased mechanical properties of ceramics matrix composites due to incorporation of ZrO₂ particles.[10-12]

In our previous works[13] we reported that ZrO₂ nanofibres were even better reinforcing agents than ZrO₂ particles: addition of ZrO₂ nanofibres to Si₃N₄ matrix significantly improved the fracture resistance of composite as compared to Si₃N₄ monolith. It was explained by the simultaneous phase transformation and fibre toughening of ZrO₂ fibres.

Some papers in the literature have been focused on studying ZrO₂/SiC systems. However, in most cases ZrO₂ was the matrix material, which was reinforced by SiC particles or SiC fibres.[14-17] Addition of ZrO₂ nanofibres for reinforcing of SiC matrix has not been studied up to now.

In this work we investigated the effect of partially stabilized ZrO₂ nanofibres on the mechanical properties of SiC-based composite ceramics prepared by spark plasma sintering (SPS) at relatively low sintering temperature (1700 °C). For comparison, we studied the reinforcing effect of ZrO₂ particles, as well. The mechanical properties of composite ceramics were characterized in terms of Vickers hardness (HV) and Young's modulus. The phase composition and microstructure of sintered bodies were also studied in order to get some information on the mechanism of spark plasma sintering.

Methods

SiC-based ceramic composites were prepared by sintering commercial SiC powder (Washington Mills) containing ZrO_2 particles and nanofibres as reinforcing additives in concentration of 5, 10 and 15 wt %, respectively. A reference specimen was also prepared from SiC without reinforcement. Al_2O_3 powder (3 wt % of Alcoa, A16) was added as sintering aid to the green mixtures. Both commercial ZrO_2 particles (Sigma Aldrich, 99.0 %) and ZrO_2 nanofibres were partially stabilized by 3 mol % Y_2O_3. The nanofibres were prepared in our laboratory by electrospinning, as reported previously.[13]

The green mixtures, SiC matrices containing ZrO_2 fibres (SiC/ZrO_{2f}) or ZrO_2 particles (SiC /ZrO_{2p}) were prepared as follows: ZrO_2 nanofibres were dispersed in ethanol (Molar Chemicals, Hungary, 99.0 %) by ultrasonication for 30 min. The SiC and Al_2O_3 powders were mixed in a Fritsch planetary ball mill with alumina tank for 30 min at 400 rpm using alumina grinding balls (diameter: 10 mm). The SiC-Al_2O_3 powder blend and the ZrO_2 fibre dispersion were mixed with a magnetic stirrer for 30 min, followed by drying at 90 °C. Samples containing ZrO_2 particles and the reference sample (without ZrO_2) were prepared in the same way.

Discs prepared from the above green mixtures were subjected to spark plasma sintering (SPS) in a HD P5 sintering machine (FCT GmbH) at 1700 °C. The green bodies were heated in argon atmosphere (1 atm) at a rate of 200 °C·min⁻¹ with on/off current pulses of 3/1 ms, at ~3500 A and ~5 V. Holding time of 4 min was applied at 1700 °C in each test. During sintering a uniaxial pressure of 50 MPa was applied. The sintered samples were cooled down to near room temperature at a rate of 150 °C·min⁻¹. The high heating and cooling rates were necessary to accelerate the sintering process and to avoid any inadvertent reactions. The heating current and voltage were recorded along with the shrinkage of green bodies.

The bulk densities of sintered ceramics were measured by the Archimedes' method, while their relative densities were calculated supposing theoretical densities of 3.2, 3.9 and 5.7 g·cm⁻³ for monolithic SiC, Al_2O_3 and ZrO_2, respectively.

The morphology and microstructure of the Pd coated composites were studied with a Zeiss EVO40 scanning electron microscope (SEM). The elemental composition and the distribution of the components were characterized by an Oxford INCA manufactured energy dispersive X-ray spectroscope (EDS).
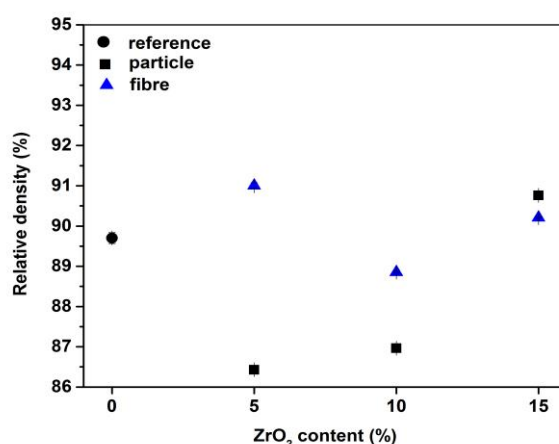
The phase compositions of sintered samples were determined with a Philips PW 1830 X-ray diffractometer (XRD) in the 2θ range of 20-70°.

The Young's modulus and Vickers hardness were measured using an instrumented indention tester (CSM Instrument, 500 mN Vickers diamond indentation force for 15 s). The hardness and elastic modulus were calculated from the load-depth curves according to the Oliver and Pharr method.[18] The reported hardness and modulus values are the mean of at least 9 measurements.

Results and discussions

Relative densities

The relative densities of sintered SiC ceramics as above were plotted in Figure 1. The reference sample had a relative density of 89.7±0.2 %. A bit higher relative density of 91±0.1 % was obtained for SiC reinforced with 5 wt % ZrO_2 fibre. Further increase of ZrO_2 fibre content however, resulted in smaller relative densities. In the case of reinforcement with ZrO_2 particles an opposite trend was observed: the relative densities increased with the ZrO_2 content. The highest relative density of 90.7±0.1 % was observed for sample containing 15 wt % ZrO_2 particles. According to Kodash and co-workers,[19] the observed differences in the relative densities could be attributed to the high heating, because the intense current application hinders particles gliding, thus decreasing the rate of densification.

Figure 1. Relative densities of sintered SiC ceramics reinforced with ZrO_2 particles and fibres, respectively
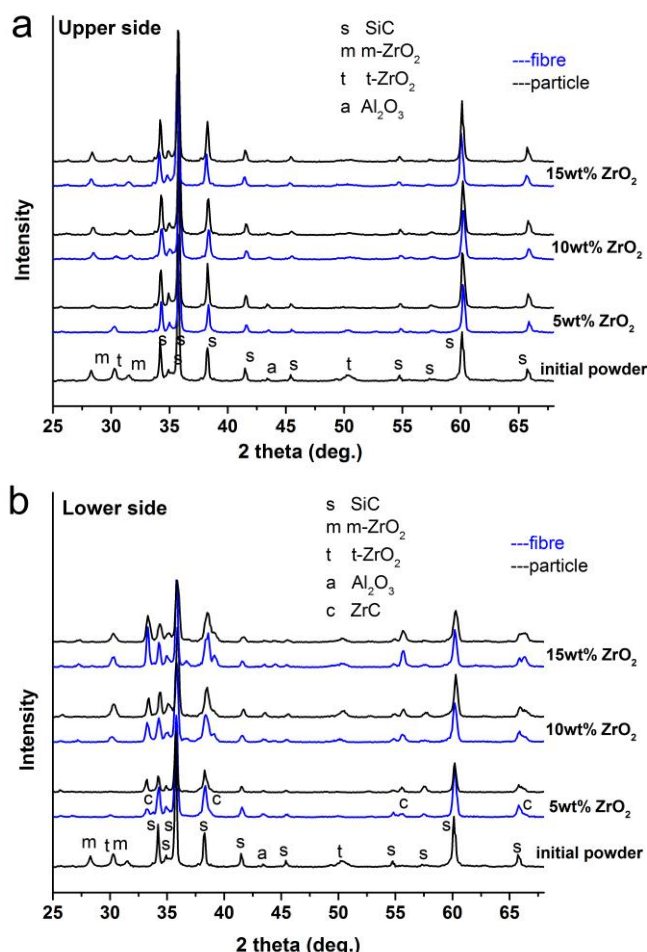
Phase compositions

The XRD patterns of ZrO_2 fibres and commercial YSZ particles are shown in Figure 2. The ZrO_2 nanofibres consist of tetragonal (t) phase only, while the commercial ZrO_2 particles are composed of tetragonal and monoclinic (m) ZrO_2 phases in nearly equal amounts.
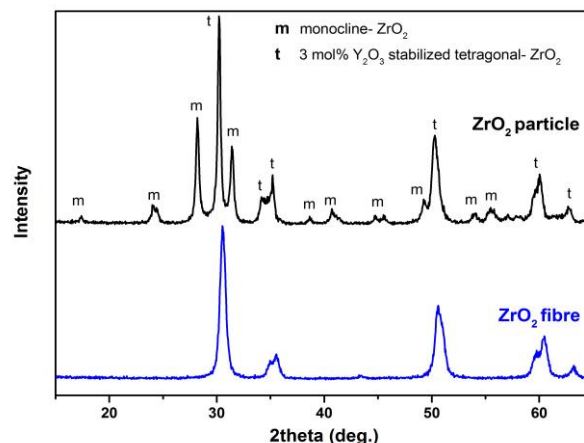
Figure 2. The XRD patterns of ZrO_2 nanofibres and particles

The diffraction patterns for both materials were in good agreement with the JCPDF2 card of the 3 mol % Y$_2$O$_3$ stabilized tetragonal ZrO$_2$ (JCPDF2 No. 83-113) and the card of the monoclinic ZrO$_2$ (JCPDF2 No. 13-0307), respectively. The XRD patterns of starting powder blends and sintered specimen of particular tests were shown in Figures 3a-b. In the starting powder blends the characteristic peaks of α-SiC crystallized in 6H-SiC and 4H-SiC polymorphs were detected.


Figure 3. Phase composition of the starting powders blends initial powder and the sintered composites as detected by XRD: a)upper side, b) lower side

On the XRD patterns of sintered composites we observed an interesting phenomenon. ZrC was developed as a new phase due to a chemical reaction between SiC and ZrO$_2$ (Figure 3b). The newly-formed ZrC is highly crystalline with typical crystalline size of ~196 nm as determined by Scherrer equation. However, ZrC was detected only at the lower side of composite discs, while the other side of the discs (upper side) consists of ZrO$_2$ phases only in SiC matrix (Figure 3a). The SPS configuration is shown by the Figure 4, where the upper and bottom punches are marked. The amount of ZrC increased with increasing zirconia content, and it was a bit higher for the particle-reinforced composites than for the fibre-reinforced ones. We found further differences in the phase compositions on the opposite sides of sintered specimens. While the initial powders contained t-ZrO$_2$ and m-ZrO$_2$ in roughly equal amounts, after sintering the m-ZrO$_2$ phase practically

disappeared, whilst the intensity of t-ZrO$_2$ increased on lower side. In contrast, on the upper side we could detect both phases of the ZrO$_2$, but the intensity of the t-ZrO$_2$ was significantly less comparing to the starting materials. The m-ZrO$_2$ → t-ZrO$_2$ transformation above 1170 °C is a well-known process that explains the tetragonal phase to be dominant on lower side. In case of fibre-reinforced composite, where only t-ZrO$_2$ phase was present, its amount did not change after sintering on lower side. On upper side m-ZrO$_2$ also appeared due to the t-ZrO$_2$ → m-ZrO$_2$ transformation. Lin et al.[20] supposed that alumina silicate glasses in the grain boundaries can scavenge yttrium ions from t-ZrO$_2$ grains, which is leading to a loss of stability of the tetragonal phase and t-ZrO$_2$ → m-ZrO$_2$ transformation can take place. In our case such transformation may also occur due to the presence of small glassy phase, even though we have not detected alumina silicate glass by XRD.

Differences in the phase compositions on the opposite sides of the sintered bodies can be attributed to the temperature differences between the different parts of graphite dies and by the different electrical conductivities of ZrO$_2$ and SiC. Anselmi-Tamburini et al. reported similar phenomenon in the case of cubic-ZrO$_2$ subjected to SPS for 5 min at 1200 °C under pressure of 105 MPa. However, they found just color differences between the two sides of the sintered bodies, because of the radial and axial temperature gradient during sintering and they suppose that the color gradient is a consequence of gradient in stoichiometry.[21]
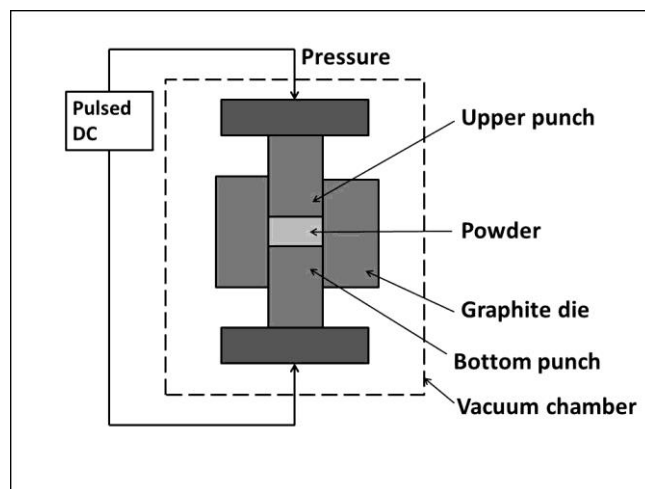

Figure 4. SPS configuration showing the graphite dies and punches

Microstructure

Figures 5a-b show the SEM micrographs of the initial powder blends. The size of SiC particles was around 3 μm, while the ZrO$_2$ particles were much finer with a mean size of ~0.8 μm (Figure 5b). The average diameter of ZrO$_2$ fibres as produced was ~0.5 μm; after ultrasonic treatment the length of the ZrO$_2$ fibres was ~5 μm (Figure 5a).

SEM micrographs of the fracture surface of sintered composites (Figures 6-8) show that grain growth of SiC can be minimized by the combination of short holding time and high heating rate (Figure 6). Both zirconia particles and fibres are evenly distributed in the ceramic matrix.
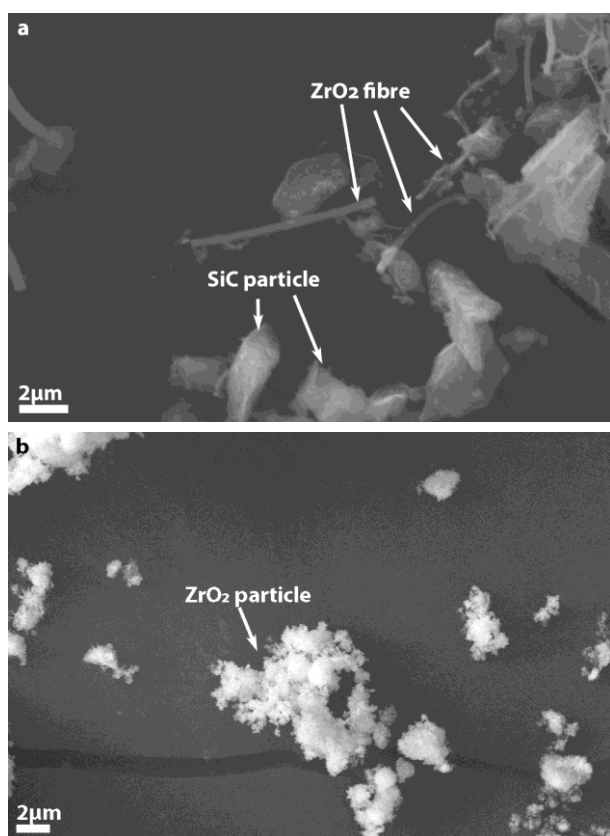
Figure 5. SEM micrographs of the initial SiC-Al$_2$O$_3$ powder mixtures with ZrO$_2$ nanofibres (a) ZrO$_2$ particles (b)

In the case of fibre reinforcement, the zirconia fibres were well oriented due to uniaxial pressure during sintering. No orientation was detected in the particle-reinforced composite. SEM micrographs also revealed that the zirconia fibres did not preserve their original morphology on sintering; most ZrO$_2$ fibres and also the particles were melted during SPS, as it can be seen in Figures 7 and 8.

Zirconia has a melting temperature over 2500 °C, however, in contact with alumina being present as sintering aid, it could form an eutectic mixture having melting temperature much below 2000 °C.[22] As a consequence, in the fibre reinforced composite fibres could only be sparingly observed, while their original positions can be well detected by the dispersed traces.

Figure 6. The fracture surface of the sintered reference SiC (secondary electron images)
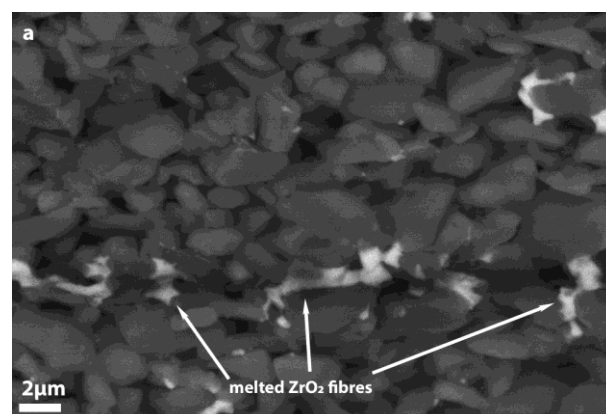
Figure 7. Fracture surfaces of sintered SiC reinforced with ZrO$_2$ nanofibres (backscattered electron images; (a, b) 10 wt% ZrO$_2$; (c) 15 wt% ZrO$_2$ nanofibres)
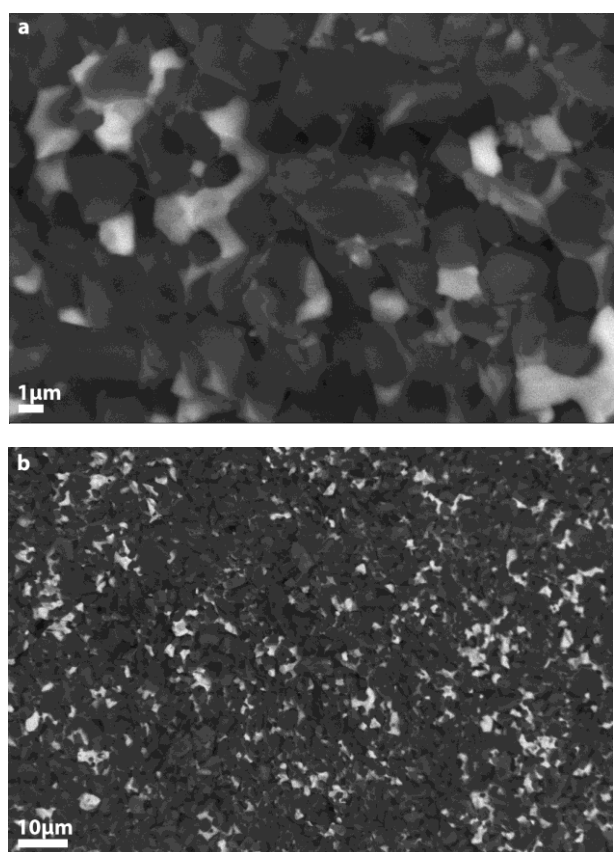
Figure 8. Fracture surface of sintered SiC matrix reinforced with 15 wt% ZrO₂ particle (backscattered electron images)

Energy dispersive X-ray spectroscopy (EDS) was also applied to get information about the microstructure and the newly formed ZrC in the SiC matrix containing 10 wt % ZrO₂ particles. Figure 9 shows the cross-sectional SEM micrographs and EDS mapping analysis of the two sides of specimen, while their composition was summarized in Table 1. Comparison of the concentrations of chemical elements on the two sides of specimen revealed that the concentration of C (27.73 at %) was higher on lower side than on the other (18.18 at %). However, on this side the concentrations of O and Si are less, than on the upper side, which confirmed formation of ZrC on lower side. The Pd came from the standard sample preparing procedure for SEM.

Table 1. Results of energy dispersive X-ray spectroscopy (EDS)

Element	Atomic%	
	Upper side	Lower side
C Kα	18.18	27.73
O Kα	17.35	13.31
Al Kα	1.80	1.95
Si Kα	55.62	50.42
Zr Kα	2.21	1.97
Pd Kα	4.83	4.62

At higher resolution, analysis of the element mapping showed the carbon distribution in the matrix (red dots in Figure 10). The carbon was detected at the grain boundary region of ZrO₂ particles. Based on this observation, we supposed that ZrC phase have been formed as an intergranular phase between ZrO₂ and SiC particles.
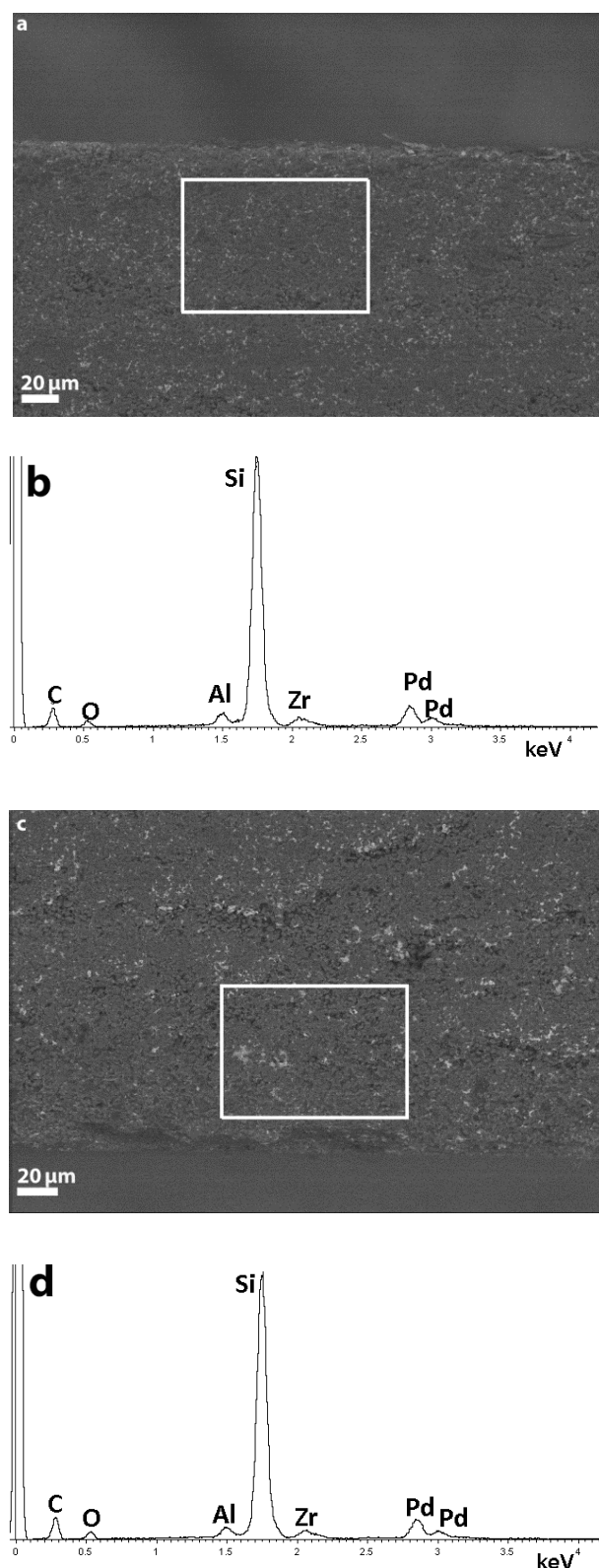


Figure 9. Results of EDS analysis of the sample containing 10 wt% ZrO₂ particles, a, c) morphology of the composites by SEM in cross- section view; b-d) results of EDS mapping

Mechanical properties

Because of the different phase compositions of the opposite surfaces of sintered specimens, as discussed above, we measured the mechanical properties on both sides of sintered composites.
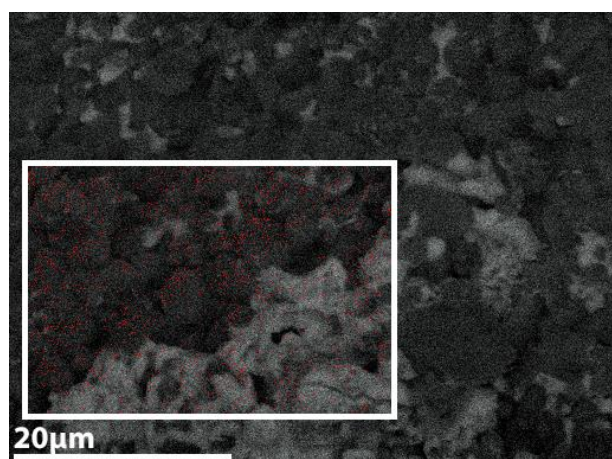
Figure 10. EDS element mapping analysis of the SiC/ZrO$_{2p}$ fracture surface, showing the distribution of C element (red dots) in the matrix

Figure 11 clearly shows that incorporation of reinforcing additives into the SiC matrix significantly increased the hardness as compared to the reference specimen, regardless of the type of additive (particle or fibre). The improvement in hardness, however, depended both on the ZrO$_2$ content and the arrangement of samples during hardness measurements. On the ZrC containing lower side (dashed lines in Figure 11.) significantly higher Vickers hardness was measured regardless of the reinforcing material. The highest hardness (25.15±3.6 GPa) was measured for the specimen containing 5 wt % ZrO$_2$ particles. However, the hardness of particular composites decreased with increasing ZrO$_2$. In case of fibre containing composites quite similar tendency was observed, but the actual HV values were slightly lower than in particle cases. On the upper side (straight lines in Figure 11.) however, the SiC/ZrO$_{2f}$ composites had higher HV values than the SiC/ZrO$_{2p}$ ones.
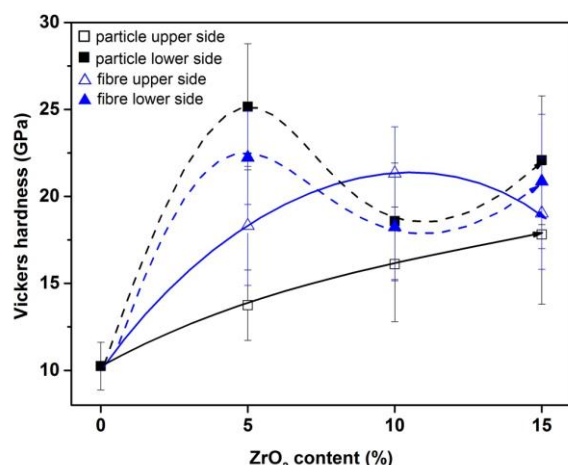

Figure 11. Vickers hardness of sintered SiC composites reinforced by ZrO$_2$ particles and fibres

Comparing with the other (lower) side, Vickers hardness exhibited a smaller, but continuous increase with zirconia content. The difference of HV values on the opposite sides of sintered samples can be attributed to the ZrO$_2$ + SiC → ZrC reaction.

In the particle containing composites more ZrC was formed that resulted in higher hardness on lower side as compared to the upper side.

Changes in the Young's modulus of specimens with zirconia content are similar to that in Vickers hardness. The reference specimen possessed the lowest modulus of 280.2±33.7 GPa. The elastic modulus tends to be significantly higher on the lower side than on the opposite side, due to presence of ZrC on this side of composite discs. Specimens containing ZrO$_2$ particles exhibit the highest modulus like the hardness. Adding ZrO$_2$ particles to the SiC matrix the modulus reached its maximum value (481.5±42.4 GPa) and a plateau at 10 wt % of ZrO$_2$ content. The modulus of the fibre containing composite was less by about a 100 GPa. On the upper side opposite tendency could be observed. The modulus increased with zirconia content both for fibre and particle reinforced composites. The SiC/ZrO$_{2f}$ composite has a bit higher modulus than the SiC/ZrO$_{2p}$ one, but they do not differ from each other on the upper side of composite discs. Comparing with the reference specimen a total improvement of 22.7 % was achieved in the modulus with a value of 345.08±19.2 GPa at 10 wt % ZrO$_2$ fibre content.
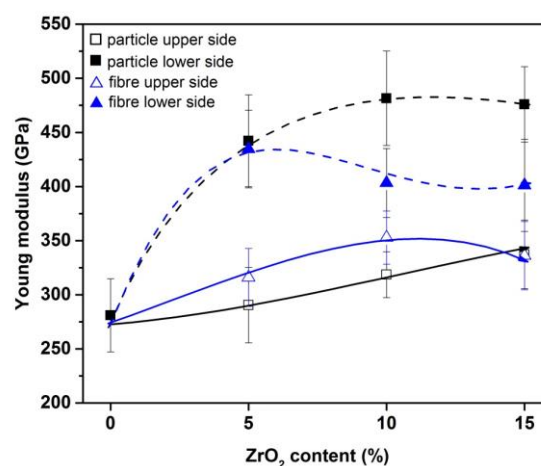
Figure 12. The Young's modulus for sintered SiC ceramics reinforced by ZrO$_2$ particles and fibres: dashed lines stand for upper side, while straight lines do for lower side

Conclusions

We produced silicon carbide-alumina (3 wt %) based composites containing partially (3 mol% Y$_2$O$_3$) stabilized ZrO$_2$ nanofibres and particles as reinforcing phases in concentrations of 5, 10 and 15 wt%, respectively, by spark plasma sintering. The 5 % SiC/ZrO$_{2p}$ composite had the maximum relative density of 91.02 %. The density decreased with the ZrO$_2$ content of composites. We suppose that it is due to the relatively low sintering temperature (1700 °C) and the high heating and cooling rates. Polymorphic phase transformations and structural changes were detected on sintering. A new phase, namely ZrC was formed during sintering. It could be attributed to a chemical reaction between SiC and ZrO$_2$. Nevertheless, ZrC could be detected only on the lower side of sintered discs, while their other side only ZrO$_2$ was found in the SiC matrix.

SEM micrographs revealed that the zirconia fibres did not retain their original morphology on sintering. It was the consequence of the melting of ZrO_2 fibres and particles during SPS. In spite of changes in the morphology of fibres, their original positions can be well detected by their dispersed traces. EDS element mapping analysis showed carbon distribution at the grain boundary region of ZrO_2 particles, thus, the ZrC likely formed as intergranular phase between ZrO_2 and SiC grains. The side of disc containing ZrC phase had significantly higher Vickers hardness regardless of the reinforcing material. The highest hardness (25.15±3.6 GPa) was detected on the lower side of composite discs reinforced with 5 wt% ZrO_2 particles. Both Young's modulus and Vickers hardness changed similarly with the zirconia content of sintered bodies. On that side of sintered discs where ZrC was found, significantly higher elastic modulus was detected as compared to their opposite side. Composites containing particles exhibited the highest modulus, with a highest value of 481.5 GPa in the case of sample containing 10 wt% ZrO_2 particles. In summary, SPS technique is currently a powerful research tool for developing a SiC/ ZrO_2 composites; however the protection of the ZrO_2 particle and fibre are necessary to avoid the degradation of the reinforcing materials.

References

[1]Saddow. S. E., Agarwal. A., Advances in Silicon carbide processing and applications, *Silicon carbide Overview*, Artech House, Inc. Boston, **2004**, 1-23, ISBN 1-58053-740-5

[2]Raju, K., Yoon, D.-H., Sintering additives for SiC based on the reactivity: A review. *Ceram. Int.* **2016**, *42*, 17947-17962 http://doi.org/10.1016/j.ceramint.2016.09.022

[3]Sedláka. R., Kovalcíková. A., Girman. V., Múdra. E., Rutkowski. P., Dubield. A., Dusza. J., Fracture characteristics of SiC/graphene platelet composites, *J. Eur. Ceram. Soc*., **2017**, *37*, 4307-4314 https://doi.org/10.1016/j.jeurceramsoc.2017.04.067

[4]Kovalcíková,, A. Dusza, J. Sajgalík, P., Thermal shock resistance and fracture toughness of liquid-phase-sintered SiC-based ceramics, *J. Eur. Ceram. Soc*., **2009,** *29*, 2387-2394 https://doi.org/10.1016/j.jeurceramsoc.2009.01.021

[5]Shinoda Y., Suzuki Y., Yoshida K., TEM analysis of nanocrystalline SiC ceramics sintered by SPS using Al₂O₃-TiO₂ additive, *J. Asian Ceram. Soc*., **2013,** *1*, 267-27 https://doi.org/10.1016/j.jascer.2013.06.004

[6]Feng, W., Zhang, L. T., Liu, Y. S., Li, X. Q., Cheng, L. F., Zhou, S. L., Bai, H., The improvement in the mechanical and thermal properties of SiC/SiC composites by introducing CNTs into the PyC interface, *Mater. Sci. Eng. A*, **2015**, *637*, 123-129 https://doi.org/10.1016/j.msea.2015.04.006

[7]Porwal, H., Tatarko, P., Saggar, R., Grasso, S., Kumar Mani, M., Dlouhý, I., Dusza, J., Reece, M. J., Tribological properties of silica-graphene nano-platelet composites, *Ceram. Int.,* **2014,** *40*, 12067-12074 https://doi.org/10.1016/j.ceramint.2014.04.046

[8]Young, R. J., Kinloch, I. A., Gong, L., Novoselov, K. S., The mechanics of graphene nanocomposites: A review. *Compos. Sci. Technol.,* **2012**, *72*, 1459-1476 https://doi.org/10.1016/j.compscitech.2012.05.005

[9]Porwal, H., Grasso S., Reecelm M. J., Review of graphene-ceramic matrix composites, *Adv. Appl. Ceram*., **2013** *112*, 443-454. http://dx.doi.org/10.1179/174367613X13764308970581

[10]Markys, G. G., Lewis, M. H., Microstructure and Fracture Toughness of Hot-Pressed Zirconia-Toughened Sialon, *J. Am. Ceram. Soc.,* **1993**, *76*, 1401-1408 http://dx.doi.org/10.1111/j.1151-2916.1993.tb03918.x

[11]Hayashi, K., Yamakawa, A., Room temperature strength and microstructure of Si₃N₄-Y₂O₃-ZrO₂-Al₂O₃ ceramics, *Mater. Sci. Eng.,* **1988,** *105-106*, 175-182 https://doi.org/10.1016/0025-5416(88)90494-6

[12]Dutta, S., Buzek, B., Microstructure, Strength, and Oxidation of a 10 wt % Zyttrite-Si₃N₄ Ceramic, *J. Am. Ceram. Soc*., **1984**, *61*, 89-92 454 http://dx.doi.org/10.1111/j.1151-2916.1984.tb09621.x

[13]Bódis, E., Molnár, K., Mucsi, A., Károly, Z., Móczó, J., Klébert, Sz., Keszler, A. M., Fazekas, P., Szépvölgyi, J., Silicon nitride-based composites reinforced with zirconia nanofibres, *Ceram. Int.,* **2017**, *43*, 16811–16818 https://doi.org/10.1016/j.ceramint.2017.09.078

[14]Baklanova, N. I., Matvienko, A. A., Titov, A. T., The Effect of ZrO₂ Interphase on Interfacial Frictional Stresses in SiC/ZrO₂/SiCf Composites, *Compos. Interfaces*, **2010,** *17*, 383–393 https://doi.org/10.1016/j.surfcoat.2010.10.025

[15]Petrovic, J. J., Bhattacharya, A. K., Honnell, R. E., Mitchell, T. E., ZrO₂ and ZrO₂-SiC particle reinforced MoSi₂ matrix composites, *Mater Sci. Eng. A*, **1992**, *155*, 259-266, https://doi.org/10.1016/0921-5093(92)90332-U

[16]Liu, D., Gao, Y., Liu, J., Li, K., Liu, F., Wang, Y., An, L., SiC whisker reinforced ZrO₂ composites prepared by flash-sintering, *J. Eur. Ceram. Soc*., **2016,** *36*, 2051-2055 https://doi.org/10.1016/j.jeurceramsoc.2016.02.014

[17]Padmavathi, N., Ghosal, P., Ray, K. K., Solution based processing and properties of carbon fiber reinforced SiC + ZrO₂ composites, *Compos. Sci. Tech*., **2015,** *106*, 55–59 http://dx.doi.org/10.1016/j.compscitech.2014.11.001

[18]Oliver, W. C., Pharr, G. M., An improved technique for determining hardness and elastic modulus using load and displacement sensing indentation experiments, *Mater. Res*., **1992**, *7*, 1564-1583 https://doi.org/10.1557/JMR.1992.1564

[19]Kodash V.Y., Groza J. R., Cho K. C., Klotz B. R., Dowding R. J., Field-assisted sintering of Ni nanopowders, *Mater. Sci. Eng. A*, **2004**, *385*, 367-371 https://doi.org/10.1016/j.msea.2004.06.075

[20]Lin, Y-J., Angelini, P., Mecartney, M. L., Microstructural and chemical influences of silicate grain-boundary phases in yttria-stabilized zirconia, *J. Amer .Ceram. Soc*., **1990**, *73*, 2728-35 https://doi.org/10.1111/j.1151 2916.1990.tb06753.x

[21]Anselmi-Tamburini U., Gennari S., Garay J. E., Munir Z. A., Fundamental investigations on the spark plasma sintering/synthesis process II. Modeling of current and temperature distributions, *Mater. Sci. Eng. A*, **2005**, *394*, 139-148 https://doi.org/10.1016/j.msea.2004.11.019

[22]Lakiza, S. N., Lopato, L. M., Stable and metastable phase relations in the system alumina-zirconia-yttria, *J. Am. Ceram. Soc.,* **1997,** *80*, 893-902 https://doi.org/10.1111/j.1151-2916.1997.tb02919.x

STUDIES ON THE ROLE OF EARTHWORMS IN BIOREMEDIATION OF MOTOR OIL

Safwat H. Shakir Hanna[a]*, Irvin W. Osborne-Lee [a], Elisha Taiwo Ahlinvide[a]

This study focuses on the bioremediation of soil contaminated with motor oil. Laboratory investigations were conducted to determine the ability of macro-organism's (i.e., earthworms) survival in soil contaminated with motor oil, and the role of macro-organisms in the contaminated soil (i.e., exposure to high toxicity in the soil). The soil was contaminated with two types of car motor oil, one with used motor oil from cars and the second was the pure car motor oil (i.e. was not used prior) in different concentrations [0% (i.e. control), 1 %, 3 %, 5 % and 10 % by weight contamination]. The soil parameters such as soil moisture %, carbon %, nitrogen %, pH, E_h, organic matter (OM) % and C/N ratio, were measured before and after contamination. Water content was maintained during incubation by making additions as determined from reweighed containers. Four worms (*Lumbricus terrestris)* were inoculated in each jar of the experiments. The length of the experiments was 30 days. The data of earthworms' survivability were measured each day. Motor oil content between 1-5 % was not harmful to the survival of earthworms for 30 days but oil concentration of 10 %, increased mortality rate by 75 % in pure motor oil and 45 % in used motor oil. Further, there was a significant difference in survivability of earthworms in used and pure motor oil. Used motor oil can support the survivability of earthworms better than pure (i.e. unused motor oil) motor oil. The properties of the soil at the end of the experiment showed an average reduction of 5 % carbon content, which indicated that the earthworms could consume the organic carbon with the support of micro-organisms in their digestive system. It was concluded that macro-organisms could be used for soil cleanup and restoration but that, Soil contamination of motor oil above 5 % might not allow for a similar process.

*Correspondent author:
E-Mail: safwat_shakir@yahoo.com
[a] P.O. Box 235, Texas Gulf Coast Environmental Data (TEXGED) Centre, Chemical Engineering Department, Prairie View A&M University, Roy G. Perry, College of Engineering, Prairie View A&M University, The Texas A&M University System] Prairie View, TX 77446, USA.

Introduction

Oil bioremediation technology is the most important technique that can avoid the oil spills' pollution and damages to the ecosystem and environment.The pollution by oil and the contamination of soils by motor oil pose a threat to the environment, and the remediation of oil-contaminated soils and water being a major challenge for environmental research.[1] Bioremediation is a useful method for soil treatment and restoration If motor oil contamination of the soil is moderate and non-biological methods are not economical.[1] Contamination of soil can occur through oil-tanker accidents, production spill, thoughtless actions of the increased number of automobiles on our roads, transportation of petroleum products, drilling activities on oil production sites and those emerging through accidental discharge,[1] etc. It is difficult to transport, store, or refine crude oil without spills and losses, and to prevent spills resulting from routine changing of motor oil or automobile crashes. The soil suffers the most ecological damage in the contaminated areas of the environment. There are high chances for a significant increase in soil and groundwater contamination at petroleum refineries.

Motor oil is one of the most common contaminants endangering both aquatic and terrestrial ecosystems.[1] Soil contaminated with motor oil presents a risk for groundwater and soil quality.[2] Appropriate disposal and/or cleans-up of contaminated sites are a legal requirement in the United States of America (USA) and most countries around the world.[2]

Motor oil is lubricating oil consisting of base lubricating oil, which is a mixture of hydrocarbons about 80 – 90 % by volume[2] and performance additives, which make up the remaining 10 – 20 %.[2] The use of this oil in motor engines alters the composition greatly due to break down of additives, introduction of metals through the wear and tear of the engine, and contamination resulting from combustion. Therefore, the components of motor oil after use vary greatly according to usage and degree of wear of metals within the lubricated area. Although the components of pure motor oil can be determined, it varies slightly from brand to brand. The major components of the used motor oil are aliphatic and aromatic hydrocarbons such as alkanes, cycloalkanes, naphthalene, phenol fluoranthene, benzo(a)pyrene, and benz(a)anthracene and high levels of heavy metals such as Pb, Zn, Cu, Cr, Ni, and Cd.[2,3]

The need to remediate contaminated site has introduced new technologies that emphasize the detoxification and destruction of the contaminants rather than the conventional approach of disposal.[4] The primary factor controlling the extent of biodegradation is the molecular composition of the petroleum contaminant. Multiple ring cycloalkanes are hard to degrade, while polynuclear aromatic hydrocarbons display varying degrees of degradation. Straight-chain alkanes biodegrade rapidly with branched alkanes and single saturated ring compounds degrading more slowly.[4]

As oil enters the environment, it begins to spread immediately. The viscosity of the oil, its pour point, and the ambient temperature will determine how rapidly the oil will spread, but light oils typically spread more rapidly than

heavy oils. The rate of spreading and ultimate thickness of the oil slick will affect the rates of the other weathering processes.[5] To cleanup a contaminated site, the contaminant will have to be determined; its degree of hazard to the environment assessed, and the best choice of remediation determined and applied.

The present paper has the following objectives:

1) Earthworms would remediate the oil-contaminated soil;

2) There is concentration range suitable for earthworms' survival, and

3) The productivity of the earthworms will decrease with the increased percentage of motor oil contamination.

Materials and Methods

Experimental design

Microcosm experiment (*oil, soil, and earthworms):* In order to achieve the research goals, we have used the microcosm.[6] An experimental approach to investigate the impact of the used motor oil and unused motor oil (i.e. pure oil) on the survivability of earthworms in the motor oil contaminated soil.

Surface horizon soil was collected from the Prairie View A & M farm in Waller County. The soil had grass growing on it, suggesting the absence of pesticide. The soil was a brown loamy fine sand, single grained; loose common fine roots; strongly acidic; clear smooth boundary with a pH of 4.5.

In this respect, set of jars (about 100 jars) were used in the experiment and these jars were 370 mL glass canning jars that were 6 cm diameter and 13 cm tall. These jars were divided to two sets: one set was about 50 jars to be used with used motor oil that was extracted from cars, and the other set was about 50 jars to be used with pure motor oil.

The used motor oil and the pure motor oil are from Castrol Brand (SAE 10 W- 30) - Partial Synthetic Oil). The pure motor oil used was newly manufactured lubricating motor oil design to lubricate, clean, inhibit corrosion, improve sealing and cool the engine.[7] It is comprised of petroleum-based and non-petroleum synthesized chemical compounds and blended using base oils composed of hydrocarbons, poly(alpha-olefins) (PAO), and polyinternal olefins[8] (PIO), which are made up of entirely carbon and hydrogen. Motor oil has heavy hydrocarbons in the range of 18-34 carbon atoms per molecule,[9] and is also characterized by other properties such as viscosity SAE, additives like detergent and dispersants additives, alkaline additives, and corrosion inhibitors.

The used motor oil was crankcase oil obtained through the oil change. The used motor oil contains petroleum and non-synthesized chemical compounds, blended with base oils

composed of hydrocarbons. The used motor oil contains metals derived from lubricating the engine. This new composition of the motor oil contains benzo[a]pyrene which is known for carcinogecity.[10]

The experimental procedure is designed by using two sets of fifty jars were divided into five groups, each group with its percentage concentration of motor oil. The concentrations of motor oil in these jars were 0 % (i.e. control experiment without contamination of motor oil), 1 %, 3 %, 5 % and 10 % soil contaminated on a soil dry weight basis, and the motor oil used and unused (i.e. pure) was thoroughly mixed with the soil. The water content was maintained at 25 % soil moisture content on soil dry weight basis. Water content was maintained during incubation by making additions as determined by reweighing the containers.

Four earthworms (*Lumbriscus terrestris)* were used in each jar (the average weight of the worm is between 2 to 4 grams each approximately) in this investigation. The reason for using this species is because it is a deep burrowing earthworm and would likely have higher exposure to oil in the soil. The jars were kept in an incubator at 20 °C as recommended by Kula and Larink.[11,12] The number of viable earthworms was determined after 5, 10, 15, 20, 25, and 30 days.

After, the completion and at the end of the experiment, soil samples were analyzed for testing the organic matter (OM %), pH, nitrogen content %, carbon content %, and E_h. In this respect, organic matter was determined through using the loss on ignition.[13] This method is used to determine the organic matter by drying the soil at 105 °C, and then weighted. The weighed crucible of dried soil, is heated in a furnace for a period of time up 16 hours at the temperature of 450 °C. The difference in weight of the soil before burning in furnace and after burning is used to determine the organic matter of the soil. According to this method, the calculation of carbon % is that of the organic matter multiplied by 0.58 to determine the carbon percentage from the organic matter.

For nitrogen determination, we used the Lecoo instrument Fp 528. The soil sample was weighted in the of range 0.2-0.29 gm and measured against the standard such as the soya flour with 8.84% and EDTA with 9.56 % nitrogen.

pH Analyses were conducted using the Accumet 1003 series pH meter model from Fishers scientific. The soil samples were weighted about 20 g of soil and added to it 40 g of distilled water. Then the soil samples were stirred for approximately 30 minutes in order to assure the uniformity of soil solution, and then the pH values were measured after standardizing the pH meter with pH 4.0, 7.0 and 10 buffer standard solutions (Fisher Brand SB 101-500, SB 107-500 and SB115-500). At the same time, we used the pH/E_h meter to measure the redox-potential of soil. The measured parameters were collected in order to measure the impact of these parameters on earthworms survivability in the contaminated soil with motor oil.

Data analysis

The experimental design was completely randomized, with a factorial arrangement of treatments. The data were submitted to two-way analysis of variance for statistical comparisons. SPSS,[14] SAS,[15] SYSTAT,[16] Sigma-Plot.[17,18] Software was used in the analysis. Additionally, sometimes the data were transformed using log and cosine functions in order to smooth the data and to reduce the variability as explained by.[19,20]

Results and Discussion

Environmental factors

The detailed data regarding environmental factors that were collected from the soil before the contamination of the soil and after the contaminations of soil with motor oil with different concentration levels at the beginning of the experiment were recorder in Tables 1-4. At the end of the experiment, the data of environmental factors were also recorded in Tables 5 and 6. The pH of the soil sample before the contamination of soil with motor oil used and pure before the commencement of the experiment was acidic averaged at 4.5 and 4.9 for the used and pure respectively (Table 7). This acidity was reduced after the contamination of the soil with motor oil, to 5.5 and 5.4 respectively for used and pure motor oil (Table 2). The increase is due to the alkalinity of the motor oil tending to neutralize the acid.

Table 1. Average mean physio-chemical parameters in the sampled soil (50 samples) before the addition of motor oil in experiment

Oil Type	pH	E_h	Om%	C%	N%
U	4.59	183.4	0.029	0.017	0.046
P	4.93	180.9	0.029	0.017	0.046

(U is used motor oil and P is pure motor oil- E_h is in millivolt)

Table 2. Average physiochemical parameters in the sampled soil (50 samples) after the addition of motor oil

Oil Type	pH	E_h	Om%	C%	N%
U	5.51	156.1	0.152	0.088	0.067
P	5.43	143.4	0.215	0.124	0.123

(U is used motor oil and P is pure motor oil- E_h is in Millivolt)

Table 3. Average physio-chemical parameters in the sampled soil (50 Samples) at the end of experiment with motor oil,

Oil Type	pH	E_h	Om%	C,%	N%
	mean	Mean	Mean	mean	Mean
U	7.18	138	4.56	2.65	0.548
P	6.75	58.84	3.66	2.12	0.118

(U is used motor oil and P is pure motor oil- E_h is in millivolt)

Improved greatly at the end of the experiment to 7.2 and 6.8 for the used and pure motor oil (Table 7). The increase at the end of the experiment is accounted for by the death and excretes of earthworms in the soil.

Organic matter of the sampled soil was 0.029 in the soil before the introduction of motor oil. The organic matter increased in the range of 1.0- 9.5 for the used motor oil and 0.68 – 9.5 for the pure motor oil after contamination of the soil with motor oil. It also had a pH range of 0.38 – 9.0 for the used motor oil and 0.49-9.04 for the pure motor oil at the end of the experiment. The activities of the earthworm are assumed to have reduced the organic content by way of feeding on the soil and its constituents. And the rise in the organic matter in the used motor oil can be inferred that the remains of the dead earthworms had added to the soil organic matter. (Table 8).

The soil nitrogen of the sampled soil before the addition of motor oil was 0.046 for both set of experiment. The nitrogen content of the soil sample after contamination with motor oil had the range of 0.037 – 0.37 for the used motor oil and 0.76 – 0.84, with a mean of 0.19 for used and 0.13 for pure motor oil. The nitrogen value reduced at the end of the experiment for the used motor oil samples but increased for that of the pure motor oil (Tables 4-6). In this respect, there was an overall improvement in the soil physiochemical properties in mixing motor oil with soil.

The soil E_h is between 183 – 120 for the used motor oil and 180 – 64 for the pure motor oil. The soil redox potential is an electrical measurement that shows the tendency of a soil solution to transfer electrons to or from a reference electrode. From this measurement we can estimate whether the soil is aerobic, anaerobic, and whether chemical compounds such as Fe oxides or nitrate have been chemically reduced or are present in their oxidized forms.[21]

Earthworms Survivability

The survival of earthworms in the studies of earthworms in both used and pure motor oil had the best of survivors in the 5 % concentration.Though the death of the earthworms in concentrations 0, 1, and 3% concentration did not follow the expected pattern and of course as seen on Figures 1 and 2, and Tables 9 and10, they were more death recorded in these concentrations than they were in concentration with 5% motor oil. This implies that factors other than those of motor oil concentration were responsible for the dead of earthworms in concentration 0, 1, and 3 %, because the earthworms survived very well in 5 % concentration of the motor oil. In 10 % concentration of the motor oil both in used and pure motor oil the earthworms could not survive as much, about 50 % of the earthworms were dead by the 5th day of the studies.

Survival of earthworms 'Lumbricus terrestris was expected to decrease as the concentration of the used motor oil increases. This was not the case as seen in (Figure 1).

Table 4. Average physiochemical parameters in the sampled soil before addition of motor oil (Number of samples =10)

Treatment	Oil type	pH	E_h	OM	C%	N%	Nml
T1	U	4.38	189	0.500	0.290	0.056	0.028
T2	U	4.75	180	0.620	0.359	0.047	0.023
T3	U	4.55	186	0.500	0.290	0.068	0.034
T4	U	4.62	185	0.519	0.302	0.044	0.021
T5	U	4.69	182	0.619	0.359	0.042	0.020
T1	P	5.32	173	0.498	0.289	0.056	0.028
T2	P	4.95	181	0.614	0.356	0.047	0.023
T3	P	5.05	186	0.496	0.288	0.044	0.022
T4	P	4.92	185	0.673	0.391	0.044	0.021
T5	P	4.69	182	0.611	0.354	0.042	0.020

U=used motor oil, P=pure motor oil, T1=control, [T2=1%, T3=3%, T4=5%, T5=10% percentage of oil added] and E_h *is* in millivolt

Table 5. Average physio-chemical parameters in the sampled soil after the addition of motor oil used (U) and pure (P)

Type of Treatment	Oil type	pH	E_h	OM	C%	N%	Nml
T1	U	5.63	137	1.007	0.584	0.099	0.035
T2	U	5.04	121	2.077	1.205	0.069	0.032
T3	U	4.24	350	5.073	2.943	0.068	0.034
T4	U	6.03	109	5.161	2.994	0.064	0.029
T5	U	6.06	104	9.498	5.509	0.044	0.026
T1	P	5.73	137	0.678	0.393	0.154	0.036
T2	P	5.40	151	2.291	1.328	0.094	0.025
T3	P	5.41	143	4.030	2.337	0.154	0.021
T4	P	5.40	145	6.530	3.788	0.124	0.031
T5	P	5.35	135	9.214	5.344	0.107	0.024

U=used motor oil, P=pure motor oil, T1= control, [T2=1%,, T3=3%, T4=5%, T5=10% of oil added] and E_h *is* in millivolt

Table 6. Average physio-chemical parameters in the sampled soil at the end of experiment with motor oil used(U) and pure (P)

Treatment	Oil type	pH	E_h	OM%	C%	N%	Nml
T1	U	7.5	43	0.384	0.222	0.047	0.024
T2	U	6.92	118	1.083	0.628	0.057	0.027
T3	U	8.68	-16	3.781	2.193	0.048	0.021
T4	U	4.7	382	4.079	2.946	0.045	0.022
T5	U	8.14	164	9.050	6.247	0.075	0.020
T1	P	6.75	57	0.499	0.289	0.125	0.034
T2	P	6.29	94	1.210	0.701	0.136	0.040
T3	P	6.88	45	3.372	1.956	0.115	0.034
T4	P	6.84	57	4.015	2.329	0.120	0.033
T5	P	6.98	41	9.040	5.246	0.170	0-029

U=used motor oil, P=pure motor oil, T1=control, [T2=1%, T3=3%, T4=5%, T5=10%] %=percentage of oil added, E_h *is* in millivolt

Table 7. The comparison of pH in the three stages of the experiment

Concentration	Stage 1 (P)	Stage 1 (U)	Stage 2 (P)	Stage 2 (U)	Stage 3 (P)	Stage 3 (U)
0%	5.32	4.38	5.73	5.63	6.75	7.50
1%	4.95	4.75	5.40	5.04	6.29	6.92
3%	5.05	4.55	5.41	4.24	6.88	6.68
5%	4.92	4.62	5.40	6.03	6.84	4.70
10%	4.95	4.69	5.35	6.06	6.98	8.14

Stage 1 means test before introducing motor oil, Stage 2 means test with motor oil, Stage 3 means test at the end of experiment U=used motor oil P=pure motor oil.

Table 7. The comparison of pH in the three stages of the experiment

Concentration	Stage 1 (P)	Stage 1 (U)	Stage 2 (P)	Stage 2 (U)	Stage 3 (P)	Stage 3 (U)
0%	5.32	4.38	5.73	5.63	6.75	7.50
1%	4.95	4.75	5.40	5.04	6.29	6.92
3%	5.05	4.55	5.41	4.24	6.88	6.68
5%	4.92	4.62	5.40	6.03	6.84	4.70
10%	4.95	4.69	5.35	6.06	6.98	8.14

Stage 1 means test before introducing motor oil, Stage 2 means test with motor oil, Stage 3 means test at the end of experiment U=used motor oil P=pure motor oil.

Table 8. Comparison of organic matter in the three stages of the experiment

Concentration	Stage 1 (P)	Stage 1 (U)	Stage 2 (P)	Stage 2 (U)	Stage 3 (P)	Stage 3 (U)
0%	0.5	0.5	0.7	1.0	0.5	0.4
1%	0.6	0.6	2.3	2.0	1.2	1.1
3%	0.5	0.5	4.0	5.0	3.4	3.8
5%	0.7	0.5	6.5	5.2	4.0	4.1
10%	0.6	0.6	9.2	9.5	9.0	9.1

Stage 1 means test before introducing motor oil   Stage 2 means test with motor oil.Stage 3 means test at the end of experiment U=used motor oil P=pure motor oil

At 5% used motor oil concentration had survivors of 100% in the day 5, 85% in the day 10, 80% in the day 15, 68% in the day 20, 45% in the day 25, and 43% in the day 30.Concentrations, 0% (control), 1% and 3% had percentage survivors lower than those of 5 % percent concentration. 0 % had 85, 63, 60, 60, 60, and 58 %, 1 % had 98, 58, 25, 25, 25, and 25 %, while 3 % had 100, 53, 30, 20, 5, and 0 %, in days 5, 10, 15, 20, 25, and 30, respectively. The earthworms' survival did not follow gradual decrease with increase in the concentration of the motor oil as expected but showed a drastic decrease in 10% oil concentration.

in the experiment followed a similar pattern with the first. Concentration 0% motor oil had percentage survival of 100, 100, 60, 28, 10, and 10%, concentration 1 % had 95, 90, 55, 23, 5, and 5 %, and concentration 3 % motor oil recorded 88, 78, 63, 45, 15, and 5% in the day 5, 10, 15, 20, 25, and 30 respectively (Figure 2, Tables 9 and 10). The survivability went out of the expected pattern, though it followed the pattern similar to that of the experiment with used motor oil, having good survivors up to 5 % concentration. The earthworms could not survive in 10 % concentration beyond the 5th day as 67 % were already dead by the 5th day.
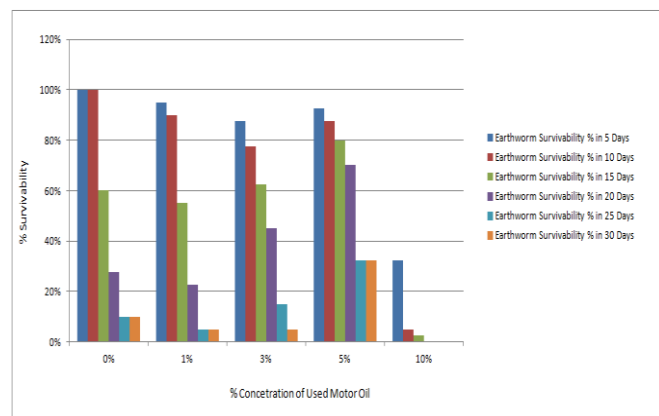
Figure 1. Graph of percentage of earthworm survivability against used motor oil as % of concentration
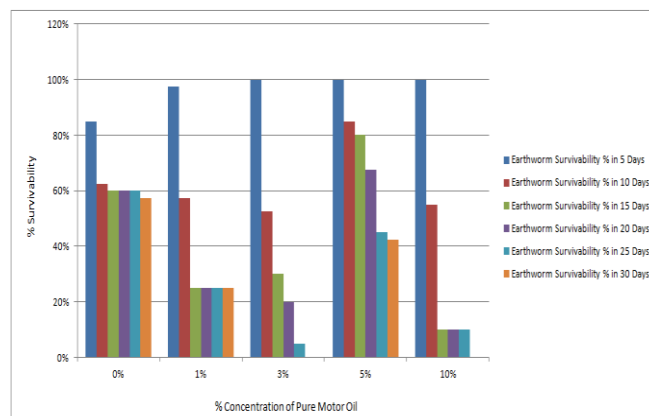
Figure 2. Graph of earthworm survivability as % against pure motor oil as % of the concentration

The second experiment with pure motor oil recorded a greater survivability, with 93 % in the day 5, 88 % in the day 10, 80 % in the day 15, 70 % in the day 20, 33 % in the day 25 and 33 % in the day 30. The survival of earthworms

The survival of earthworms in both used and pure motor oil had the best of survivors in the contaminated samples with 5 % concentration.Though the death of the earthworms in concentrations 0, 1, and 3 % did not follow the expected

Table 9. Survivability average of earthworms in experiments with motor oil, used (U) and pure (P) at the end of the experiment in the individual.

Type of treatment	Oil type	D5	D10	D15	D20	D25	D30
T1	U	3.4	2.5	2.4	2.4	2.4	2.3
T2	U	3.9	2.3	1.0	1.0	1.0	1.0
T3	U	4.0	2.1	1.2	0.8	0.2	0.0
T4	U	4.0	3.4	3.2	2.7	1.8	1.7
T5	U	4.0	2.2	0.4	0.4	0.0	0.0
T1	P	4.0	4.0	2.4	1.1	0.4	0.4
T2	P	3.8	3.6	2.2	0.9	0.2	0.2
T3	P	3.5	3.1	2.5	1.8	0.6	0.2
T4	P	3.7	3.5	3.2	2.8	1.3	1.3
T5	P	1.3	0.2	0.1	0.0	0.0	0.0

U=used motor oil, P=pure motor oil, [T1= control, T2=1 %, T3=3 %, T4=5 %, and T5=10 % of oil added], D5=day 5, D10=day 10, D15=day 15, D20=day 20, D25=day 25, D30=day 30.

Table 10. Survivability of L. terrestris in experiment with used (U) and pure (P) motor oil after 30 days as %

Treatment Type	Oil Type	D 5	D10	D15	D20	D25	D30
T1	P	100%	100%	60%	28%	10%	10%
T2	P	95%	90%	55%	23%	5%	5%
T3	P	88%	78%	63%	45%	15%	5%
T4	P	93%	88%	80%	70%	33%	33%
T5	P	33%	5%	3%	0%	0%	0%
T1	U	85%	63%	60%	60%	60%	58%
T2	U	98%	58%	25%	25%	25%	25%
T3	U	100%	53%	30%	20%	5%	0%
T4	U	100%	85%	80%	68%	45%	43%
T5	U	100%	55%	10%	10%	10%	0%

U=used motor oil, P=pure motor oil, T1= control, [T2=1 %, T3=3 %, T4=5 %, T5=10 % of oil added], D5=day 5, D10=day 10, D15=day 15, D20=day 20, D25=day 25, D30=day 30.

pattern (Figures 1 and 2, and Table 9 and 10), they were more death recorded in contaminated samples with ten percent % concentration of the motor oil in both studies, while concentration with 5 % motor oil recorded the most survivors. This implies that factors other than those of motor oil toxicity were responsible for the dead of earthworms in concentration 0, 1, and 3 %, because the earthworms survived very well in 5 % concentration of the motor oil.

In 10 % concentration of the motor oil both in used and pure motor oil, the earthworms could not survive as much, about 50 % of the earthworms were dead between the 10th day and the 15th day of the studies as a general observation. This means the death of earthworms is caused by the toxicity of motor oil.

The tree diagrams showed similarities in the oil-type and various concentrations (Figures 3 and 4).
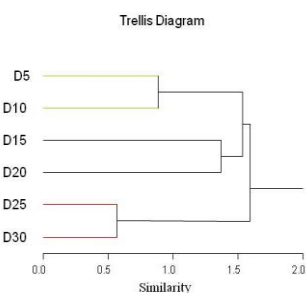
In Figure 3, The survival of earthworms in used motor oil had two groups, day five (D5) and day ten (D10) with high survivors, and day fifteen (D15), day twenty (D20), day twenty five (D25) and day thirty (D30) with high fatality (Figure 3).

A comparison between the number days D5 and D10, D15, D20, D25 and D30 and the concentration was plotted. The comparison of D5 with other concentrations and showed a clustered pattern with the only deviation emerging in 10 % concentration of motor oil. This pattern indicates a norm in or sustainable toxicity to the earthworms excluding the 10 % concentration; hence at 5 % concentration earthworms can be used to clean up a contaminated site.

In Figure 4, a pattern of survivability in pure motor oil is observed. There is a similarity between the survival of earthworms in day five (D5) and day ten (D10), and also between day fifteen (D15) and day twenty (D20) of the experiment.D5 and D10 had a higher degree of survival than D15 and D20. But the twenty-fifth day (D25) and the thirtieth day (D30) are further apart indicating a very low percentage of earthworm survival (Figure 4).

As can be observed from Figures 5, 6, 7, and 8, when survivability of earthworms in soil contaminated with motor oil was plotted against the duration of the experiment in days, the chances of survival for the earthworms decreased as the length of days of the experiment increases.

The survival of earthworms throughout the duration of the experiment was plotted but normalized such that, the equation would not be limited to a specific number of earthworms to be used in the experiment. In this case, the desired number of earthworms would be multiplied by one (1). With this parameter, the survivability was normalized in two equations, the exponential and the polynomial fit. It was found that the exponential fit is the closest to the normal measured data.

Figure 3. Similarity[1] of survivability of earthworms in the soil contaminated with used motor oil
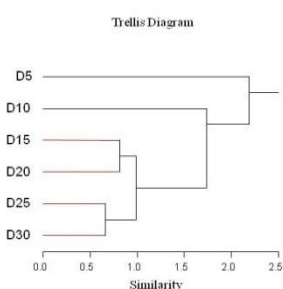
Figure 4. Similarity[1] of survivability of earthworms in the soil contaminated with pure motor oil
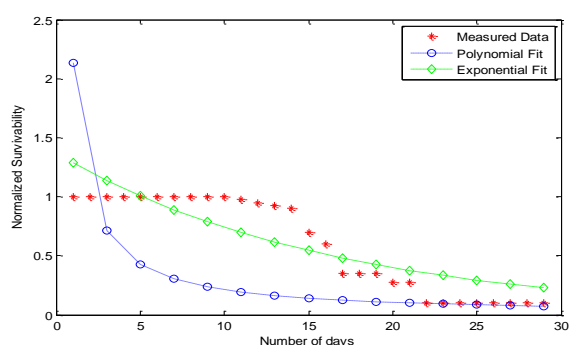
Figure 5. Survivability of earthworms in 1 % of pure motor oil

---

[1] scale is referred to the similarity distance in hierarchical clusters that are displayed in a tree which is using Computes a normalized Euclidean distance (root-mean-squared differences) matrix for all the variables in variable list (i.e. days of the experiment as 5, 10, 20, 25, and 30).
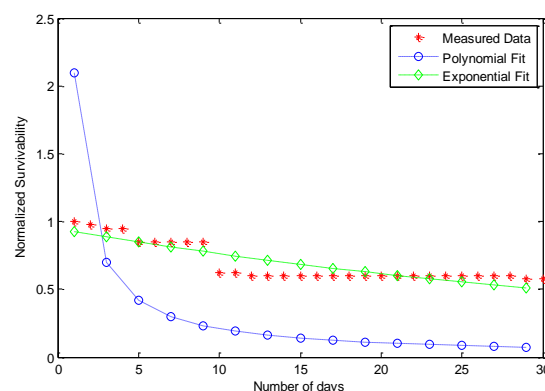
The exponential form of normalized survivability is:

$$s = a\exp(-bdy)$$

where a and b are fitting parameters, d is the percent concentration and y is the number of days. From the minimum mean square error fitting: a=1.3686, and b= 6.1489. The polynomial form is:

$$s = a/(dy)$$

From the minimum mean square error fitting: $a = 0.0213$

Figure 6. Survivability of earthworms in 1% of used motor oil

Normalized survivability_

$$s = a\exp(-bdy)$$

where a and b are fitting parameters, d is the percent concentration and y is the number of days. From the minimum mean square error fitting: a= 0.9480, and b= 2.1625.

Polynomial form_

$$s = a/(dy)$$

From the minimum mean square error fitting: $a = 0.02095$.

Analysis of variance

One-way ANOVA analysis of earthworms' survivability for the first 5 days in contaminated soil with pure and used motor oil showed significant difference between different concentrations of motor oil % [i.e. F =13.12 and P<0.001 for pure motor oil type], and [i.e. F=4.19 and P<0.0057 for used motor oil type] (Tables 11 and 12).
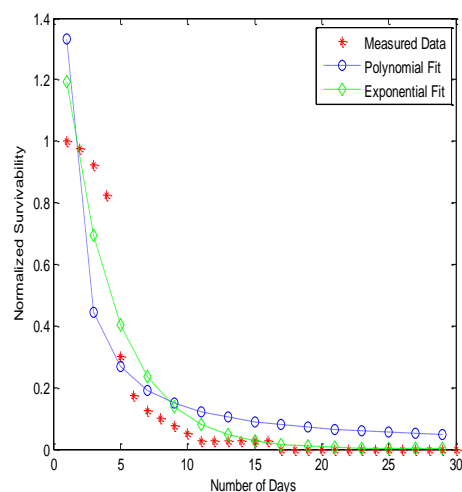
Figure 7. Survivability of earthworms in 10% of pure motor oil
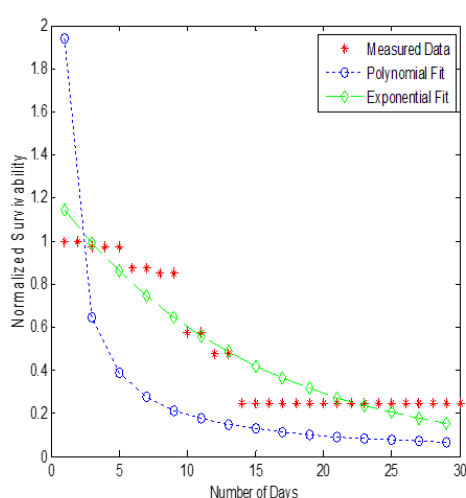
Figure 8. Survivability of earthworms in 10% of used motor oil

However, the ANOVA Two-ways analysis for earthworms' survivability in different motor oil types at different concentrations % indicated that there are significant results [i.e. F=16.33 and P<0.001 for motor oil type] and [i.e. F=9.54 and P<0.001 for motor oil concentrations]. However, the impact of the interactions between motor oil type and motor oil concentrations on the earthworms' survivability showed significant results [i.e. F= 14.05 and P<0.001] (Table 13).

Table 11. ANOVA analysis for survivability of earthworms in contaminated soil with used motor oil (D5)

Source	DF	Sum of Squares	Mean square	*F* Value	*Pr > F*
Model	4	49.32	12.33	12.12	< .0001
Error	45	42.30	0.94		
Corrected Total	49	91.62			

Table 12. ANOVA Analysis for survivability of earthworms in contaminated soil with pure motor oil (D5)

Source	*DF*	Sum of Squares	Mean square	*F* Value	*Pr > F*
Model	4	2.72	0.68	4.19	0.0057
Error	45	7.30	0.16		
Corrected Total	49	10.02			

One-way ANOVA analysis of earthworms' survivability at the end of the studies (i.e. at 30 days in contaminated soil with pure and used motor oil) showed insignificant difference between different concentrations % of pure motor oil type [i.e. F =2.37 and P<0.07], and significant difference between different concentrations [i.e. F=6.34 and P<0.0004] for used motor oil type (Tables 14 and 15).

Table 13. MANOVA analysis for survivability of earthworms in contaminated soil with motor oil types and interaction between oil type and concentration oil (D5)

Source	DF	Sum of squares	Mean square	*F* Value	*Pr > F*
Concent-ration	4	13150.0	3287.5	9.54	<0.0001
Oil type	1	5625.0	5625.0	16.33	<0.0001
Oil type/ concent-ration	4	19375.0	4843.8	14.05	<0.0001

However, the ANOVA two-ways analysis for earthworms' survivability in different motor oil at different concentrations % indicated that there are significant results (i.e. pure and used motor oil [i.e. F=6.11 and P<0.01 for motor oil type] and [i.e. F=6.98 and P<0.01 for motor oil concentrations]. However, the impact of the interaction between motor oil type and motor oil concentrations on the earthworms' survivability showed significant results [i.e. F=2.51 and P<0.05] (Table 16).

Table 14. ANOVA Analysis for Survivability of Earthworms in Contaminated Soil with pure motor oil (D30)

Source	*DF*	Sum of Squares	Mean square	*F* Value	*Pr > F*
Model	4	10.48	2.62	2.37	0.0664
Error	45	49.70	1.10		
Corrected Total	49	60.18			

**Table 15.** ANOVA Analysis for Survivability of Earthworms in Contaminated Soil with used motor oil (D30)

Source	*DF*	Sum of squares	Mean square	*F* Value	*Pr > F*
Model	4	41.80	10.45	6.34	0.0004
Error	45	74.20	1.65		
Corrected Total	49	116.00			

Table 16. MANOVA analysis for survivability of earthworms in contaminated Soil with motor oil types and interaction between oil type and concentration (D30)

Source	DF	Sum of Squares	Mean square	F value	Pr > F
Concentration	4	24025.00	6006.30	6.98	<0.0001
Oil Type	1	5256.30	5256.30	6.11	0.0153
Oil type /concentration	4	8650.00	2162.5	2.51	0.0471

Impacts of ecological factors on earthworms survivability

Earthworm survivability in contaminated soil with used and pure motor oil has shown variation in survivability due to the ecological parameters that prevailed in the experiment. In this respect, during the survivability test of earthworms in contaminated soil with used and pure motor oil (i.e. the one-month period of study) showed that the survivability of earthworms decreased from 100 % to 40 % during the first 15 days and declined until it reached 20 % at the end of the experiment (Figure 9).
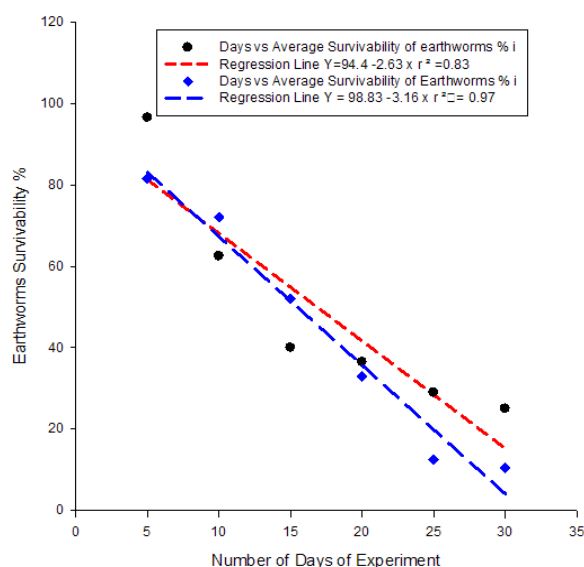
Figure 9. Relationship between the number of days of the experiment and average earthworms survivability % in contaminated soil with used and pure motor oil

Earthworm's survivability with respect to pH (Figure 10) showed the highest survivability rate at a pH (7.0) in contaminated soil with pure and used motor oil. There is a significant relationship between pH and the survivability of earthworms. In addition, it is found that the earthworm's survivability decreased when the pH moved from neutral to alkaline (8-10).
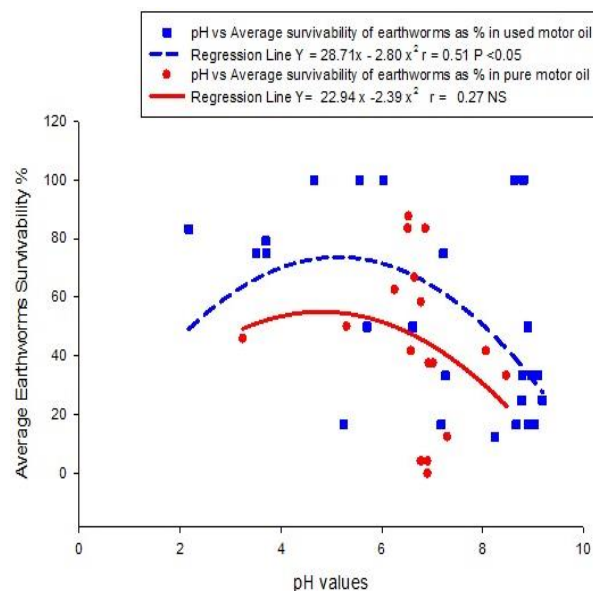
Earthworm's survivability (Figure 11) increased when the OM% reached 6-8%. On the other hand, earthworms showed a significant decrease of the survivability when the organic matter increased more than 10% and this is related to the increase carbon % which impacted on its degradation by microbial organisms in the gut of the earthworms and has resulted in the degradation of these toxic materials and

heavy hydrocarbon. The present heavy materials of hydrocarbon in the motor oil have prevented the earthworms from its ability to degrade these compounds, and it is due to the lack of microorganisms that are able to degrade the hydrocarbon.

The earthworms showed a significant increase in survivability when the nitrogen percentage increased. Consequently, the increase of nitrogen has enhanced the ability of earthworms and the microbial organisms in the earthworms' guts to decompose the heavy hydrocarbon materials in the motor oil (Figure 12).

Further, the survivability of earthworms with respect to concentration of motor oil showed an increase in survival as the concentration of motor oil increased up to 5% concentration and declined steadily after that (Figure 13).

The earthworms showed increased survivability in the contaminated soil, with a rise in C/N ratio and its peak at a ratio of 50. A further rise in the C/N ration beyond fifty 50, affected the survival of earthworm as seen in the graph. The increase led to a rise in the toxicity of the soil and hence the inability of earthworms to survive (Figure 14).


Figure 10. The relationship between pH and average earthworms survivability % in contaminated soil with used and pure motor oil.

The above results are supported by the comparison of the day five D5 and the day D30 with the concentration T1-T5 as shown in Figure 16, in which it shows a cluster of the various concentrations with similarities in concentration 0, 1, 3 and 5 %. The 10 % concentration is completely off the scale.

Earthworm's survivability (Figure 15) increased when the C% reached 2-4 %. The earthworms showed a significant increase in survivability with the rise in carbon content but declined after four (4 %) increase in carbon. The increase in carbon content became much toxic and its degradation by microbial organisms in the gut of the earthworms was inhibited by the toxicity.
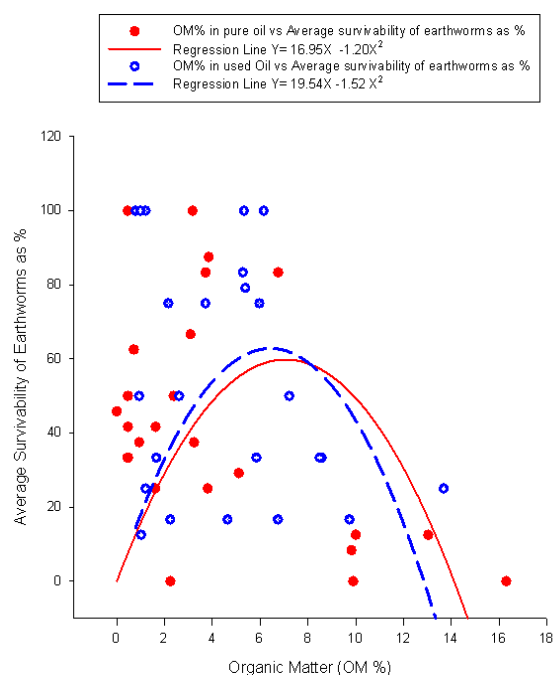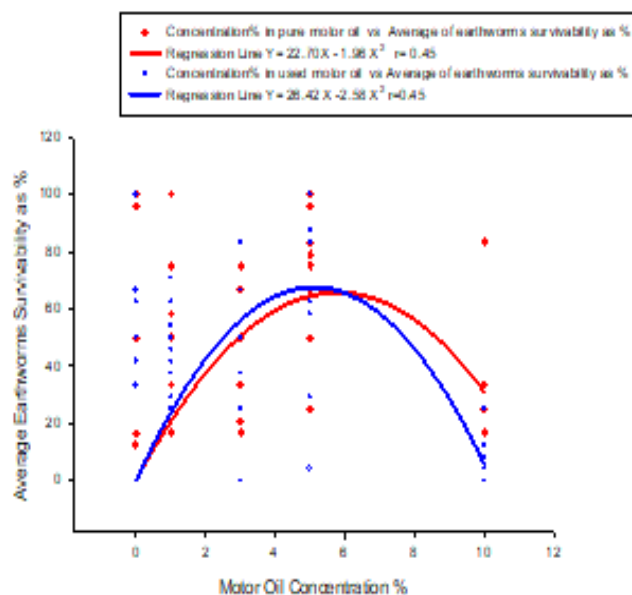
Figure 11. Relationship between averages of earthworms' survivability as % and organic matter (OM %) in contaminated soil with used and pure motor oil
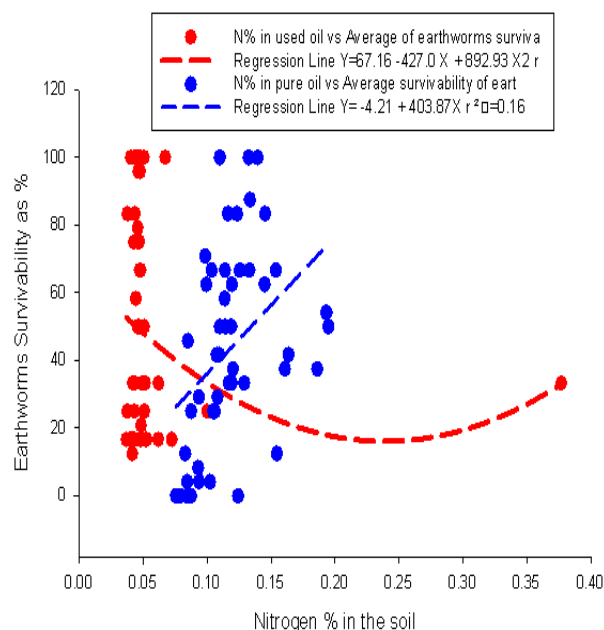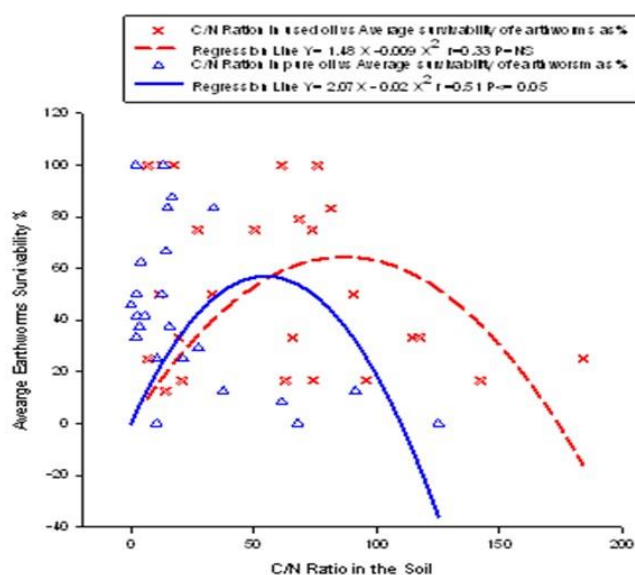

Figure 12. Relationship between average earthworms survivability % and nitrogen % in contaminated soil with used and pure motor oil

A graphic representation model of the entire process was developed (Figure17). It is important in this experiment to present a visual model for a clear understanding of the processes by which earthworms deal with the decomposition of organic hydrocarbon materials in the soil. The diagram shows how the earthworms can improve the soil quality to

degrade these contaminants and convert it to fewer toxic substances and, to enhance the process of biodegradation through the combing activities of earthworms and the microorganisms in their guts or the digestive tract of earthworms.
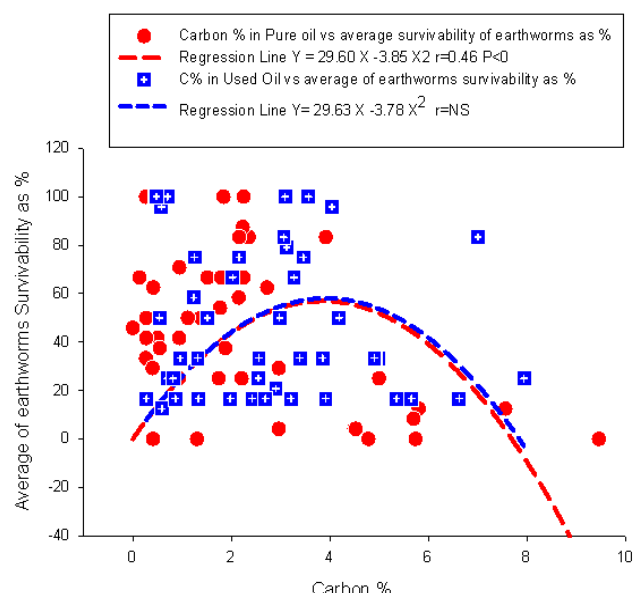

Figure 13. Relationship between average earthworms survivability as % and motor oil concentration % in contaminated soil with used and pure motor oil.

Figure 14. Relationship between C/N ratio and average survivability of earthworm's %in contaminated soil with used and pure motor oil

At the end of the experiment, the carbon content % of the soil samples was measured and recorded. The carbon content of the soil samples before and after the inoculations of the earthworm was recorded.

Figure 15. Relationship between average earthworms survivability % and soil carbon % in contaminated soil with pure and used motor oil

The percentage carbon reduction in each concentration, both pure and used motor oils are as follows: 1) In 0 % concentration, 26 % and 38 % in the pure and used motor oil respectively; 2) In 1 % concentration, 47 % and 47 % in the pure and used motor oil respectively; 3) 3 % concentration had 16 % and 25 %; in the pure and used motor oil respectively; 4), 5 % concentration recorded 38 % and 20 % in the pure and used motor oil respectively; and 5)10 % concentration recorded 1.8 % total reduction of carbon in the pure motor oil and 4.7 % total in the used motor oil. In this respect, Daniel A. Vallero[22] Indicated that the earthworms could degrade pollutants into simpler, less toxic forms, while the organisms at the lower levels of the biological organization transform substances in the direction of mineralization, i.e. toward inorganic compounds (those that lack carbon-to-carbon and carbon-to-hydrogen covalent bonds), and that motor oil biodegradation can be enhanced and was accelerated from 55.9% to 64.4% by adding other micro-organisms. This result can support that the microorganisms that are existing in guts of earthworms can have accelerated influence in the decomposition of hydrocarbons in the motor oil, which is the case in the present study.

Metals have been shown to cause mortality[23-26] and reduce fertility,[27] and growth[28] of earthworms. Therefore, a higher percentage survival of earthworms was expected in the pure motor oil than in the used motor oil due to the presence of toxic metals in the used motor oil, but the reverse was the case.

The cause of this unexpected result cannot be determined at this time. More studies are needed for this purpose to find out. The survival of earthworms in the contaminated soil was impacted on by the pH of the soil. As the pH increases the survivability also increases, and reached its peak at pH of 7 as seen on the graph (Figure 10).

The organic matter and carbon content of the soil also impacted the survival of the earthworms. The soil originally was very low in carbon and organic content, an unfavorable condition for the earthworms. But as both the carbon and organic content increased, the survivability of the earthworms also increased. The carbon and organic matter in the samples increased as the percentage of added motor oil increases. These increases eventually create a toxic environment for the earthworms which in turn reduces survivability for the earthworms.
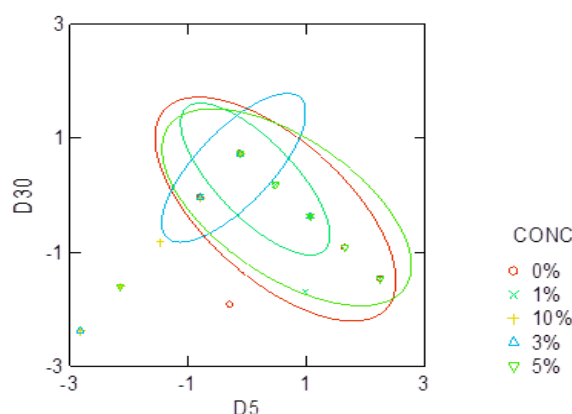

Figure 16. Comparisons of D5 and D30 against T_1-T_5[2]

Note: CONC means the different concentration %, D5 means survivability of earthworms in day 5 as a factor and D30 is the survivability of earthworms in day 30 of the experiment as a factor used in discrimination analysis. In this respect, the graph is representing two canonical variables as used by SYSTAT. The SYSTAT produces a canonical scores plot, in which the axes are the canonical variables, and the points are the canonical variable scores. This plot includes confidence ellipses for each group.

In the present research, an oil concentration of 10 % reduced survival of *Lumbriscus terrestris* (Tables 9 and 10). An oil concentration of 5 % did not reduce survival of *Lumbriscus terrestris* and from the limited data of the current study, it appears that *Lumbriscus terrestris* was better off in the used, motor oil since *Lumbriscusterrestris* survived 42 % for 30 days in 5 % used motor oil treatment and 32 % for 30 days in 5 % pure motor oil treatment. It was expected that *Lumbriscus terrestris* was going to survive more in the pure motor oil than in the used motor oil, because used motor oil contains metals depleted from the crankcase of the engine and chemicals generated in the process. These properties of the used motor oil should have hindered the survival of the earthworm Lumbriscus terrestris. As stated by Neuhauser and Hopkin.[24] There are no published studies on *Lumbriscus terrestris* for bioremediation of motor oil to compare to my laboratory

---

[2](T_1=0%, T_2=1%, T_3=3%, T_4=5%, T_5=10% Concentration of motor oil)

results but Shakir Hanna and Weaver[11] in their study on earthworm survival in oil-contaminated soil, used *Lumbriscus terrestris*. In this research, 17 % of *Lumbriscus terrestris* survived at an oil concentration of 1.5 % for 7 days, and none survived to the 10th day. This result is not in agreement with ours because 33 % *Lumbriscus terrestris* survived in an oil concentration of 5 %, for 30 days in pure motor oil and 30 days for the used motor oil.The concentration of organic matter at the end of the experiment was less than before the experiment may have been due to earthworm's activities on the soil. Bioremediation of motor oil reduced toxicity to *Lumbriscus terrestris.*
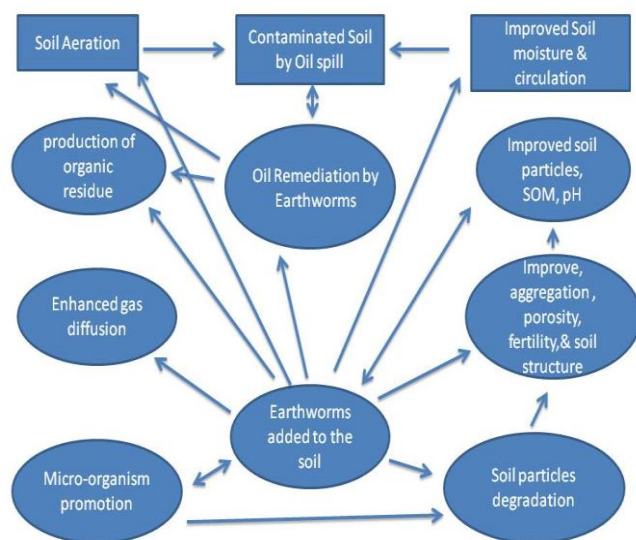
Figure 17. Graphic diagram showing the impact of earthworms as a biological agent for remediation of motor oil contaminated soil

In conclusion, research work on the use of earthworm to remediate soil contaminated with motor oil needs expansion. The limited studies carried out by author, and others indicate that the type of oil, soil and species of earthworm all influence the quantity of oil that can be tolerated in soil.[29-30] Future investigations need to be done to determine the toxicity of oil-contaminated soil on juvenile *Lumbriscus terrestris* and effects on reproduction. In addition, the influence of metals on earthworm needs to be addressed too.

Conclusions

There has not been much work on bioremediation using earthworms *Lumbriscus terrestris* for soil clean-up. The success of *Lumbriscus terrestris* in bioremediation is achieved only if the concentration of the contaminated site can be tolerated by the *Lumbriscus terrestris* in the soil. This study is to determine the concentration of the motor oil that the earthworms *Lumbriscus terrestris* can survive in, and maintain its natural pattern of activities, which eventually results in the process of clean-up. Shakir Hanna and Weaver[11] in their study on earthworm survival in oil-contaminated soil used *Lumbriscus terrestris*. In this research, 17 % of Lumbricus terrestris survived at an oil

concentration of 1.5 % for 7 days and none survived to the 10th day. But in my investigation, 33 % *Lumbriscus terrestris* survived in an oil concentration of 5 %, for 30 days in pure and used motor oil. Therefore it can be concluded that *Lumbriscus terrestris* can survive in motor oil contaminated soil for up to 30 days in a concentration of 5 % percent. At the end of the experiment, the carbon content of the soil samples were less than those before the activities of *Lumbriscus terrestris*. This implies that *Lumbriscus terrestris* can be used to clean-up the soil contaminated with motor with concentrations between 0-5 % and might not support the clean-up of concentrations higher than 5% of the contamination of motor oil be it used or pure. More studies need be conducted to determine the cause of fatality of earthworms in the oil contaminated soil because obviously, there would be other reasons for the fatality of earthworms. Studies should be extended to consider the accumulation of metals by not only *Lumbriscus terrestris* but also other species in naturally contaminated soils. What is required to progress this field and to increase the use of studies in bioremediation using macro-organism (*Lumbriscus terrestris*) is to study the effects of metals on the earthworms, determine soil properties (which should include pH, organic matter content, soil texture, cation exchange capacity). Kinetic studies are of particular importance as will suggest how long studies should be performed in the laboratory and provide more useful toxicological information than more straight forward bioremediation studies. It is important that studies are tested on different soils; individual studies usually define relationships but do not test them independently. More studies are required that generate earthworm interspecies comparison ratios thereby allowing application of data obtained for one species (and particular *Lumbriscus terrestris*) to other species.

Lastly, attempts should be made to perform experiments either in the field or terrestrial model ecosystems[23] in order that experimental constraints do not influence earthworm's response. In particular, the different ecological niches that earthworms occupy cannot be expressed in laboratory studies performed closely following some laboratory protocols.

References

[1]Maike, S., Soren, P. O., Juliane, F., Effects of Lumbricus terresris, *Allolobophora chlorotica* and *Eisenia fetida* on microbial community dynamics in oil-contaminated soil," *Soil Biol. Biochem.,* **2005**, *37*, 2065-2076. doi.org/10.1016/j.soilbio.2005.03.010

[2]Vazquez-Duhalt, R., Greppin, H., Biodegradation of used motor oil by bacteria promotes the solubilization of heavy metals. *Sci. Total Environ.,* **1986**, *52*, 109-121. https://doi.org/10.1016/ 0048-9697(86)90108-7

[3]Maugh, T. H. "Refined oil; an option that saves oil, minimizes pollution," *Science,* **1976**, *193*, 1108-1110.

[4]Wang, G. D., Chen, X. Y., Detoxification of soil phenolic pollutants by plant secretory enzyme, *Phytoremediation,* In*: Methods in Biotechnology Series, Animal Cell Biotechnology, Methods and Protocols*, Second Edition, Edited by John Walker, Humana Press, Totowa., **2007**, 49-57. DOI: https://doi.org/10.1007/978-1-59745-098-0_4.

[5]Driscoll, J. N., Hanby, J., Panaro,J., Calabrese P. T., J. B. E., Review of Field Screening Methodology for Analysis of Soils. *Hydrocarbon Contaminated Soils. 2*. Boca Raton: Lewis Publishers, Boca Raton, **1992**, *2*, 153–171.

[6]http://en.wikipedia.org/wiki/Microcosm_(experimental_ecosyststem).

[7]Peake, E., Parker, K., Polynuclear aromatic hydrocarbons and the mutagenicity of used crankcase oil, In: *Chemistry and Biological Effects*, P. A. H. in A. Bjorseth and J. Dennis (Eds..), Ed. Columbus, OH, Battelle Press, **1980**, 1025-1039.

[8]Stewart, R. G., Helm, J. L., *The lubricant market in the 1980s*. The US and the free world (AM-80-25), National Petroleum Refiners Association, Washington, DC, U.S.A., **1980**.

[9]National Petroleum Refiners Association, **1981** *Report on U.S. lubricating oil sales*, Washington, DC, U.S.A.

[10]Ismailov, N. M., Effect of oil population on the nitrogen cycle in the soil, *Mikrobiologiya*, **1983**, *52*,1003-1007.

[11]Kula, H., Larink, O., Tests on the earthworms Eisenia fetida and Aporrectodea caliginosa. In: *Handbook of Soil Invertebrate Toxicity Tests*. Eds. H. Lockke and C. A. Mvan Getsel. JohnWiley & Sones Ltd. Chichester, **1998**.

[12]Shakir Hanna, S.H., Weaver, R.W., Earthworm survival in oil-contaminated soil, *Plant and Soil*, **2002**, *240*, 127–132. **DOI:** https://doi.org/10.1023/A:1015816315477

[13]Vepraskas,M.J.. Redox potential Measurements. NC State University, **2002**, 1-17.

[14]SPSS Inc.SPSS *Base 8.0 for Windows User's Guide*. SPSS Inc., Chicago.**1998**. http://www.childrens-mercy.org/stats/ask…

[15]Base SAS 9.3, *Procedures Guides: Statistical procedures*. Copyright **2011** by SAS Int. Software, Inc.

[16]*SYSTAT 12. Getting started*. Copyright **2007** by SYSTAT software, Inc.

[17]*SPSS Science, S., Sigmaplot,* Version 8 SPSS Science, **2002**. www.spsscience.com/sigmaplot.

[18]*Matlab works Inc.*, **2009**.

[19]Sokal, R. R., Rohlf, F. J., *Biometry The Principles and practices of Statistics in Biological Research*: W.H Freeman and Company. NY **1995**.

[20]McDonald, J.H., *Handbook of biological statistics*. Sparky House, Publishing, Baltimore, Maryland U.S.A, **2009**, 313 p.

[21]Su, W., Wu, B., Cheng, W., Characterization and biodegradation of motor oil by indigenous Pseudomonas aeruginosa and optimizing medium constituents. *J. Taiwan Inst. Chem. Eng.,* **2011**,*42*, 689-695. https://doi.org/10.1016/j.jtice.2011.01.002.

[22]Daniel, V. A., *Environmental Biotechnology- A Biosystem Approach,* **2010**, 742 pp. Academic Press, Elsevier Science, USA

[23]Fitzpatrick, L.C., Muratti-Ortiz, J.F., Venables, B.J.,Goven, A.J., Comparative toxicity in earthworms Eisenia fetida and Lumbricus terrestris exposed to cadmium nitrate using artificial soil and filter paper protocols. *Bull. Environ. Contam. Toxicol,* **1996**, *57*, 63-66. DOI: https://doi.org/10.1007/s001289900156

[24]Neuhauser, E. F., Loehr, R. C., Milligan, D. L. and Malecki, M. R., Toxicity of metals to the earthworm *Eisenia fetida*. *Biol. Fertil. Soils*, **1985** *1*,149-152. **DOI:** https://doi.org/10.1007/BF00301782

[25]Spurgeon, D. J., Hopkins, S. P., Effects of metal-contaminated soils on the growth, sexual development, and early cocoon production of the earthworm *Eisenia fetida*, with particular reference to zinc. *Ecotoxicol. Environ. Safety,* **1996**, *35*, 86-95. https://doi.org/10.1006/eesa.1996.0085

[26]Spurgeon, D. J., Svendsen, D. J., Rimmer, C., Hopkin V. R. S. P., Weeks, J. M., Relative sensitivity of life-cycle and biomarker responses in four earthworm species exposed to zinc. *Environ. Toxicol. Chem.*, **2000**, *19*, 1800-1808. DOI: 10.1002/etc.5620190714.

[27]Cikutovic, M.A., Fitzpatrick, L.C., Venables, B. J., Goven, A.J., Sperm count in earthworms (*Lumbricus terrestris*) as a biomarker for environmental toxicology: effects of cadmium and chlordane. *Ecotoxicol. Environ.,* **1993**, *81*, 123-125. https://doi.org/10.1016/0269-7491(93)90076-Z

[28]Siekierska, E., Urbanska-Jasik, D., Cadmium effect on the ovarian structure in earthworm *Dendrobaena veneta* (Rosa). *Environ. Pollut.*, **2002**, *120*, 289-297. https://doi.org/10.1016/S0269-7491(02)00152-5

[29]Khalil, M. A., Abdel-Lateif, H. M., Bayoumi, B. M., Straalen, N. M. V., Analysis of separate and combined effects of heavy metals on the growth of *Aporrectodea caliginosa* (Oligochaeta; Annelida), using the toxic approach. *Appl. Soil Ecol.,* **1996**, *4*, 213-219. https://doi.org/10.1016/S0929-1393(96)00115-1

[30]Van Gestel, C. A., Van Dis, W. A., Dirven-V-van Breemen, E. M., Sparenburg, P. M., Baerselman, R., Influence of cadmium copper and pentachlorophenol on growth and sexual development of *Eisenia andrei* (Oligochaeta, Annelida). *Biol. Fertil. Soils*, **1991**, *12*, 117-121. DOI: https://doi.org/10.1007/BF00341486

ANTI-BACTERIAL ACTIVITY STUDIES ON TEXTILES MODIFIED WITH SILVER METAL, COPPER, ZINC AND MAGNESIUM OXIDES NANOPARTICLES

Nehad Hamdi[a], Doaa M. El-Mekkawi[b]*, Mohamed M. Selim[b], S. A. Hassan[c] and Amir Ezzat[c]

The anti-bacterial characteristics of different nano-structured metal and metal oxides modified cotton fabrics were investigated. In this study, silver metal, copper, zinc and magnesium oxides have been supported on bleached cotton fabrics. Reduction, wet method, sol gel and precipitation methods were used in the preparation of the antibacterial nanoparticles (NPs). The preparation of the antibacterial-loaded cotton was carried out in-situ and ex-situ by pad dry methods. Formation of the supported nanoparticles was confirmed using x-ray diffraction (XRD), scanning electron microscopy studies (SEM) and energy dispersive x-ray (EDX) analyses. Antibacterial studies on the supported nanoparticles were done on gram positive (Bacillus and S. aureus) and gram negative (E-coli) bacteria by agar diffusion method. The loaded antibacterial nanoparticles are effective against the bacteria under investigation. Under the given experimental conditions, the maximum inactivation performances of each loaded inorganic agent were investigated. The loaded fabrics show the following antibacterial performance order against *Bacillus subtilis* is Ag=CuO>ZnO>MgO. However, the activity order is CuO>Ag>ZnO=MgO against *S.aureus* and *E. coli*. The inactivation performances depend on the type, purity and the amount of antibacterial nanoparticles on the textile surfaces.

* Corresponding Authors
    Fax: (+202) 33370931
    E-Mail: doaa_egypt@yahoo.com
[a]   Textile Lab., Chemistry Administration, 12 Ramses st., Cairo, Egypt.
[b]   Physical Chemistry Department, National Research Centre, 33 EL Bohouth st., Dokki, P. O. 12622, Giza- Egypt.
[c]   Faculty of Science, Ain Shams University, Cairo, Egypt.

Introduction

Inorganic materials such as metal and metal oxides have extensively considered as promising antibacterial agents.[1-5] Several kinds of metals and metal oxides posses obvious killing abilities to most microbes even at very low concentrations.[6] Different metal, oxide or salt compounds, mostly based on silver, copper, zinc and magnesium kill microbes by binding to intracellular proteins and inactivating them. These materials can react with cell enzymes leading to either generating or catalyzing reactive oxygen species. Reactive oxygen can then induce an oxidative stress, damaging cellular proteins, lipids and DNA.[7] Recently, much attention has been paid on the loading of metal and metal oxides nanoparticles (NPs) onto cotton substrate due to their potential applications.[8-12] The modified cotton fabrics have exhibited excellent antimicrobial activities against bacteria.[7] There is a growing awareness of the use of antibacterial fabrics in the form of medical clothes, protective garments, and bed spreads to minimize the chance of the nosocomial infections.

In the last few years, environmental and technical efforts have been made to develop new efficient antimicrobial textiles. For example, silver is now used in a large number of commercial antimicrobial products, either as an isolated form, for fiber finishing or incorporation, or even already in fiber or fabric form,[13] Copper particles also show antifungal and antiviral properties.[14] Impregnation of cellulose textiles with copper salt, Cu-alginate or CuO nanoparticles

including release properties has been studied.[13-19] Different techniques to insert/deposit copper in cellulose fibers have been also proposed. Zinc oxide has also been explored as a powerful antibacterial agent.[7-13] The relation between the antibacterial activity versus the ZnO particles size was studied.[17] It was observed that the antibacterial activity is inversely proportional to the nanoparticles' size. Arouk et al. have developed a ZnO nanoparticle-chitosan composite to coat cotton fabrics in order to conjugate the antimicrobial power of ZnO and chitosan and even to overcome the lack of strong chemical bonding with textile substrates presented by chitosan.[20] Magnesium oxide nanoparticles has been also reported as an acceptable mild inorganic antibacterial agent due to its abundance and low cost.[21] It also can work in simple antibacterial conditions and safe materials to human beings.[22]

The aim of the present research is to prepare inorganic antibacterial-loaded cotton for antibacterial studies. The prepared nanoparticles act as antibacterial agent, while cotton act as a substrate which can be used to in many biomedical applications. Silver metal and metal oxides (CuO, ZnO and MgO) supported cotton have been prepared and characterized for the antibacterial applications. The antibacterial modified cotton fabrics were characterized by XRD, SEM and EDX. The killing abilities of the modified cotton fabrics were tested against Gram-negative *Escherichia coli* (*E. coli*) and Gram-positive *Staphylococcus aureus* (*S. aureus*) and *Bacillus subtilis* (*B. subtilis*) bacteria.

Experimental

Materials

All chemicals used were reagent-grade without further purification. Bleached cotton (100 % cotton bleached, woven fabric, 115 g/m^2), AgNO$_3$ (purity > 99%, Merck, Germany) trisodium citrate (TSC, ≥ 98%, Fluka,

Switzerland), sodium dodecyl sulfate (SDS, $\geq$ 98 %, Aldrich, U.S.A), agar culture medium (Oxoid, UK), CuSO$_4$.5H$_2$O ($\geq$ 99 %, Oxford, India), acrylic binder (purity > 99 %, Pachin – Obour Paints & Chemical Industries, Egypt), Zn(NO$_3$)$_2$.3H$_2$O and Mg(NO$_3$)$_2$ (> 98 %, Merck ,Germany), soluble starch ($\geq$ 98 %, WINLAB, UK) and NaOH (purity > 98 %, El Nasr for Intermediate Chemicals, Egypt) were used as received.

Preparation of cotton loaded with Ag metal nanoparticles

Silver metal nanoparticles were prepared by the reduction of silver ions using trisodium citrates (TSC) as reducing agent.[23] AgNO$_3$ solution was heated to boiling at 70 ºC and 10 mL of TSC solution (36×10^{-3} mol L^{-1}) were added drop by drop. During the process, the solution was mixed vigorously and heated until a pale yellow color appeared. Reduction of silver ions (Ag$^+$) to silver nanoparticles was evident in the colloid synthesis process, as the colorless solution became pale yellow with the formation of the silver nanoparticles. Next, the solution was removed from the heating and stirred until cooled to room temperature. Cotton fabric samples were then immersed in the prepared silver nanocolloids heated at 50 ºC and stirred rapidly for 30 min. The cotton samples subsequently were padded. The padding process ensured the solution was coated evenly, and the excess chemicals were removed. The padded samples were air dried and finally cured at 120 ºC for 3 min in a pre-heated curing oven. The preparation steps were repeated with different initial concentrations of AgNO$_3$ (0072, 0.018 and 0.0288 mol /l).

Preparation of CuO loaded textile

Copper oxide nanoparticles were prepared by sonochemical method as indicated previously.[24] Cotton woven fibers were first washed in a water bath containing 5 % of sodium dodecyl sulfate at 40 °C for 1 h. After rinsing with distilled water, the fibers were dried in vacuum at 60 °C for 24 h. Dry cotton (5×5 cm) was first soaked into 100 mL of aqueous solution of CuSO$_4$.5H$_2$O (4.8×10^{-4} mol L^{-1}) solution in a sonicated flask and irradiated for 10 min with Ultrasonic generator. Then 0.06 g of NaOH was added to the mixture while stirring. The mixture was then re-sonicated at 35 to 40 °C for 1 h, the strong blue color was gradually converted into brown after 15 min. The bath temperature was kept at a constant temperature around 40 °C. The product was then washed thoroughly several times with distilled water to remove any excess hydroxide and dried in vacuum at 60 °C overnight. The preparation experiment was repeated using different initial concentrations of copper sulphate (0.0012, 0.00192, 0.00216 and 0.0024 mol L^{-1}).

### Preparation of textile loaded with ZnO NPs

The zinc oxide nanoparticles were prepared by wet chemical method.[25] Zinc nitrate and sodium hydroxide were used as precursors while soluble starch was added as stabilizing agent. Soluble starch (0.1 %) was dissolved in 500 ml of distilled water then zinc nitrate was added. Then the solution was kept under constant stirring using magnetic stirrer till completely dissolve the zinc nitrate. After

complete dissolution of zinc nitrate, 0.2 M of sodium hydroxide solution (20 mL was used in our study) was added under constant stirring, drop by drop touching the walls of the vessel. The reaction was allowed to proceed for 2 h after complete addition of sodium hydroxide. After the completion of reaction, the solution was allowed to settle for overnight and the supernatant solution was then discarded carefully. The remaining solution was centrifuged at 35,000 rpm for 10 min and the supernatant was discarded. The obtained nanoparticles were washed three times using distilled water. Washing was carried out to remove the byproducts and the excessive starch that were bound with the nanoparticles. After washing, the nanoparticles were dried at 80 ºC for overnight. During drying, complete conversion of zinc hydroxide into zinc oxide takes place.

ZnO nanoparticles were applied on cotton using immersion method. The cotton fabric cut to the size of 5×5 cm was immersed in the solution containing ZnO (1 %) and acrylic binder (1 %) for 5 min and then it was padded. After padding, the fabric was air-dried and then cured for 3 min at 140 °C. The fabric was then immersed for 5 min in sodium dodecyl sulfate solution (2 g L^{-1}) to remove unbound nanoparticles. Then the fabric was rinsed at least 10 times to completely take out all the soap solution. The fabric was washed then air-dried. The loading procedure was repeated with different solutions containing different percentages of ZnO suspension (1, 2, 2.5, 4.5, 5 and 8 % w/v).[25]

Preparation of textile loaded with MgO

Magnesium oxide nanoparticles were prepared by wet chemical method.[26] Magnesium nitrate and sodium hydroxide were added to soluble starch as stabilizing agent. Starch act as a stabilizing agent and also prevents the agglomeration of nanoparticles. Starch (0.1 % w/v) solution was dissolved in 100 mL distilled water then magnesium nitrate was added to the above solution. Then the solution was kept under constant stirring using magnetic stirrer for complete dissolution of contents. After complete dissolution, 4 g (0.2 M) sodium hydroxide solution (25 ml) was added in drops along the sides of the container under constant stirring for 2 h and allowed to settle for 24 h. The supernatant liquid was then discarded carefully and the remaining solution was centrifuged (35,000 rpm at 25 °C) for 10 min. Centrifugate was washed three times using distilled water to remove the byproducts and the excessive starch that bound with the nanoparticles. The nanoparticles of magnesium hydroxide were placed in furnace at 300 °C. During this process, conversion of magnesium hydroxide into magnesium oxide takes place. The following reaction explains the formation of magnesium oxide nanoparticles.

$$Mg(NO_3)_2.6H_2O + 2NaOH \rightarrow Mg(OH)_2 + 2NaNO_3 \quad (1)$$

$$Mg(OH)_2 \rightarrow MgO + H_2O \quad (2)$$
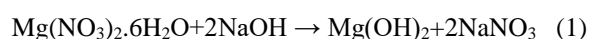
MgO nanoparticles were applied on cotton using immersion method. The cotton fabric cut to the size of 5×5 cm was immersed in the solution containing MgO (2 %) and acrylic binder (1 %) for 5 min and then padded. After padding, the fabric was air-dried and then cured for 3 min at 140 °C. The fabric was then immersed for 5 min in sodium

dodecyl sulfate solution (2 g L^{-1}) to remove unbound nanoparticles. Then the fabric was rinsed at least 10 times to completely take out all the soap solution. The fabric thus washed was air-dried. The loading procedure was repeated with different solutions containing different percentages of MgO suspension (3, 4 and 5 % w/v).

Characterization of the prepared samples

X-ray diffraction measurements

To determine the crystal phase composition of the synthesized samples, X-ray diffraction (XRD) measurements were taken using a Bruker D8 advance instrument with CuK$_{\alpha 1}$ target with secondary monochromator 40 kV, 40 mA. The reference data for the interpretation of the X-ray diffraction patterns were obtained from the International Centre for Diffraction Data Joint Committee on Powder Diffraction Standards ICDD-JCPDS card files. The crystallite size (*D*) determined by the Scherrer's formula: [27]

$$D = \frac{K\lambda}{\beta cos\theta} \qquad (3)$$

where

λ is the wavelength of X- ray radiation (CuK$_{\alpha 1}$= 0.15406 nm),

K is a constant taken as 0.89,

β is the line width at half maximum height (FWHM) of the peak, and

θ is the diffracting angle.

Scanning electron microscope

In SEM measurements, an electron beam was passed through the specimens followed by scattering them back as electrons and secondary electrons. Back scattered secondary electrons were used to form the image on the computer monitor. The acceleration of the electron beam was 10 kV. This was carried out on Quanta FEG250 Instrument.

Energy dispersive X-ray

The spectra of NP coated cotton fabrics were obtained by EDX measurements. A field emission scanning electron microscope (QUANTA FEG 250) coupled with an energy dispersive X-ray spectrometer (EDX) unit was employed to evaluate the elemental composition of NP/cotton sample. Semi-quantitative analyses in the inspection field were conducted using ZFA software where the energy of the emitted electrons for each element was counted in units of weight percent.

Antibacterial activity

The antibacterial activity was carried out by the agar diffusion method using the suspension of bacteria spread on nutrient agar. The swab was dipped into the broth culture of the organism and was gently squeezed against the tube inside to remove excess fluid. The swab used to streak agar plate or a nutrient agar plate for a lawn of growth. This is best accomplished by streaking the plate in one direction, then streaking at right angles to the first streaking, and finally streaking diagonally. End by using the swab to streak the outside diameter of the agar. The inoculated plates were incubated at appropriate temperature for 24 h. The supported fabric placed on the surface of the agar using a dispenser that dispenses multiple pieces at the correct distance apart, on the surface of the agar using flame sterilized forceps. The antibacterial activity was evaluated by measuring the zone of inhibition against the test organisms. Zone of inhibition is the area in which the bacterial growth is stopped due to bacteriostatic effect of the compound and it measures the inhibitory effect of compound towards a particular microorganism. Finally diameters of zones of inhibition (mm) were measured and illustrated.

Results and Discussion

XRD analyses

The XRD measurements of the prepared inorganic antibacterial agents were carried out. The estimated average crystals sizes and the purity of the samples were estimated. Figure 1 shows the x-ray diffractograms of Ag, CuO, ZnO and MgO, respectively. As shown in Figure 1, the diffractogram of Ag shows good agreement with the characteristic peaks of pure Ag.

The characteristic peaks of pure Ag appeared in the prepared sample at 2θ =10.54°, 15.02 °, 23.80 °, 28.43 °, 31.44 ° and 37.74 ° degrees. This data is consistent with the standard XRD data in Joint Committee on Powder Diffraction Standards (JCPDS) card file no. 74-1828. The calculated average crystal size of Ag using Scherrer relation is 64.8 nm. On the other hand, the characteristic peaks of pure CuO appeared at 2θ =35.48 °, 38.64 °, 48.64 °, 61.33 °, 66.97 ° and 79.56 ° degrees. The data matches the recorded peaks in JCPDS card no.48-1548. The calculated average crystal size of CuO is 5.8 nm. Further, the diffractograms of the prepared MgO NPs are in good agreement with the JCPDS data (89-7746).
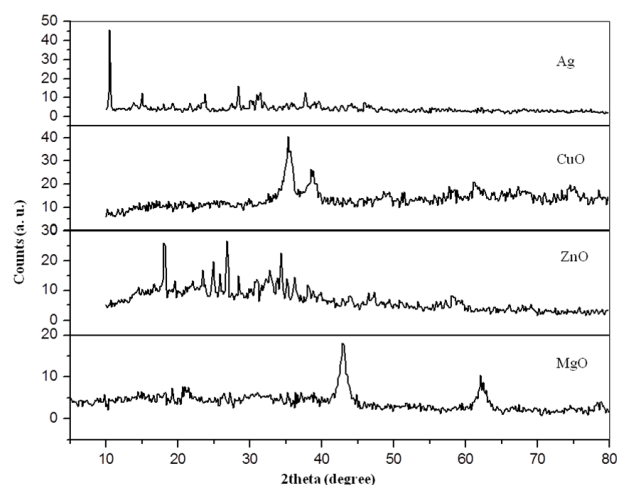

Figure 1. X-ray diffractograms of the prepared Ag, CuO, ZnO and MgO nanoparticles.

This indicates the formation of pure nanocrystalline MgO without any foreign material. The estimated average crystal size of MgO is 10.5 nm. However, XRD data of the prepared ZnO indicated the presence of foreign phases. Data indicated the formation of only 11.5 % zinc oxide phase. Characteristic peaks of zinc hydroxide and nitrate appeared and the estimated percentage of each phase was 33.5 and 55.0 %, respectively.

SEM and EDX analyses

The SEM micrographs of the supported inorganic agents on cotton fabric were measured. For example, the supported Ag nanoparticles are illustrated in Figure 2. As shown in Figure 2, the Ag nanoparticles appear to be homogeneously distributed on the cotton surface. On the other hand, EDX spectroscopy reveals the good binding of Ag to cotton surfaces. As shown in Figure 3, the characteristic signals of Ag atom were observed in the EDX spectra of Ag/cotton sheets. In addition, EDX data indicated that the percentage amount of Ag on cotton surfaces was 28.48 %.
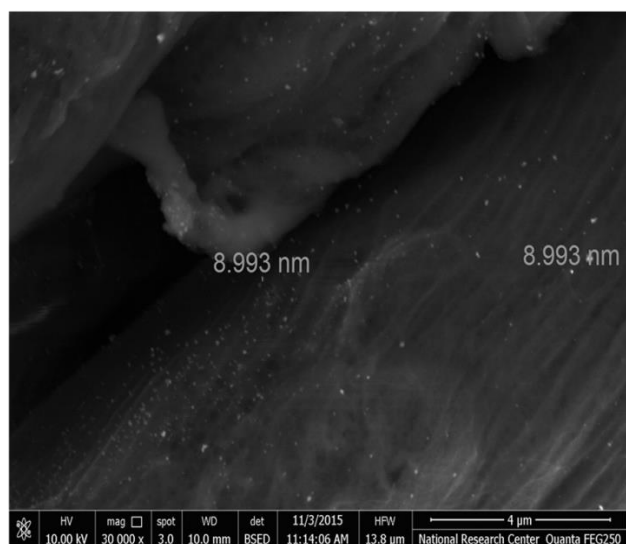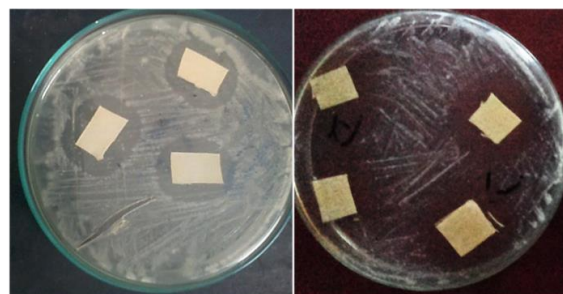

Figure 2. SEM image of Ag nanoparticles loaded on cotton.
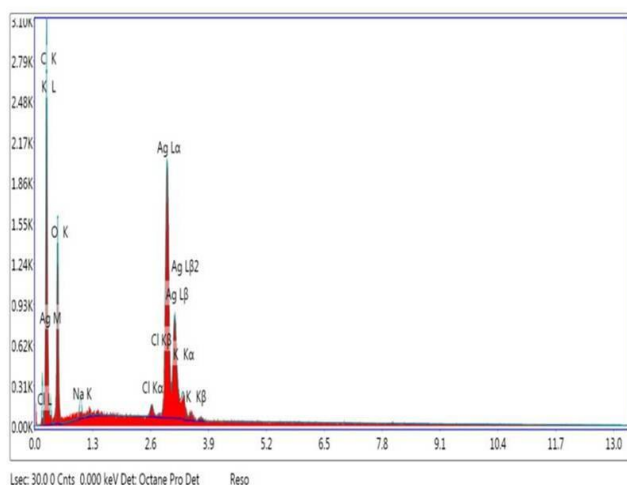
Figure 3. EDX spectra of Ag nanoparticles loaded on bleached cotton.

Antibacterial studies

Antibacterial activities of the loaded samples have been tested against gram positive (*B. subtilis* and *S. aureus*) and gram negative (*E. coli*) bacteria by agar diffusion method (Figure 4).

Figure 4. Zones of inhibition of zinc (left) and copper (right) oxides nanoparticles against a gram positive bacteria (*B. subtilis*).

Overall, results revealed different killing abilities of bacteria. It has been found that the inactivation performances depend on the type and the amount of antibacterial nanoparticles on the textile surfaces as well as the type of bacteria. First, the influence of the amount of the loaded antibacterial nanoparticles was investigated (Figure 5). The amount of loaded NPs was initially increased as previously illustrated in the experimental section. The amount of loaded MgO or ZnO were varied by initially increase the amount of suspended oxides during the loading processes. However, loading of Ag and CuO were carried in-situ. Therfore, the influence of the amount of loaded Ag or CuO were controlled by varying the initial amounts of the added AgNO$_3$ or CuSO$_4$, respectively. Generally, according to each loading procedure, the increase in the amount of the loaded NPs was proceeded till the maximum inhibition zones were acheived (i. e. no further increase in the inhibition zone upon increasing the amount of loaded NPs). This may be attributed to the maximum loading capacity of the cotton fabric toward the loaded NPs.

Contrary, in case of CuO, loading of CuO on cotton was acheived through the in-situ sonochemical conversion of copper sulphate into CuO in the presence of NaOH. Change of the characteristic blue color of copper hydroxide into the brown CuO was ceased when the initial concentration copper sulphate exceeds 0.0024 mol L^{-1}. Therefore, this concentration was taken as the maximum initial loading concentration.

As appeared in Figure 5a and b, by increasing the amount of loaded Ag and CuO, the inhibition zones increase toward all types of bacteria. In addition, both Ag and CuO show the highest killing abilities toward *B. subtilis*. Further, at low concentrations, Ag and CuO show different antibacterial activities toward *E-coli* and *S. aureus* with the order *S. aureus > E-coli*. However, at high concentrations, both agents show similar killing abilities. On the other hand, ZnO shows only high killing ability toward *B. subtilis* (Figure 5c). The inhibition zone increases upon increasing the initial concentration of ZnO from 1 % to 4 %. Further increase in ZnO concentration does not affect the inhibition zone. The zero antibacterial activity of ZnO toward *S. aureus* and *E. coli* is probably due to its low purity as previously indicated by the XRD analyses.

However, loaded MgO shows no killing abilities toward the three kinds of bacteria. It worthy to mention that preliminarily antibacterial activity tests of both MgO and ZnO in its powder form was tested against the three bacteria. The preparation of the oxide powders were carried out as previously discussed but in the absence of the cotton fabric. The unsupported ZnO powder showed lower activity against *S. aureus* and *E. coli* than that toward *B. subtilis*. However, MgO powder shows only very low antibacterial activities against all bacteria.
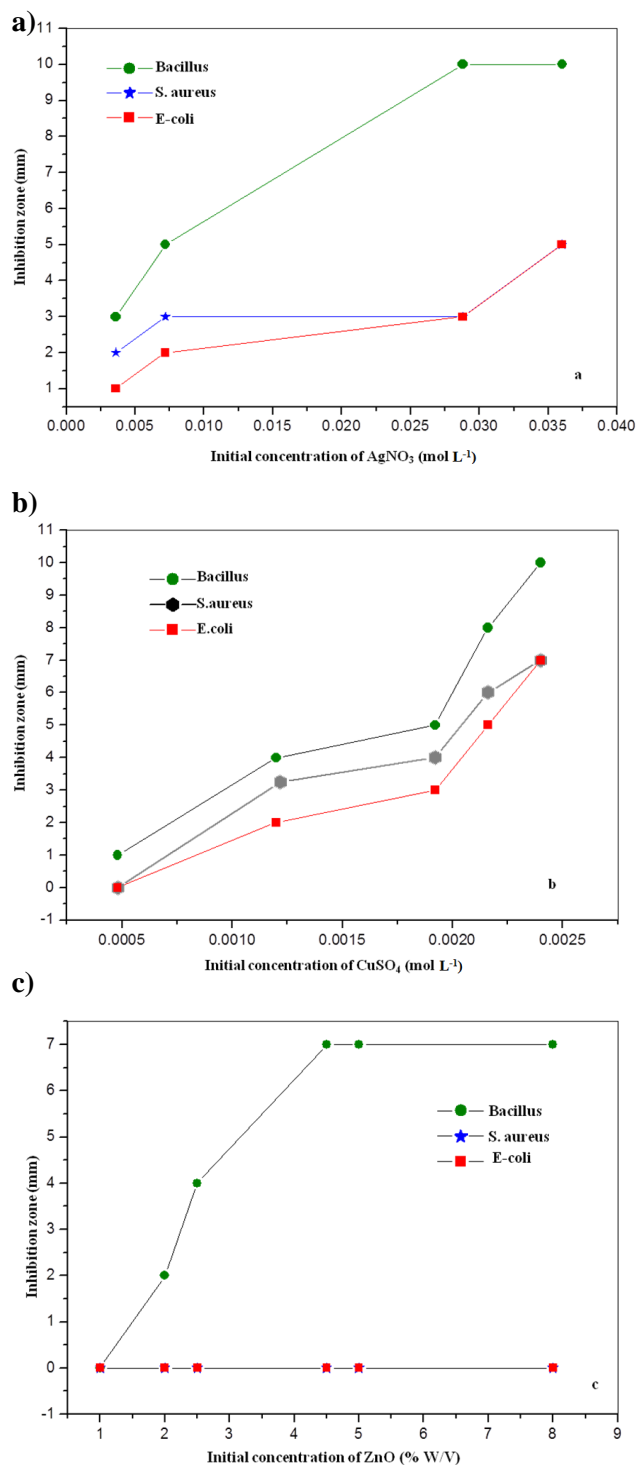
Obviously, loading of the inorganic antibacterial agents into textile fabrics leads to decrease in the amount of active agents and consequently decrease in their killing abilities (see for example the estimated amount of loaded Ag on cotton using EDX technique).

The maximum inactivation performances of each loaded inorganic agent against the three bacteria are illustrated in figure 6. Under the given experimental conditions, the loaded fabrics show the following antibacterial performance order against Bacillus: Ag=CuO>ZnO>MgO. However, the activity order is CuO>Ag>ZnO=MgO against *S.aureus* and *E.coli*.
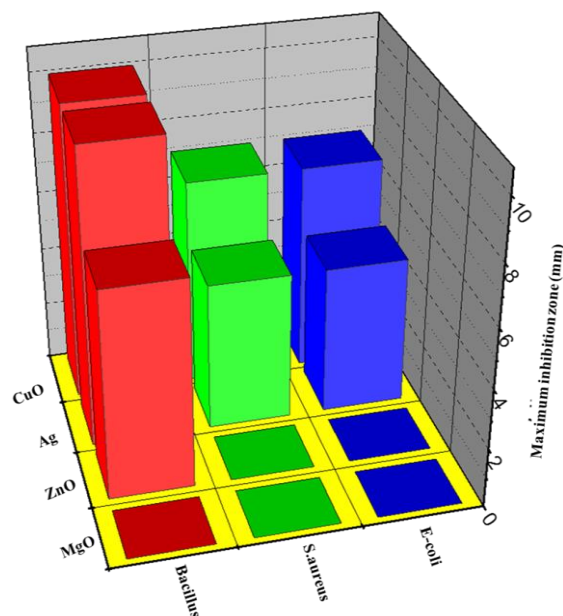
Figure 6 . The effect of the type of loaded inorganic agent on the antibacterial activity against *B. subtilis*, *B. subtilis* and *B. subtilis*.

The maximum inactivation performances of each loaded inorganic agent against the three bacteria are illustrated in figure 6. Under the given experimental conditions, the loaded fabrics show the following antibacterial performance order against *B. subtilis*: Ag=CuO>ZnO>MgO. However, the activity order is CuO>Ag>ZnO=MgO against *S.aureus* and *E.coli*.

Overall, the results revealed that not all of the active antibacterial agents in its powder form can be loaded into fabrics for the biomedical application purposes. It is not recommended to load fabrics with NPs that posses low antibacterial activities (such as MgO) as an adequate perfomances is not expected. One important issue that should be taken in consideration is the purity of the inorganic agents. The low purity of the prepared ZnO NPs negatively impacts the killing ability of the loaded samples.

Conclusion

Silver metal, copper, zinc and magnesium oxides have been supported on bleached cotton fabrics. Reduction, wet method, sol gel and precipitation methods were used in the preparation of the antibacterial nanoparticles. The formation of nanometer sized inorganic antibacterial agents was

Figure 5. The effect of the initial concentration of inorganic nanoparticles on the antibacterial activity of the loaded samples against *B. subtilis*, *E.coli* and *S.aureus*. (a) Ag, (b) CuO and (c) ZnO.

confirmed by XRD analyses. SEM measurements indicate the homogeneous distribution of NPs on the cotton surface. However, EDX spectroscopy reveals the good binding of NPs to cotton surfaces. As the initial concentrations of the loaded NPs increase, the killing abilities of bacteria increase. The zero antibacterial activity of ZnO toward *S. aureus* and *E. coli* is probably due to its low purity. Whereas, zero killing ability of loaded MgO is due to its very low antibacterial activity in its unsupported form. Under the given experimental conditions, the loaded fabrics show the following antibacterial performance order against *B. subtilis*: Ag=CuO>ZnO>MgO. However, the activity order is CuO>Ag>ZnO=MgO against *S. aureus* and *E. coli*. On the light of this work, it can concluded that the inactivation performances depend on the type, purity and amount of antibacterial nanoparticles on the textile surfaces.

Acknowledgement

References

[1]Sahooli, M., Sabbaghi, S., Saboori, R., *Matter. Lett.,* **2012**, *81*, 169–17.https:// doi: 10.1016/j.matlet.2012.04.148

[2]Khawla, K., Ghassan, S., Farah. A., *Arab. J. Sci. Eng*., **201**6, *41*, 301–310.doi:10.1007/s1336

[3]Ahamed, M., Siddiqui, M. A., Akhtar, M. J., Ahmad, I., Pant, A. B., Alhadlaq, H. A., *Biochem. Biophys. Res. Comm.* **2010**, *396*, 578–583. doi:10.1016/j.bbrc.2010.04.156

[4]Mortimer, M., Kasemets, K., Kahru, A., *Toxicology*, **2010**, *269*, 182–189. doi: 10.1016/j.tox.2009.07.007

[5]Rashu K, Harpeet K., Gurav S., Mu, N., Deepak, P., *J. Ind.., Eng. Chem.,* **201**5, *31*, 173–184. doi: 10.1016/j.jiec.2015.06.021.

[6]Jones, N., Ray, B., Ranjit, K.T., Manna, A.C., *FEMS Microbiol. Lett.,* **2008**, *279(1),* 71–76. doi:10.1111/j.1574-6968.2007.01012.x

[7]Lura K. A., Delina, Y. L., Pedro, J. J., *Water Res.,* **2006**, *40(19),* 3527–3532. doi: 10.1016/j.watres.2006.08.004.

[8]Zahran, M. K., Hanan. B. A., El Rafie, M. H., *Carbohyd. Polym.,* **2014**, *108*, 145-152. doi: 10.1016/j.carbpol.2014.03.005

[9]Hossam, E. E., Avinash, P. M., Barbora, S., Heinz, D., Petra, M., Bernhard, R., Thomas B., *Surf. Coat. Tech.,* **2014**, *254,* 344–351. doi:10.1016/j.surfcoat.2014.06.036

[10]Eunmi, K., and Kyung, H. H., *Dyes Pigments*., **2014**, *103*, 222-227. doi: 10.1016/j.dyepig.2013.09.015

[11]Rajendran, R., Balakumar, C., Hasabo, A., Ahammed, M., Jayakumar, S., Vaideki, K., Rajesh, E., *Int. J. Eng. Sci.,* **2010**, *2,* 202-208. doi: 10.4314/ijest.v2i1.59113

[12]Anita, S., Ramachandran, T., Rajendran, R., Koushik, C.V., Mahalakshli, M., *Text. Res. J.,* **2011**, *81*, 1091–1099. doi: 10.1177/0040517510397577

[13]Seil J. T., and Webster, T. J., *Int. J Nanomed.,* **2012**, *7,* 2767–2781. doi: 10.2147%2FIJN.S24805

[14]Zarrindokht E. K., Pegah C., *Afr. J. Microbiol. Res.,* **2011**, *5(12),* 1368–1373. doi: 10.5897/AJMR10.159

[15]Xie, Y., He, Y., Irwin, P. L., Jin, T., Shi, X., *Appl. Environ. Microb.,* **2011**, *77*, 2325–233. doi:10.1128/AEM.02149-10

[16]Krishna, R. R., Ranjit, T. K., Adhar, M., *Langmuir.,* **2011**, *27(7),* 4020–4028. doi: 10.1021/la104825u

[17]Pal, S., Tak, Y. K., Song, J. M., *Appl. Environ. Microb.,* **2007**, *73(6),* 1712–1720. doi: 10.1128%2FAEM.02218-06

[18]Lingling, Z., Yunhang, J., Vulang, D., Malclm, P., David, Y., *J. Nanopart. Res.,* **2007**, *9(3),* 479–489. doi:10.1002/9781118150887.ch13

[19]Peng, X., Palma, S., Fisher, N. S., Wong, S. S., *Aquat. Toxicol.,* **2011**, *102(3),* 186–196. doi: 10.1016/j.aquatox.2011.01.014

[20]Hebeish, A., Sharaf, S., Farouk, A., *Int. J. Biol. Macromol.,* **2013**, *60*, 10–17. doi: 10.1016/j.ijbiomac.2013.04.078

[21]Di, D. R., He, Z. Z., Sun, Z. Q., Liu, J., *Nanomedicine UK.,* **2012**, *8,* 1233–1241. doi: 10.1016/j.nano.2012.02.010

[22]Banele, V., Phumlan, T., Poslet, M. S., Jane, C.N., Lucky, Richard, M., *J. Biomater. Nanobiotechnol*., **2013**, *4,* 365-373. doi: 10.4236/jbnb.2013.44046

[23]Srimala, P., Bharat, B., Rathnayake, B., Gamini, R., Sanath, R., Chaturanga, B., *Colloids. Surf. A.,* **2013**, *436,* 975– 989. doi:10.1016/j.colsurfa.2013.08.038

[24]El-Nahhal, M. I., Shehata, Z. M., Fawzi, K. S., Mohamed, S., Isabelle G., and Florence, B., *Int. Nano. Lett.,* **2012**, *2,* 62-67. doi:10.1186/2228-5326

[25]Rajendran, R., Balakumar, C., Hasabo, A., Jayakumar, S., Vaideki K., and Rajesh, *Int. J. Eng. Sci.,* **2010**, *2(1),* 202- 208. doi: 10.4314/ijest.v2i1.59113

[27]Sundrarajan, M., Suresh, J., Rajiv, R. G., *Dig. J. Nanomater. Bios.,* **2012**, *7,* 983 – 989.

[28]Patterson, A. L., *Phys. Rev.,* **1939**, *56*, 978–982. **doi**: **10.1103/PhysRev.56.978**

EFFECT OF GAMMA RADIATION ON A MIXED DYE FILM AND ITS POSSIBLE USE AS A RADIATION DOSIMETER

Sayeda Elewa Eid[a], Abdel Gawad Mohamed Rabie[b], Seif El-Din Ebraheem[a] and Asmaa Sobhy[a]*

Keywords: Poly(vinyl alcohol), chlorophenol Red, Quinaldine Red, dosimetry.

Dyed poly(vinyl alcohol) (PVA) films prepared by a simple technique of casting aqueous PVA solution incorporating a mixture of two dyes namely chlorophenol red (CPR) and Quinaldine Red (QR) on a horizontal glass plate are useful as high dose dosimeter in the dose range 2-30 kGy range. The colour of these films change from deep red to yellow when exposed to gamma radiation. Chloral hydrate was added with different concentrations. The response of the prepared films can be modified either by change of chloral hydrate concentration or ratio of the two dyes. As a result, these films can be used as a dosimeter in two dose ranges. The dosimetric parameters, e.g.; dose response, effect of relative humidity on response as well as pre- and post-irradiation stability of these films have been investigated.

* Corresponding Authors
    Fax: 022748188
    E-Mail: asmaa.sobhy@hotmail.com
[a]   National Center for Radiation Research and Technology (NCRRT), P.O. Box; 29 Nasr City, Egypt.
[b]   Faculty of Science Ain Shams University, Egypt.

Introduction

Ionizing radiation is commonly used for industrial applications of food preservation, blood irradiation, and medical devices sterilization. Such applications require dosimeters with higher accuracy to quantify the absorbed doses and indicators to detect visually the radiation exposure. Many dyed poly films had been developed and investigated for possibility of their being used to measure absorbed dose in nuclear reactors and doses of X rays, gamma rays and electron beam.[1-6] Recently a new thin plastic film dosimeter has been prepared from poly vinyl alcohol mixing with dyes. This film is considered to be as radiation dosimeter of promise.[7] Dyed polymer films of PVA-QR and poly(vinyl butyral) (PVB) containing QR are useful as routine high dose dosimeter. These flexible plastic film dosimeters are bleached when exposed to gamma rays. Films of PVA or PVB dyed with QR are useful dosimeter in dose range 10-90 kGy and 30-200 KGy respectively.[8] PVA containing CPR and chlorine containing substance (chloral hydrate) is useful for low doses application. CPR in PVA films change its color from purple to yellow by irradiation and the useful dose range extend up to 3.5 kGy.[9] New radiation sensitive indicators consisting of PVA film containing pH indicator dye and a water soluble chlorine containing substance have been developed.[10] Mixed dye film containing 2,6-dichlorophenol indophenol sodium salt and Cresol Red was investigated to be useful dosimeter in dose range up to 17 kGy and another dose range up to 50 kGy.[11]

The main goal of the present work is the investigation of mixed dye film of two dyes chlorophenol red (CPR) and Quinaldine Red (QR) to be a dosimeter for sterilization, also it describes the influence of humidity during irradiation as well as stability before and after irradiation on the film response.

Experimental

Preparation of stock solution dyes

The stock solution of QR indicator (product of E-Merck, Molecular Weight 430.352) was prepared by dissolving 0.08 g in 50 mL 95 % ethanol. The stock solution of sodium salt of CPR indicator (products of Sigma & Aldrich, molecular weight 423.27) was prepared by dissolving 0.08 g CPR in 1.9 mL of aqueous solution of 0.1 N NaOH, then the volume was completed by 95 % ethanol in a 50 mL volumetric flask.

Preparation of CPR/QR /PVA mixed dye films

Films were prepared by dissolving 9 g of PVA (average M.wt 125,000, fully hydrolyzed 99-100 % product of Sigma) in 180 mL of double distilled water. Complete dissolution was attained by stirring for 3 h at 60 ºC followed by continuous stirring for 2 h at room temperature and then left to cool.

The polymeric solution was divided into six parts, each of 30 mL volume to prepare six films. The first three parts contain 4 mL of CPR, 2 mL of QR from stock solution of both dye and different chloral hydrate concentrations as (0.2, 0.3, 0.4 g) respectively. The other three parts contain 2 mL CPR and 4 mL QR from stock solution of both dyes and different chloral hydrate concentrations as (0.2, 0.3, 0.4 g) respectively.

All solutions were well–stirred at room temperature for about 3 h in order to obtain an uniformly mixed solution. Each solution was poured on 15x15 horizontal glass plate and dried at room temperature for about 48 h, after stripping the films were cut into 1x1 cm pieces. Then films stored in dark at room temperature for further investigation. The thickness of the films was found to be 0.03±0.005 (σ). Six polymer films were obtained; three of them contain 0.42 phr (part per hundred) CPR and 0.21 QR phr and 13.2, 19.8, 26.4 phr chloral hydrate. The other three films contain 0.21 phr CPR and 0.42 phr QR and 13.2, 19.8, 26.4 phr of chloral hydrate.

Irradiation sources (γ-irradiation)

The Gamma chamber 4000A ^{60}Co irradiation facility (manufactured at Bhabha Atomic Research Center, India) is a compact and self-contained irradiation unit offering an irradiation volume of approximately 4000 cm^3. The activity of this irradiation facility was 15,000 Ci at the time of installation (15 June 2006). The source cage holds the radiation source pencils vertically and symmetrically along its periphery. The cage can hold a maximum of 48 pencils. Each pencil contains seven aluminium cladded ^{60}Co slugs.

The sample chamber is the central part of the drawer and has 16 cm inside diameter and 21 cm height. The central drawer is raised or lowered by means of an electric motor. The movement of the central drawer is controlled from the control panel of the irradiation chamber, which incorporates an analogue timer.

The absorbed dose rate in the irradiation facility 400A was measured by using reference alanine dosimeter and was found to be in the range 2.25 to 2.1 kGy h^{-1} during the overall time period of the experimental part.

UV/VIS spectrophotometer

The absorption spectra of non-irradiated and irradiated films were measured throughout the wavelength range 200-800 nm using UVIKON860 spectrophotometer. These films were placed into the holder designed especially for reproducible fitting into the sample beam of the instrument. The absorbance spectra were scanned to determine the wavelengths (nm) of the maximum absorbance (λ_{max}) and the change in absorbance for UV/VIS spectra were recorded.

Results and Discussion

Absorption spectra

The absorption spectra of the PVA film containing a mixture of 0.42 phr of CPR and 0.21 phr of QR in presence of 26.4 phr chloral hydrate were recorded before and after irradiation. The spectrum of the above film is represented in Figure 1 for non-irradiated and irradiated film of different absorbed doses.

The absorption spectrum of the non-irradiated film shows a main absorption peak in the visible region peaking at 586 nm characteristic of the dark red colour composed from both QR and CPR dyes. The colour of the film changes from dark red to yellow. At the beginning of irradiation gradual decrease in absorbance at 586 nm takes place due to the bleaching of QR, At 4 kGy orange colour appears due to the radiolysis product resulting of chloral hydrate which in turn leads to gradual transformation of CPR to its acidic form.

Complete irradiation of this film leads to complete bleaching of QR and complete transformation of CPR to acid form at 18 kGy. It has been previously reported that complete transformation to acidic form for CPR occurs at 3-5 kGy**Hiba! A könyvjelző nem létezik.** and complete bleaching of QR up to 90 kGy.**Hiba! A könyvjelző nem létezik.** In the present work, the dose range of CPR was

extended to be 18 kGy and that of QR to 18 kGy. This behaviour is attributed to the high sensitivity of QR towards radiolysis products, so it was consumed in the degradation process and causes retardation of the transformation of CPR.
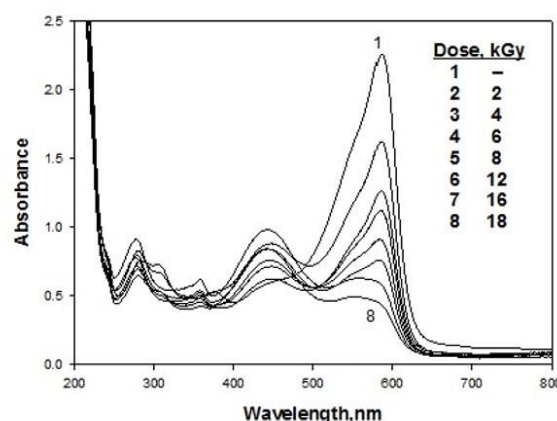
Figure 1. The absorption spectra of CPR/QR/PVA containing chloral hydrate for non-irradiated and irradiated films to different absorbed doses. [CPR]= 0.42 phr, [QR] = 0.21 phr, [Chloral hydrate] = 26.4 phr.

Figure 2 shows the absorption spectra for the PVA film contains a mixture of 0.21 phr CPR and 0.42 phr of QR in the presence of 26.4 phr chloral hydrate. The absorption spectra of non-irradiated and irradiated film show a main absorption peak at 548 nm. Gradual decrease in absorbance at 548 nm without any appearance of yellow color, indicating that the complete consuming of radiolysis products in bleaching reaction of QR only.
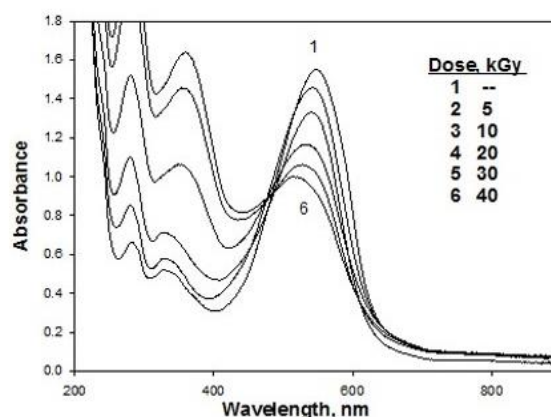
Figure 2. The absorption spectra of CPR/QR/PVA containing chloral hydrate for non-irradiated and irradiated films to different absorbed doses. [CPR]= 0.21 phr, [QR] = 0.42 phr, [Chloral hydrate] = 26.4 phr.

Response curve

Figure 3 shows the dose response curves of three films containing 0.42 phr of CPR and 0.21 phr of QR in presence of different chloral hydrate concentrations (13.2, 19.8, 26.4 phr).

The response curves were established in terms of change in optical density measured at 586 nm per unit thickness ΔA mm^{-1} against the absorbed dose ($\Delta A = A_0 - A_i$), where A_0 and A_i are values of optical absorbance at 586 nm for non-irradiated and irradiated films respectively. Each point on

the response curve represents the mean average of the three measurements (three dosimeter films irradiated to the same dose). It can be noticed that all the curves show the same trend, but they differ in slope value. The slop value increases with the increase of chloral hydrate concentrations.
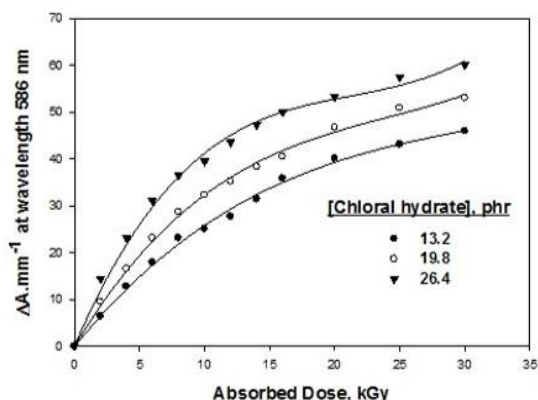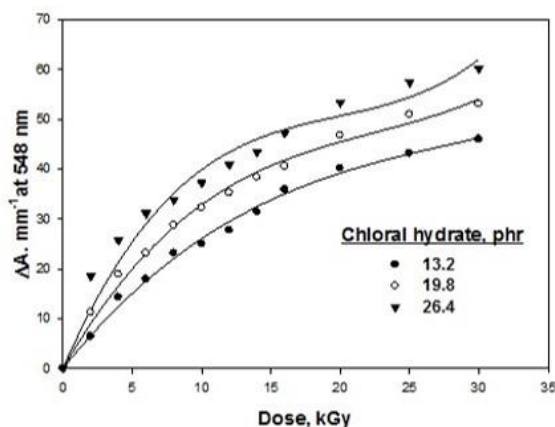

Figure 3. Change of $\Delta A.mm^{-1}$ of CPR/QR/PVA films containing different chloral hydrate concentrations. [CPR]= 0.42 phr, [QR] = 0.21 phr, at λ_{max}= 586 nm.

Figure 4 shows the dose response curve of another three films containing 0.21 phr of CPR and 0.42 phr of QR and different of chloral hydrate concentrations 13.2, 19.8, 26.4 phr at wavelength 548 nm. It is noticed that the response value increases with the increases of chloral hydrate concentrations and reach saturation at different absorbed doses depending on the chloral hydrate concentrations.


Figure 4. Change of $\Delta A \ mm^{-1}$ of CPR/QR/PVA films containing different chloral hydrate concentrations. [CPR]= 0.21 phr, [QR] = 0.42 phr, at λ_{max}= 548 nm.

From the present study, we can concluded that the preferred concentration of both dyes was 0.42 phr CPR and 0.21 phr QR, in which the degradation reaction and acidic formation takes place, the color change from red to yellow is obviously illustrated.

Humidity during irradiation

The effect of relative humidity (RH) during irradiation on response of CPR/ QR/PVA film, [CPR] = 0.42 phr, [QR] = 0.21 phr and [chloral hydrate] = 26.4 phr was investigated

by irradiating the films to a dose of 10 kGy at different relative humidity (0, 33, 54, 76, 92 and100 % RH). The different relative humidity was maintained by using different saturated salt solutions.[12] The films were stored before irradiation for 48 h period under the same relative humidity conditions as maintained during irradiated, so that the equilibrium moisture content in dosimeter is established during irradiation.
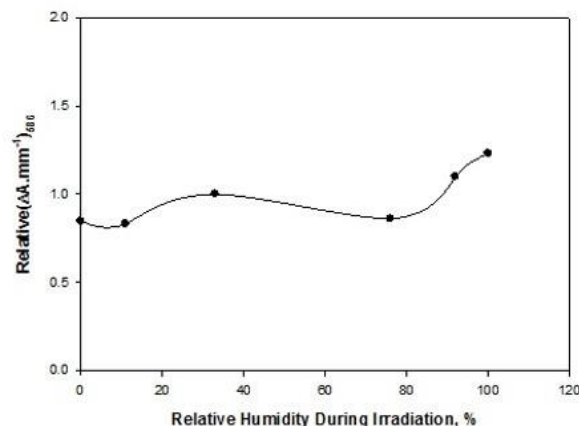
Figure 5. Variation in response ($\Delta A \ mm^{-1}$) of CPR/QR/PVA films as a function of relative humidity during irradiation. λ_{max}= 586 nm, dose= 10 kGy.

Figure 5 shows the variation in response ($\Delta A \ mm^{-1}$) as a function of percentage relative humidity during irradiation relative to that at 33 %. It can be seen that there is no appreciable effect of RH on the response in the range from 0-75 % RH. At higher RH more than 75 % the response increase gradually with increase of RH up to 92 % by 1.5 % . To avoid the effects of higher humidity levels, the films should be stuffed and sealed under controlled humidity conditions in the range 0-75 % or, if that impractical, one should maintain conditions of calibration as close as possible to the conditions of use.

Pre-irradiation stability

The colour stability of CPR/QR/PVA film was tested before irradiation by storing the film at 35 % RH at room temperature under laboratory fluorescent light and in the dark.
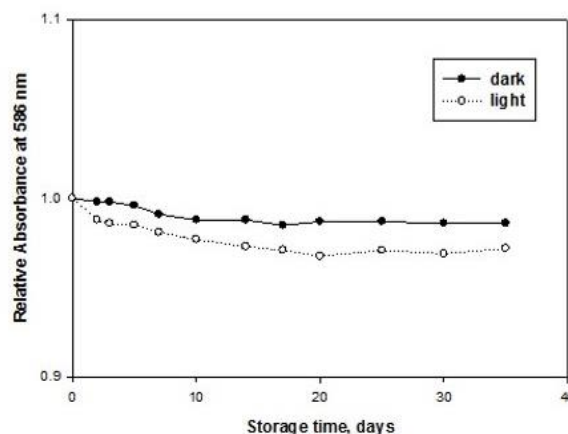
Figure 6. Pre-irradiation stability of CPR/QR/PVA films in terms of relative change in absorbance as a function of storage time.

Figure 6 represents the change in relative absorbance of the tested film, by measuring the absorbance at 587 nm at different time intervals during the storage period of 30 days. It can be seen that, the film exhibits excellent stability before irradiation, where the variation in the absorbance during the 30 days storage period is less than ± 3.2 % at light and less than ± 1.4 % at dark.

Post irradiation stability

Film of CPR/QR//PVA containing chloral hydrate, [chloral hydrate] = 26.4 phr irradiated to 10 kGy was stored at 35 % RH, room temperature (25 °C) under laboratory fluorescent lights and in the dark. The absorbance of the film was measured at 586 nm wavelength at different intervals time during the post- irradiation storage period of 30 days. The change in absorbance at 586 nm wavelength as a function of storage time relative to that before storage is shown in figure7. From the figure, it can be seen that, the absorbance of the film at 586 nm decrease gradually with nearly 2 % in the dark and 5 % at light during the first week then the absorbance tends to be stable up to the end of the storage period.
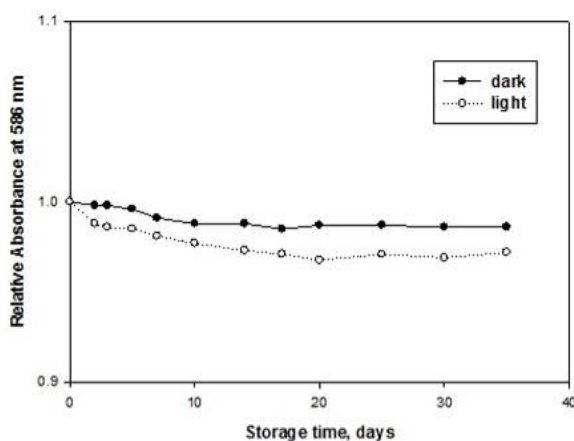
Figure 7. Post-irradiation stability of CPR/QR/PVA films in terms of relative change in absorbance as a function of storage time.

Conclusion

By irradiating CPR/QR/PVA films containing chloral hydrate, the colour changes from dark red to yellow indicating the acid formation. These films can be used as dosimeter in dose range 0-18 kGy. Two reactions occur in this film, first is bleaching reaction of QR and then acid formation of CPR. At 3 kGy colour change to orange due to radiolysis product resulting from chloral hydrate causes the gradual transformation of CPR to its acidic form. Then upon irradiation complete bleaching of QR and complete transformation of CPR to acid form till 18 kGy.

Addition of QR to CPR increase the dose range to 18 kGy instead of 3.5 kGy in case of CPR films and decrease the dose range to 18 kGy instead of 90 kGy in case of QR films. The best dyes ratio were 0.42 phr CPR and 0.21 phr QR, in which the degradation reaction and acidic formation takes place. The dose range depends on the chloral hydrate concentrations. The films have negligible humidity effects in range of 0-75 % RH as well as good pre and post irradiation stability. These films are easy to prepare so it is useful to use in large scale production and application for routine irradiation processes in moderate and high dose irradiation.

References

[1]Abdel-Rehim, F., Miller, A. McLaughlin, W. L., *Radiat., Phys. Chem.*, **1985,** *25*, 767-775.

[2]Abdel-Rehim, F., Ebraheem, S., Souka, N., *Radiat. Phys. Chem.*, **1992**, *39*, 191-195.

[3]Abdel-Rehim, F., Ebraheem, S., Wei-Zhen B.A., McLaughlin, W. L., *Appl. Radiat. Isot*., **1992**, *43*, 1503-1510.

[4]Abdel-Fattah, A. A., Ebraheem S., El-Kelany, M., Abdel-Rehim, F., *Appl. Radiat. Isot.*, **1996a**, *47*, 345-350. http://dx.doi.org/10.1016/0969-8043(95)00266-9

[5]Abdel-Fattah, A. A., Miller, A., *Radiat. Phys. Chem.*, **1996,** *47*, 611-621. http://dx.doi.org/10.1016/0969-806X(95)00037-x

[6]Kattan, M., Daher, Y. Alkassiri, H., *Radiat. Phys. Chem.*, **2007,** *76*, 1195-1199. https://doi.org/10.1016/j.radphyschem.2006.12.004

[7]El-Kelany, M., Gafar, S. M., *Optik,* **2016,** *127*, 6746-6753. http://dx.doi.org/ 10.1016/j.ijleo.2016.05001.

[8]Beshir,W. B., Eid, S., *Open J. Polym. Chem*., **2012,** *2*, 113-116. http://dx.doi.org/10.4236/ojpchem.2012.23015.

[9]Eid, S., Beshir, W. B. Ebraheem, S., *J. Rad. Res. Appl. Sci*., **2010**, *4 (1A)*, 45-57.

[10]Eid, S., *Arab J. Nucl. Sci. Appl*., **2008**, *41*(2), 28-37.

[11]Ebraheem, S., Eid, S., Kovacs, A., *Radiat. Phys. Chem.*, **2002,** *63*, 807-811.

[12]Levine, H., McLaughlin, W. L. Miller, A., *Radiat. Phys. Chem.*, **1979,** *14*, 551-574.

SYNTHESIS AND CHARACTERIZATION OF N-[3-(DIMETHYL-AMINO)PROPYL]METHACRYLAMIDE/(NANO-SiO₂, AMINE-MODIFIED NANO-SiO₂ AND EXPANDED PERLITE) NANOCOMPOSITE HYDROGELS

Fatma Özge Gökmen[a,b]* and Nursel Pekel Bayramgil[a]

The nanocomposite hydrogel of N-[3-(dimethylamino)propyl]methacrylamide (DMAPMAAm) with different SiO₂ particles were prepared by free radical polymerization. The nano-SiO₂ as reinforcement material was used in original, hydrophilic and perlite forms. The swelling values of nanocomposite hydrogels containing amine-modified nano-SiO₂ were found to be higher than those of the original DMAPMAAm hydrogel and the nanocomposite hydrogel containing original SiO₂. SEM and mapping studies with SEM proved the presence of nano-SiO₂ particles incorporated into the hydrogel structure.

* Corresponding Authors
    Fax: +902282141427
    E-Mail: fatmaozge.gokmen@bilecik.edu.tr
[a]   Hacettepe University, Chemistry Department, Ankara, Turkey
[b]   Bilecik Şeyh Edebali University, Central Research Laboratory, Bilecik, Turkey

INTRODUCTION

Hydrogels are three dimensional hydrophilic polymer networks capable of swelling in water or biological fluids, and retaining a large amount of fluids in the swollen state.[1-4] Their ability to absorb water is due to the presence of hydrophilic groups such as –OH, –CONH–, –CONH₂, – COOH, and –SO₃H.[5] The water content in the hydrogels affects different properties like permeability, mechanical properties, surface properties, and biocompatibility. Hydrogels have physical properties similar to that of living tissue, and this similarity is due to the high water content, soft and rubbery consistency, and low interfacial tension with water or biological fluids.[6-8]

Several techniques have been reported for the synthesis of hydrogels. The first approach involves copolymerization/crosslinking of co-monomers using multifunctional co-monomer, which acts as crosslinking agent. The polymerization reaction is initiated by chemically. The polymerization reaction can be carried out in bulk, in solution, or in suspension. The second method involves crosslinking of linear polymers by irradiation, or by chemical compounds.[9-12]

The monomers used in the preparation of the ionic polymer network contain an ionizable group, a group that can be ionized, or a group that can undergo a substitution reaction after the polymerization is completed. As a result, hydrogels synthesized contain weakly acidic groups like carboxylic acids, or a weakly basic group like substituted amines, or a strong acidic and basic group like sulfonic acids, and quaternary ammonium compounds. Some of the commonly used crosslinking agents include N,N'-methylenebisacrylamide, divinyl benzene, and ethylene glycol dimethacrylate. For co-polymerization/crosslinking reactions in solution, ionic or neutral monomers are mixed with the multifunctional crosslinking agent. The polymerization is initiated by UV, by redox initiator system or thermally. The presence of solvent serves as heat sink, and minimizes temperature control problems. The prepared hydrogels need to be washed with distilled water to remove the unreacted monomers, crosslinking agent, and the initiator.[13,14]

In this study, N-[3-(dimethylamino)propyl]methacrylamide (DMAPMAAm) was used as a monomer. Nano-SiO₂ was added to the solution of DMAPMAAm with the crosslinking agent and initiator and crosslinked disk shaped nanocomposite hydrogels were obtained. The nano-SiO₂ used as reinforcement material is in both original and hydrophilic forms (amine-modified) and were commercially purchased. In the preparation of nanocomposite hydrogels, DMAPMAAm monomer was preferred because of its biocompatibility feature.
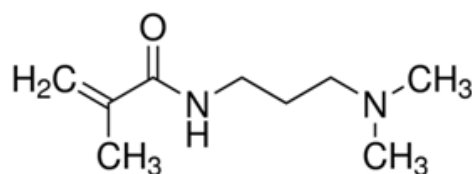
Fig. 1. N-[3-(dimethylamino)propyl]methacrylamide (DMAPMAAm).

All of the selected materials have been chosen in consideration of the fact that they are harmless to the environment and can work in harmony with the human body. After the behavior of nano-SiO₂ in hydrogels was determined, the volcanic rock type Perlite, which is common in nature and cheaper than the commercial cost of nano-SiO₂, is doped to DMAPMAAm hydrogels.

Table 1. Percent swelling (*S* %) values of nanocomposite hydrogels.

DMAPMAAm											
Plain			Neutral nano-SiO$_2$ doped			Amine-modified nano-SiO$_2$ doped			Expanded perlite doped		
C, %	*CL* %	*S* %	*C* %	*CL* %	*S* %	*C* %	*CL* %	*S* %	*C* %	*CL* %	*S* %
92.07	49.65	1331	92.00	71.09	715.0	85.14	77.04	1620.0	81.83	49.85	1798.0

Conversion, % (*C*) : 100*(m$_1$/m$_0$); Crosslink % (*CL*, gelation %) = 100 *(m$_2$/m$_1$'); Swelling degree (*S* %) =100*[m$_t$-m$_2$)]/m$_2$; [Monomer + Crosslinker + Initiator+(nanoparticles)] = *m$_0$*; Mass of dry hydrogel = *m$_1$*; Mass of 3 or 4 pieces of dry hydrogel = *m$_1$'*; Mass of 3 or 4 pieces of hydrogel after washing and drying = *m$_2$*; Mass of swollen hydrogel at time "*t*" = *m$_t$*.

The perlite design of the polymer/clay nanocomposite is due to the fact that its high SiO$_2$ content (~75 %) and the purity is rather high compared to other clays. This allowed us observe the behaviour of SiO$_2$ in perlite form and compare the results with those of pure nano-SiO$_2$ in the nanocomposite hydrogel structure.

EXPERIMENTAL

Neutral nano-SiO$_2$ (15-20 nm, 99.5 %, Skys nanomaterials), hydrophilic nano-SiO$_2$ with amine groups via long alkyl chains (10-20 nm, 99.8%, Skys nanomaterials), expanded perlite (EP) (ETİ Mine Operations), DMAPMAAm (Sigma-Aldrich), N,N'-methylenebisacrylamide (N,N'-MBAAm) (Sigma-Aldrich) and azobisisobutyronitrile (AIBN) (Merck) were used as supplied.

Preparation of hydrogels

The crosslinked cylindrical hydrogels were prepared by using DMAPMAAm monomer in PVC straws. The hydrogel solution containing monomer, initiator, crosslinking agent, solvent, and nanoparticles was heated in a temperature-controlled water bath (at 80 °C) for 2 h. Then, the PVC straws were carefully removed from bath, cut into cylindrical discs (3-4 mm in length) with a knife, and the hydrogels were dried in air before kept in vacuum oven (35 °C).

Swelling properties

Percent swelling (*S* %) values of nanocomposite hydrogels were calculated using the following equations, where m$_0$ is the initial mass of dry hydrogel, m$_t$ is the mass of swollen hydrogel at time *t*. When the equilibrium state is reached, the swollen hydrogel has the greatest swelling value.

Measurements

FT-IR analyzes were performed on a Perkin Elmer Spectrum 100 model FT-IR. The wave number range is 400-4000 cm^{-1}. ATR mode was used and each spectrum was scanned 4 times and worked at a resolution of 4 cm^{-1}. SEM analyzes were performed with Carl Zeiss Supra 40VP model SEM device. The surfaces are plated with Qourum brand coating device to ensure conductivity with platinum in the hydrogels. While the surfaces were being photographed, SE

(secondary detector) was used. Inorganic particle distributions in nanocomposite hydrogels were determined by applying the mapping method with the Bruker EDX detector. TGA analyzes were performed with the SETARAM simultaneous TG / DTA instrument. The heating was carried out at a temperature range of 25 °C-900 °C with a heating rate of 10 °C min^{-1} in N$_2$ atmosphere.

For better examination of the pore structures of the nanocomposite hydrogels, the water adsorbed hydrogels were put in a freezer (kept at -18 °C) for 12 h, then placed in a vacuum device with frozen states (instrument: Labconco, Freezone 2.5 (Canada) lyophilizer). Hydrogels that have been pressurized in the apparatus for 16 h were examined in FESEM without deformation by the water separation inside.

RESULTS AND DISCUSSION

Surface morphologies of original i.e. neutral nano-SiO$_2$ and amine-modified (hydrophilic, *hf*) nano-SiO$_2$ used in this study were shown in Fig. 2. As seen from these figures, while the surface of nano-SiO$_2$ is rough and irregular, the surface of amine-modified nano-SiO$_2$ is more regular and presents more uniform particle size distribution.
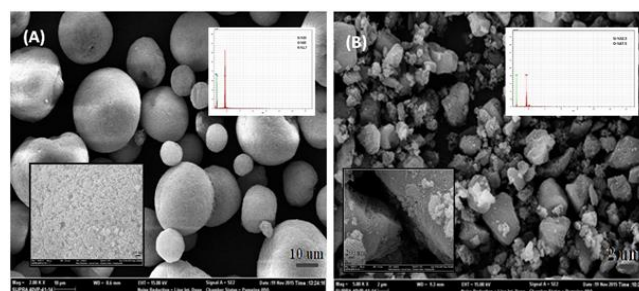
Figure 2. SEM photographs of (A) amine-modified nano-SiO$_2$ and (B) nano-SiO$_2$.

The results for gravimetric determination of nanocomposite hydrogels were given as table in the experimental section. From Table 1, it is apparent that nanocomposite hydrogels having amine-modified nano-SiO$_2$ showed more swelling than plain DMAPMAAm hydrogel and neutral nano-SiO$_2$ doped nanocomposite hydrogel. Structural changes observed for nanocomposite hydrogels were evaluated taking into account FT-IR results, shown in Fig. 3. The bands appearing on the spectrum are as follows: bands between 2650 cm^{-1} and 2950 cm^{-1} belong to CH$_2$ and CH groups of DMAPMAAm, respectively. The band for C = O groups of DMAPMAAm was seen at 1620 cm^{-1}.[15]
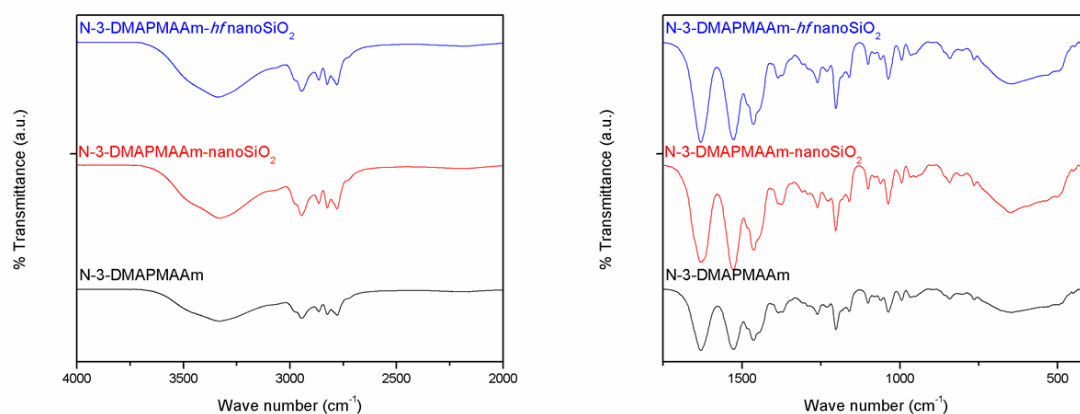
Figure 3. FT-IR spectra of DMAPMAAm, DMAPMAAm nano-SiO₂ and DMAPMAAm –hydrophilic (*hf*) nano-SiO₂.

The bands at 900-1550 cm⁻¹ indicate C-H bending in DMAPMAAm structure. Structural changes in nanocomposite hydrogels are much more difficult to understand then plain hydrogels because the nano-SiO₂ contribution is very small.
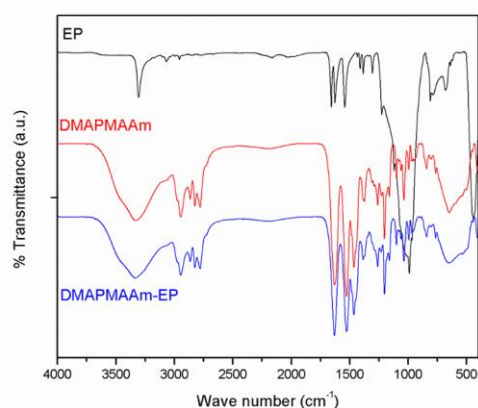
Figure 4. FT-IR spectra of DMAPMAAm, EP and DMAPMAAm EP.

Figure 4 shows the FT-IR spectrum of DMAPMAAm and EP doped DMAPMAAm nanocomposite hydrogel. In the spectrum, the H-bonding interactions between EP and the hydrogen in the Si-OH groups of nanocomposite hydrogel were also observed. The sharp band observed at 480 cm⁻¹ attributed to the Si-O-Si vibrations of EP was not observed in the nanocomposite spectrum because the amount of EP entering the DMAPMAAm was very low.

Surface morphologies of nanocomposite hydrogels were investigated by using SEM instrument by the aid of lyophilizer and mapping method. SEM photographs were taken by applying three methods. Following three Fig. s were about these evaluations. When classical SEM analysis of the nanocomposite hydrogels was performed, the cross-section was first taken as it is from the dried hydrogels and then the surface photographs were recorded. The SEM images given in Fig. 5 did not clarify the morphological structure of the nanocomposite, only showed how the nanoparticles influence the hydrogel structure.

Figure 5 shows the 500-magnified SEM images for DMAPMAAm hydrogels (A), with nano-SiO₂ added (B), amine-modified nano-SiO₂ added (C), and EP added (D) forms.
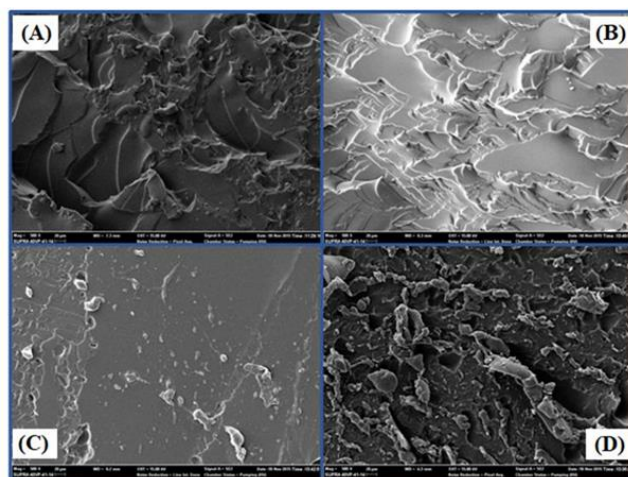
Figure 5. SEM images: (A) DMAPMAAm hydrogel; DMAPMAAm nanocomposite hydrogels having (B) nano-SiO₂, (C) (*hf*) nano-SiO₂, and (D) EP.
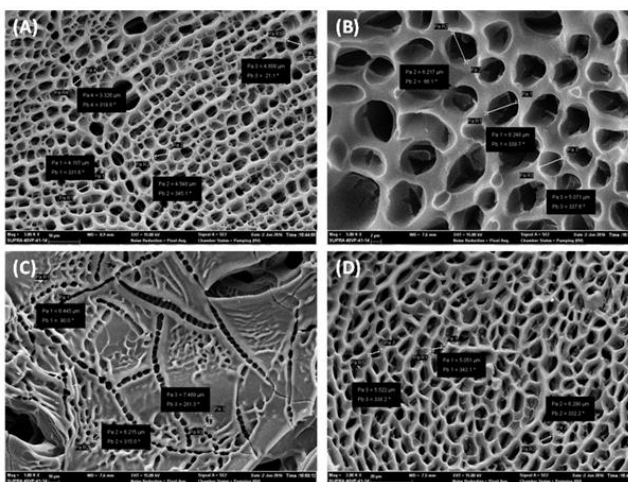
Figure 6. SEM images of lyophilized (A) DMAPMAAm hydrogel and (B) DMAPMAAm /nano-SiO₂, (C) DMAPMAAm /amine-modified hydrophilic nano-SiO₂, and (D) DMAPMAAm /EP nanocomposite hydrogels

While nano-SiO$_2$ doped DMAPMAAm nanocomposite hydrogels (B) have a rough structure, surface roughness of EP doped DMAPMAAm nanocomposite hydrogels (D) has increased. Amine-modified hydrophilic nano-SiO$_2$-added hydrogel (C) showed exact conformity to the original hydrogel structure caused a decrease in surface roughness

Figure 7. Mapped SEM images of (A) DMAPMAAm hydrogel and (B) DMAPMAAm/nano-SiO$_2$, (C) DMAPMAAm/amine-modified nano-SiO$_2$, (D) DMAPMAAm/EP nanocomposite hydrogels.

Second, the nanocomposite hydrogels were brought to swollen state and lyophilization were applied followed by taking SEM photographs. SEM photographs of lyophilized specimens showed pore and mesh structures. Finally, EDX spectra were taken to prove that the 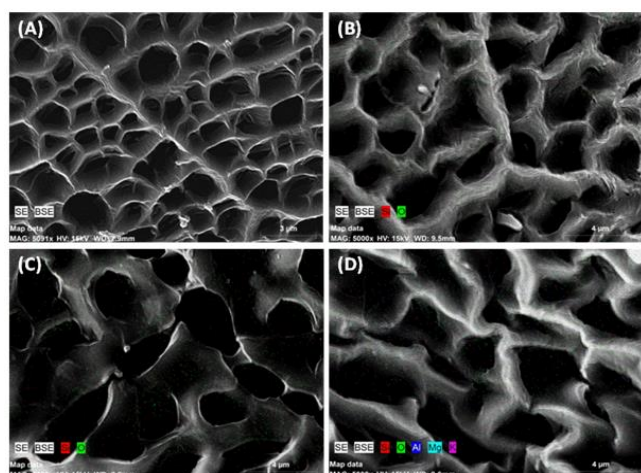hydrogels were doped with nano-SiO$_2$, amine-modified nano-SiO$_2$ and EP. In literature, the elemental maps of nanocomposites have been identified by EDX and distributions of doped nanoparticles has been proven.[16]

Fig. 6A shows the SEM image for lyophilized pure DMAPMAAm hydrogel; the average pore diameters were recorded as 4,147 μm. The pores have an uniform

distribution. In Fig. 6B, the diameters of pores in nano-SiO$_2$ doped DMAPMAAm nanocomposite hydrogel increased from 4.147 μm to 5.845 μm. The pore distribution is still homogenous. This image also shows the wall thickness of the nanocomposite increased after the addition of dopant nanoparticles. Fig. 6C shows the surface structure of DMAPMAAm nanocomposite hydrogel with amine-modified hydrophilic nano-SiO$_2$. The pores are arranged in a different manner. In Fig. 6D, the average pore diameter of the DMAPMAAm nanocomposite hydrogel with EP was 5.621 μm and homogeneous distribution was observed.

Fig. 7B shows a mapped SEM image giving elemental distribution of nano-SiO$_2$ doped DMAPMAAm. In the hydrogel structure, the elements are much more prominent in the pores than on the walls (It was shown Fig. 7C and D clearly). It is possible to see Si and O elements in the same frequency and homogeneously in the walls as the pores are filled with hydrophilic nano-SiO$_2$, because its surface compatibility is higher than the other additives (neutral SiO$_2$ and EP) in the mapping method. The element distribution of hydrophilic nano-SiO$_2$ doped DMAPMAAm hydrogels was clearly observed in Fig. 7C. In the mapping studies (Fig. 7D) made to indicate the element distribution of the EP-doped DMAPMAAm nanocomposite hydrogel, the distribution of Si, O, Al, Mg and K elements in the perlite was shown to be homogenous in the pores.

In addition to the structural and morphological characterization, the nanocomposite hydrogel has also been examined for thermal stability. In a TGA curve, which is a study of the formation of copolymers on polypropylene films with DMAPMAAm, 50% parts of DMAPMAAm is reported to degrade at 406 °C.[17] In Fig. 8 (B), the maximum decomposition temperature of DMAPMAAm hydrogel is 419 °C. And weight loss was calculated ~ %80. From the doped composites it has been found that the amine-modified nano-SiO$_2$, which has been proven to be fully compatible with the structure, has a maximum breakdown temperature of 421 °C. Thermal decomposition of nanocomposite hydrogels has been start at 200 °C and has completed at 470 °C.
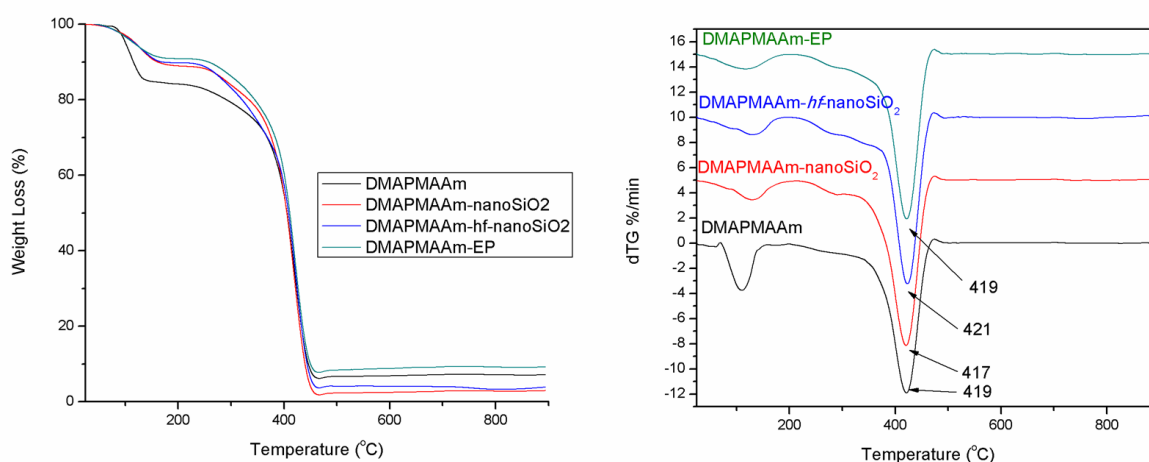
Figure 8. (A) TGA and (B) DTG curves of DMAPMAAm hydrogel and DMAPMAAm nanocomposite hydrogels.

CONCLUSION

The experimental conditions for all nanocomposite hydrogels were determined in the same way during the synthesis of the study. After the behavior of nano-SiO$_2$ in hydrogels was determined, the volcanic rock type Perlite, which is common in nature and cheaper than the commercial cost of nano-SiO$_2$, is doped to DMAPMAAm hydrogels. The perlite design of the polymer / clay nanocomposite is due to the fact that its high SiO$_2$ content (~75%). This allowed us to be informed about the behavior of SiO$_2$ in perlite from the results obtained by observing the pure nano-SiO$_2$ behavior of the nanocomposite hydrogel structure. Structural and morphological characterization were performed by FT-IR, and detailed SEM analyses. The results showed that the amine-modified nano-SiO$_2$ was in complete conformity with the DMAPMAAm hydrogels, resulting in improved swelling, mechanical, morphological and thermal properties.

The behaviour of three different SiO$_2$ reinforcements in composite hydrogels during the planning of target-focused work with SiO$_2$ doped nanocomposite hydrogels is important in interpreting the results to be achieved in the target applications.

ACKNOWLEDGMENT

REFERENCES

[1]Bouwstra, J. A., Jungiger, H. E., In: Swarbrick, J. and Boylan, J. C., Eds., *Encyclopedia of Pharmaceutical Technology,* 1st Edition, Vol. 7, Marcel Dekker Inc, New York, **1993**.

[2]Gaharwar, A. K., Peppas, N. A., Khademhosseini, A., *Biotechnol. Bioeng.*, **2014**, *111*, 441-453. DOI: 10.1002/bit.25160

[3]Paul, D. R., Robeson, L. M.*, Polymer*, **2008**, *49*, 3187-3204. https://doi.org/10.1016/j.polymer.2008.04.017

[4]Shetye, S. P., Godbole, A., Bhilegaokar, S., Gajare, P., *IJSRM. Human,* **2015**, *1(1)* , 47-71.

[5]Satish, C. S., Satish, K. P. and Shivakumar, H. G., *Indian J. Pharm. Sci.,* **2006**, *68 (2)*, 133-140. DOI: 10.4103/0250-474X.25706

[6]Blanco, M. D., Garcia, O., Trigo, R. M., Teijon, J. M. and Katime, I., *Biomaterials*, **1996**, *17 (11)*, 1061-1067. https://doi.org/10.1016/0142-9612(96)85906-0

[7]Ahmed, E. M., *J. Adv. Res.*, **2015**, *6 (2)*, 105-121. https://doi.org/10.1016/j.jare.2013.07.006

[8]Hamidi, M., Azadi, A., Rafiei, P., *Adv. Drug Del. Rev.*, **2009**, *60 (15)*, 1638–1649. https://doi.org/10.1016/j.addr.2008.08.002

[9]Peppas, N. A. and Khare, A. R., *Adv. Drug Del. Rev.*, **1993**, *11 (1-2)*, 1. https://doi.org/10.1016/0169-409X(93)90025-Y

[10]Anisha, S., Kumar, S. P., Kumar, G. V., Garima, G., *Int. J. Pharm. Sci. Rev. Res.*, **2010**, *4 (2)*,102.

[11]Sun, X., Zhang, G., Shi, Q., Tang, B., Wu, Z. J., *J. Appl. Polym. Sci.*, **2002**, *86*, 3212–3717.

[12]Kashyap, N., Kumar, N., Kumar, M., *Critical Crit. Rev. Ther. Drug*, **2005**, *22(2)*, 107–149. DOI: 10.1615/CritRevTherDrugCarrierSyst.v22.i2.10

[13]Ulusoy, U., Şimşek, S., *J. Hazard. Mater.*, **2005**, *127 (1)*, 163–171. https://doi.org/10.1016/j.jhazmat.2005.06.036

[14]Malhotra, S. L., Parikh, K. K., Blumstein, A., *J. Colloid Interf. Sci.,* **1972**, *41 (2)*, 318-327. https://doi.org/10.1016/0021-9797(72)90117-8

[15]Chen, J., Yang, L., Nho, Y. C., Hoffman, S., *Topics in Tissue Engineering*, *4*, Chapter 14, **2008.** [16]Ganeshraja, A. S., Clara, A. S., Rajkumar, K., Wang, Y., Wang, J., Anbalagan, K., *Appl. Surf. Sci.*, **2015,** *353*, 553-563. https://doi.org/10.1016/j.apsusc.2015.06.118

[17]Contreras-Garcia, A., Alvarez-Lorenzo, C., Concheiro, A., Bucio, E., *Radiat. Phys. Chem.,* **2010,** *79 (5)*, 615-621. https://doi.org/10.1016/j.radphyschem.2009.12.007

SOLVENTS EFFECT ON THERMAL STABILITY AND ELECTROCHEMICAL BEHAVIOUR OF *GRIFFONIA SIMPLI-CIFOLIA* EXTRACTS AS STEEL CORROSION INHIBITOR IN ACIDIC ENVIRONMENT

Ekemini Ituen,[a],[b]* Onyewuchi Akaranta[b],[c] and Abosede James[c]

Different solvents were used to extract *Griffonia simplicifolia* and tested corrosion inhibitors for as X80 steel in 1 M HCl solution. The corrosion tests were conducted by thermo-gravimetric analyses (TGA), electrochemical impedance spectroscopy (EIS) and potentiodynamic polarization (PDP) while the surface morphologies were checked by scanning electron microscopy (SEM). The essence was to investigate the effects of the solvents on the yield, phytochemical profile, corrosion inhibition properties and thermal stability of the extracts. The highest yields of 63.24 g kg^{-1} and 51.63 g kg^{-1} were obtained with seeds (SEGS) and leaves (LEGS) extracts respectively in ethanol-water (1:1) system. Acetone extract showed presence of all the tested phytochemicals namely alkaloids, tannins, saponins, glycosides, steroids and terpenoids. The highest inhibition efficiencies of 95.86 % (SEGS) and 82.14 % (LEGS) were obtained with acetone extracts. Acetone extract was also most thermally stable being 66.4 % (SEGS) and 50.05 % (LEGS) efficient at 90 °C, followed by ethanol extract while methanol extract was least stable and least efficient. Inhibitors act as mixed type and their addition increased charge transfer resistance and decreased corrosion current density with respect to the free acid solution. Micrographs of the steel surface in some systems show evidence of slight surface protection by the inhibitors. It has been inferred from this study that both acetone and ethanol are better solvents for extraction of *Griffonia simplicifolia* based corrosion inhibitors.

* Corresponding Author's
    E-Mail: ebituen@gmail.com
[a]   Materials and Oilfield Chemistry (MOC) Research Group, Department of Chemistry, University of Uyo, Nigeria
[b]   African Centre of Excellence in Oilfield Chemicals Research, Institute of Petroleum Studies, University of Port Harcourt, Nigeria.
[c]   Department of Pure and Industrial Chemistry, University of Port Harcourt, Nigeria.

Introduction

Corrosion of metals and alloys in various aggressive media has been an active area of research. In the oil and gas industry where corrosion is associated with various operations such as pickling, well acidizing and fracture, corrosion inhibitors are usually deployed to reduce the rate of corrosion. Several chemicals and organic compounds have been reported to be capable of inhibiting corrosion in various oilfield environments.[1] Many of these compounds are toxic and very expensive. Environmental and economic concerns have triggered preference for green corrosion inhibitors derived from sustainable and cheap sources. A vast number of plant extracts have been investigated and some of them have shown excellent inhibitive effects especially at low temperatures.[2-4]

If plants that are meant for food are used to produce corrosion inhibitors, food scarcity may set in. Therefore, inedible plants and agricultural wastes are better options. Previously, we have reported the efficiency of extracts of seeds (SEGS) and leaves (LEGS) of *Griffonia simlicifolia* as corrosion inhibitor for different oilfield grades of steel in various simulated acidizing and fracture fluids.[5,6] Detailed information on *Griffonia simplicifolia* were also given in the articles cited while others are available in literature,[7] the picture is shown in figure 1. In these reports, both LEGS and

SEGS were extracted in acetone. The acetone extracts were efficient at low temperatures but performed poorly at high temperatures perhaps due to thermal degradation. This made it difficult to commercialize the product of that research. It was also difficult to predict if the potency of the extracts could change if they were extracted in other solvents. This study was therefore designed to investigate the effects of solvents on the inhibitive efficiency of SEGS and LEGS in acidizing environment.

Figure 1. Leaves and seeds of *Grifonia simplicifolia*.

In this study, the plant parts were extracted in different solvents and the phytochemical profile of each solvent fraction was screened. The extracts were subjected to corrosion tests using X80 steel with 1 M HCl being the corroding medium. Standard techniques such as TGA, EIS and PDP were used for the corrosion tests. SEM was also used to probe the surface of the steel in the absence and presence of the inhibitors. The effects of the different solvents on the corrosion inhibitive potential of the extracts were evaluated. The choice of X80 steel was motivated by its widespread application in construction of casings, tubing, pipe works and transport lines in the oil and gas industry.[8-14] On the other hand, the choice of *Griffonia simplicifolia* is due to the broad alkaloid composition which has been reported about the plant, especially the presence of 5-hydroxytryptophan.[15]

Experimental

Steel samples and surface preparation

X80 steel samples were purchased from Qingdao Tengxiang Instrument and Equipment Co. Ltd., China and were cut into coupons of dimension 2 cm x 2 cm for thermo-gravimetric experiments and 1 cm x 1 cm for electrochemical studies. The surface of each coupon was treated as provided by NACE Recommended Practice RP-0775 and ASTM G-1 & G-4 for surface finishing and cleaning of weight-loss coupons. The coupons for electrochemical studies were abraded using different grades of silicon carbide paper and finished to mirror surface with CC-22F P1000. The prepared specimens were put in sealed water-proof containers and stored in moisture free desiccator prior to use. The chemical composition of the X80 steel was C (0.065), Si (0.24), Mn (1.58), P (0.011), S (0.003), Cu (0.01), Cr (0.022), Nb (0.057), V (0.005), Ti (0.024), B (0.0006), and Fe (balance).

Preparation of plant extracts

Mature seeds and leaves of *Griffonia simplicifolia* were harvested from a local bush in Ikot Ambon Ibesikpo, Uyo, Nigeria. The seed pericarps were removed and the seeds were washed and air-dried in the laboratory for one week, ground to powder and soaked in the different solvents for 48 h, then retrieved and filtered. The filtrate was concentrated using rotary evaporator at room temperature. The washed leaves were air-dried in the absence of light for one week, ground and extracted as described above.

Phytochemical screening

The extract was screened for the presence of alkaloids, tannins, terpenoids, glycosides, flavonoids, saponins, and steroids using standard procedures reported in literature.[15]

Preparation of extract for corrosion study

The dry extracts were accurately weighed and prepared in 1 M HCl (analytical grade) to concentration of 1000 ppm

with distilled water and labelled SEGS (seed extract) and LEGS (leave extract).

Control experimental sample

A commercially corrosion inhibitor for acidizing was purchased and also tested under the same conditions. It was a reddish brown liquid with pH around 3-5. About 5ml of the liquid was dissolved in 995 ml 1 M HCl and well shaken before use in the corrosion experiment. This sample was labeled CTR-INH.

Thermogravimetric analysis (TGA)

Pre-weighed steel coupons were immersed in the test solutions in the absence and presence of the studied inhibitors for 5 h at 30 °C in a water bath. They were retrieved, cleaned using standard procedures[16] and weighed to determine the weight loss. Experiments were carried out in triplicates and the mean values of the weight losses were used for computation. By denoting the initial and final weights of the coupons as w_1 and w_2 respectively, corrosion rate of iron, percentage inhibitor effectiveness (inhibition efficiency ε_{WL}, and degree of surface coverage (θ), were calculated as follows:

$$CR = \frac{87.6(w_1 - w_2)}{\rho At} \qquad (1)$$

$$\varepsilon_{WL} = 100(\frac{CR_b - CR_i}{CR_b}) \qquad (2)$$

$$\theta = 0.01\varepsilon_{inh} \qquad (3)$$

where

CR_b and CR_i are the corrosion rates (mmpy) in the absence and presence of the inhibitor, ρ is the density of iron, A is the average surface area (cm^2) of the metal specimens and t is the immersion time. This procedure was repeated at 60 °C and 90 °C. Also, the procedure was followed using CTR-INH at the different temperatures.

Electrochemical measurements

The corrosion process was monitored using Gamry ZRA REF 600-18042 electrochemical workstation. The conventional three electrode set up was used consisting of saturated calomel electrode (SCE) as reference electrode, platinum as counter electrode and the different steel coupons as working electrode. EIS measurements were conducted at frequency of 10^5 to 10^{-2} Hz for immersion time of 30 min at 30 °C. The voltage was changed to -0.15 V to +0.15 V vs. E_{OC} at scan rate of 1 mV/s for PDP measurements. E-Chem software package was used for data fitting and analyses. Electrochemical studies were conducted for only SEGS.

Charge transfer resistance from EIS measurements were used to compute the inhibition efficiency according to Eqn.

(4) while the inhibition efficiencies from PDP was calculated from the corrosion current densities using Eqn. (5).

$$\varepsilon_{EIS} = 100 \left(\frac{R_{ctI} - R_{ctB}}{R_{ctI}} \right) \qquad (4)$$

where

R_{CtB} and R_{ctI} are charge transfer resistances in the absence and presence of inhibitor respectively.

$$\varepsilon_{PD} = 100(1 - \frac{I^{i}_{corr}}{I^{b}_{corr}}) \qquad (5)$$

where

I^{b}_{corr} and I^{i}_{corr} are the corrosion current densities in the absence and presence of the inhibitor respectively. The magnitude of the double layer capacitance (C_{dl}) of the adsorbed film was calculated from constant phase element (CPE) constant (Y_0) and charge transfer resistance (R_{ct})) using eqn (6).

$$C_{dl} = \left(Y_0 R_{ct}^{n1} \right)^{1/n} \qquad (6)$$

where n is a constant showing degree of roughness of the metal surface obtained from the phase angle given that ($j^2=-1)\alpha$ and $n=2\alpha/\pi$ and is the CPE exponent. EIS and PDP measurements were also conducted using CTR-INH at 30 °C.

SEM studies

X80 steel coupons of dimensions 1 cm × 2 cm were abraded to mirror finish as earlier described. The morphologies of the surfaces immersed in 1 M HCl and those of acetone and ethanol SEGS for 12 h were scanned by SEM.

RESULTS AND DISCUSSION

Yield of extract

The yield of the crude extract obtained by direct extraction of 1.0 kg of the ground leaves and seeds of *Griffonia simplicifolia* at room temperature is given in Table 1. The highest yield of 63.24 g/1000 g and 51.63 g/1000 g was obtained with 1:1 (v/v) water-ethanol solvent mixer for SEGS and LEGS respectively. As can be observed in table 1, the seeds yield higher than the leaves, and the yield follows the trend ethanol-water > acetone > water > ethanol > methanol.

Table 1. Yield of LEGS and SEGS in different solvents at room temperature.

Solvent	Yield (g kg^{-1} dry weight)	
	LEGS	**SEGS**
Acetone	43.23	58.16
Methanol	16.72	20.45
Ethanol	48.18	52.86
Water	44.73	57.45
Ethanol-Water (50-50)	51.63	63.24

Phytochemical profile of extract

Phytochemical screening of the extracts from the different solvents reveals that acetone extracts of LEGS and SEGS contained all the groups of compounds tested namely alkaloids, tannins, saponins, glycosides and terpenoids. These substances are rich in functionalities containing lone pair of electrons and π-electrons which are potential adsorption sites of established corrosion inhibitors.[1] Table 2 shows the phytochemical profile of LEGS and SEGS in the different solvents studied. Alkaloids are detected in extracts of all the solvents studied while flavonoids were not detected in any. These result are in partial agreement with those reported for seeds of *Griffonia simplicifolia* in Ghana.[17]

TGA studies

In other to determine which solvent would provide the highest inhibition efficiency, LEGS and SEGS were extracted using methanol (MeOH), ethanol (EtOH), acetone, water and ethanol-water (1:1) (EtOH-H$_2$O) as solvents. Results (Table 3) show that acetone extract gave the highest inhibition efficiency which also sustained appreciably at high temperature. It was earlier observed that acetone extract contained all the phytochemicals tested, which may be responsible for the high inhibition efficiency obtained.

EIS studies

EIS measurements for corrosion of X80 in 1 M HCl were carried out in the absence and presence the SEGS as well as CTR-INH. Nyquist plots shown in Fig. 2 were constructed using the experimental data obtained. The plots yielded imperfect semicircles with diameters influenced in the presence of SEGS from that of HCl solution. The differences in sizes of the diameters of the curves obtained can be due to the influence of the different solvents on the efficiency of SEGS. It can be observed that all the curves are larger in diameter in the inhibited solutions than the free acid solution which may be due to corrosion inhibition.

The diameters increase according to the trend CTR-INH > ETOH > ETOH-H$_2$O > Acetone > H$_2$O > MeOH > HCl which is similar to the trend of inhibition efficiency obtained from TGA. This indicates that TGA and EIS are in agreement. A close look at table 2 also reveals that the inhibition efficiencies obtained from both measurements are comparable.

Table 2. Phytochemical profile of SEGS and LEGS in different solvents.

Solvent	Alkaloids		Tannins		Saponins		Glycosides		Steroids		Terpenoids	
	LEGS	SEGS	LEGS	SEGS	LEGS	SEGS	LEGS	SEGS	LEGS	SEGS	LEGS	SEGS
Acetone	+	+	+	+	+	+	+	+	+	+	+	+
Methanol	+	+	-	+	-	-	+	-	+	+	+	-
Ethanol	+	+	-	+	+	-	+	+	+	+	+	-
Water	+	+	+	+	+	+	+	+	-	-	+	+
EtOH-H$_2$O	+	+	+	+	+	+	+	+	-	+	+	-

Table 3. Effect of solvent on the inhibition efficiency of LEGS and SEGS using weight loss measurement.

T, °C	EtOH-H$_2$O		MeOH		EtOH		H$_2$O		Acetone		CNTR-INH
	SEGS	LEGS	SEGS	LEGS	SEGS	LEGS	SEGS	LEGS	SEGS	LEGS	
30	91.73	79.68	84.63	56.08	91.02	78.43	90.31	76.17	95.86	82.14	100.0
60	78.41	65.18	62.54	42.17	78.91	67.02	73.02	61.13	82.64	69.42	99.8
90	56.25	41.45	42.49	36.34	57.14	42.85	50.42	39.12	66.04	50.15	94.2

Imperfections in the shapes of the semicircles can be attributed to roughness or heterogeneity of the steel surface.[18] The shapes of the plots were similar in both inhibited and free acid solution indicating that the mechanism of steel corrosion is not influenced by SEGS. However, slight differences can be observed in ethanol-water mixture and acetone. This implies that in addition to charge transfer mechanism, SEGS adsorption in these two solvents may also be associated with diffusion mechanism For uniformity, the same equivalent circuit in Figure 3 corresponding to $R_s(R_{ct}Ø_{CPE})$ model was used to analyze the obtained data. Goodness of the fits obtained was in the order of 10^{-4} indicating good correlation with the model. The surface roughness or heterogeneity of the steel was compensated by introduction of a non-integer element dependent on frequency called constant phase element, CPE, estimated in terms of Y_0 and n, related to impedance by Eqn. (7).

$$Z_{CPE} = (Y_0)^{-1} (j\omega)^{-n} \qquad (7)$$

where

Z_{CPE} is the impedance of the CPE,

Y_0 is the CPE constant,

ω is the angular frequency,

j is an imaginary complex number, (j^2=-1)α is the phase angle of CPE and $n=2\alpha/\pi$,

Table 4. Some EIS parameters determined for the inhibition of X80 steel corrosion in 1 M HCl without and with SEGS extracted from different solvents.

Test solution	R_{CT} Ω cm^2	R_S Ω cm^2	n	C_{dl} μF cm^{-2}	ε_{EIS}, %
1 M HCl	68.9	0.982	0.736	15.4	-
MeOH	429.8	1.225	0.724	11.4	83.9
H$_2$O	630.1	1.122	0.805	8.6	89.0
Acetone	825.1	1.410	0.786	5.8	91.6
EtOH-H$_2$O	767.0	1.136	0.811	9.2	91.0
EtOH	837.6	1.213	0.816	4.7	91.7
CTR-INH	1089.1	1.679	0.776	2.6	93.6

Some of the EIS parameters calculated are presented in Table 4. The value of n can be used to predict the degree of roughness or inhomogeneity of the steel surface. This value decreases on addition of SEGS suggesting that the surface roughness of the steel is increased by adsorption of inhibitor molecules.[20] It also shows that there is relative and/or integrated influence on the CPE and not just a single resistance, capacitance or inductive element. Decrease in n on addition inhibitors also signifies insulation of the metal/solution interface by formation of a surface film, which results in increase in charge transfer resistance in the presence than in the absence of inhibitor. The charge transfer resistance increases according to the trend of inhibition efficiency showing that the 'insulating' property of the film improved as solvent elicits better cooperative or synergistic effect with the extract.

The C_{dl} values obtained decreases in the presence of inhibitors similar to results reported in literature.[18] This has been attributed to decrease in the local dielectric or increase in the thickness of the double layer or both, caused by the adsorbed protective film of the inhibitors.[18]
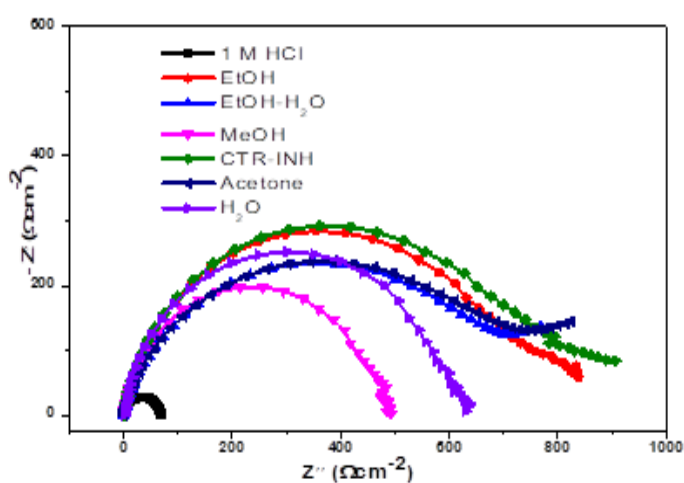
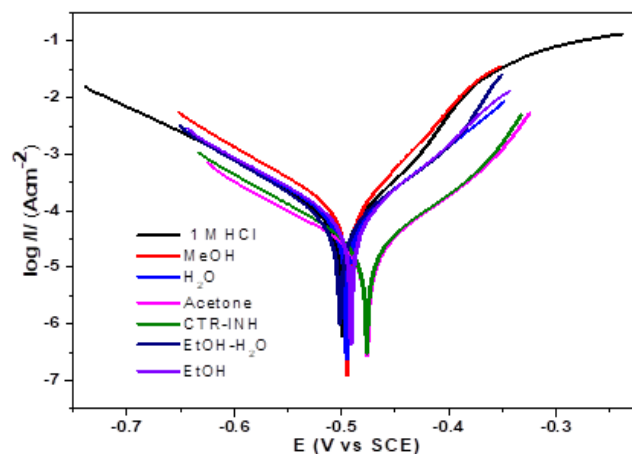**Figure 2.** Nyquist plot for the inhibition of X80 steel corrosion in 1 M HCl using SEGS in different solvents.

PDP study

Polarization (Tafel) curves for X80 steel corrosion in 1 M HCl in the absence and presence of SEGS from different solvents obtained at 30 °C is shown in figure 3. The corrosion potential (E_{corr}) and the corresponding corrosion current density (I_{corr}), Tafel anodic slope constant (β_a), Tafel cathodic slope constants (β_c) and inhibition efficiency (ε_{PD}) deduced from the plots are listed in Table 5. The E_{corr} values obtained in the presence of SEGS are more positive than that of the free acid solution indicating that SEG has influenced the corrosion rate of the steel. E_{corr} values shift to more positive regions on addition of SEGS from all the solvents signifying that the SEGS has more effects on anodic half reaction by suppressing the oxidation or corrosion of iron.[21] In the literature, when the shift in E_{corr} values is up to -85 mV, the inhibitor is classified as anodic or cathodic type inhibitor.[22] The shifts in E_{corr} values obtained is not up to -85 mV indicating that SEGS acts as a mixed type inhibitor with anodic predominance.[22]

SEM analyses

The surfaces of the coupons in 1 M HCl and those in acetone and ethanol SEGS were scanned by SEM. Results (Figure 4) show that roughness of the micrographs of the steel surface were more highly attacked in the uninhibited acid solution compared to the inhibited solutions. This demonstrates that the extracts inhibit X80 steel corrosion. Though the adsorbed film is not very visible, it can be seen inferred that corrosion inhibition is due to adsorption of the extracts on the steel surface.

Figure 3. Tafel plots for the inhibition of X80 steel corrosion in 1 M HCl using SEGS in different solvents.

Table 5. Some PDP parameters determined for the inhibition of X80 steel corrosion in 1 M HCl without and with SEGS extracted from different solvents.

Test Solution	E_{corr}, mV vs SCE	I_{corr}, µA cm^{-2}	β_a, mV dec^{-1}	β_c, mV dec^{-1}	ε_{PD}, %
1 M HCl	-499	693.1	82.5	98.4	−
MeOH	-492	119.2	103.7	110.6	82.8
H$_2$O	-481	74.8	99.4	108.5	89.2
Acetone	-464	56.8	101.7	131.2	91.8
EtOH-H$_2$O	-494	63.1	98.5	102.4	90.9
EtOH	-483	53.4	112.1	109.7	92.3
CTR-INH	-463	41.6	107.9	99.8	84.0
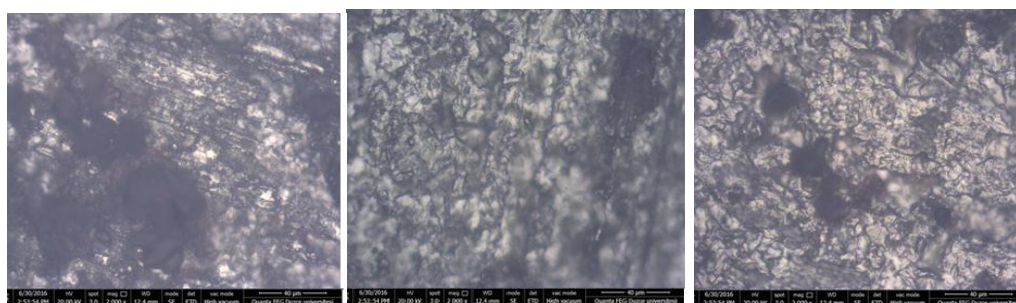
Figure 4. SEM micrographs of X80 steel immersed in 1 M HCl (left), Acetone SEGS (middle) and EtOH SEGS (right).

Conclusion

Effects of solvents on the yield, phytochemical profile, corrosion inhibition properties and thermal stability of the *Griffonia simplicifolia* extracts have been investigated. Based on the results, the following conclusions are drawn: Acetone produces the highest yield while methanol produces the lowest yield of the extracts per 1000 g of solvent. Acetone extract contains alkaloids, tannins, saponins, glycosides, steroids and terpenoids. Acetone extract is most efficient in the inhibition of X80 steel corrosion in 1 M HCl while methanol extracts is the least efficient. Acetone and ethanol extracts are more thermally stable at 90 °C while methanol is least thermally stable at that temperature. Extracts of in the solvents act as mixed type inhibitors.

References

[1]Finšgar, M, Jackson, J., *Corros. Sci.*, **2014,** *86*, 17. https://doi.org/10.1016/j.corsci.2014.04.044

[2]Sangeetha M, Rajendran S, Muthumegala T.S, Krishnaveni A., *Mater. Prot.*, **2011,** *52*, 3.

[3]Raja, P.B. and Sethuraman, M.G., *Mater. Lett.*, **2008**, 62, 113. https://doi.org/10.1016/j.matlet.2007.04.079

[4]Rani, B. and Basu, B. B. J., *Int. J. Corros*., **2012**, Article ID 380217, 15 pages. http://dx.doi.org/10.1155/2012/380217

[5]Ituen, E., Akaranta, O., James, A., Sun, S., *Sustain. Mater. Technol.*, **2017**, *11*, 12

[6]Ituen, E. B, Akaranta, O., James, A. O, Sun, S., *J. Chem. Mater. Res*., **2016**, 5, 45.

[7]Kumar, P. S., Praven, T., Jain, N. P., Jitendra, B., *Int. J. Pharm. Life Sci.*, **2010**. *1*, 174.

[8]Craig, B. D., *SPE Reprint Series*, **1997**, 143.

[9]Kennedy, J. L., *Oil and gas pipeline fundamentals,* Pennwell Books, Tulsa, Oklahoma, **1993**

[10]Crolet, J. L., *J. Petrol. Technol*. **1983**, *35*, 1553. https://doi.org/10.2118/10045-PA

[11]Heidersbach, R., *Metallurgy and corrosion control in oil and gas production*, John Wiley & Sons, **2010,** Hoboken, New Jersey.

[12]Siciliano, F., Stalheim, D. G., Gray, J. M., *Modern high strength steels for oil and gas transmission pipelines*, 7th International Pipeline Conference, American Society of Mechanical Engineers, Alberta, **2008**. https://doi.org/10.1115/IPC2008-64292

[13]Ueda, M., Takabe, H., Nice, P. I., *The development and implementation of a new alloyed steel for oil and gas production wells*, CORROSION 2000 NACE International, **2000,** Orlando, Florida.

[14]Smith, L., *Brit. Corr. J.*, **1999**. *34*, 2471. https://doi.org/10.1179/000705999101500905

[15]Ituen, E. B. and Udo, U. E., *Der Chemica Sinica*, **2012,** *3*, 1394.

[16]Ahmad, Z., *Principles of Corrosion Engineering and Corrosion Control*, Butterworth-Heinemann, **2006,** Boston.

[17]Addotey, A., *Local production of 5-HTP from the seeds of Griffonia simplicifolia*, Doctoral dissertation, Kwame Nkrumah University of Science and Technology, Kumasi, Ghana, **2010**.

[18]Singh, P., Singh, A., Quraishi, M., *J. Taiwan Inst. Chem. Eng.*, **2015,** *60*, 588.

[19]Artamonova, I. V., Gorichev, I. G., Godunov, E. B., *Chem. Petrol. Eng.*, **2017,** *52*, 710. https://doi.org/10.1007/s10556-017-0257-2

[20]Anupama, K. K., Ramya, K., Shainy, K. M., Joseph, A., *Mater. Chem. Phys.*, **2015**, 167, 28. https://doi.org/10.1016/j.matchemphys.2015.09.013

[21]Ehsani, A., Mahjani, M. G., Hosseini, M., Safari, R., Moshrefi, R., Mohammad S. H., *J. Colloid Interface Sci.*, **2017,** *490*, 444. https://doi.org/10.1016/j.jcis.2016.11.048

[22]Singh, A., Ansari, K. R., Kumar, A., Liu, W., Songsong, C., Lin, Y., *J. Alloys Comp.*, **2017**, *712,* 121.

LAND-COVER CLASSIFICATION FOR EAST SUEZ CANAL REGION USING HYPERSPECTRAL EO-1 DATA

Nagwan M. Afify,[a]*Abdel Aziz S. Sheta,[b] Sayed M. Arafat,[a] Afify A. Afify,[c] Mohammed S. Abd-Elwahed2[b] and Adel S. El-Beltagy[b]

Earth Observation (EO-1) data provides a highest spectral resolution to get spectral information of Earth's Surface targets within 242 spectral bands at 30 m spatial resolution. In this context, the main objective of this paper is to produce a land cover map using hyperspectral data acquired by EO-1 Hyperion instrument over one test site. Atmospheric correction on the hyperspectral data was performed using ENVI's Fast Line-of-sight Atmospheric Analysis of Spectral Hyper-cubes (FLAASH) module. Support Vector Machine (SVM) classification was implemented on the dominant elements to produce a land cover map for test site. SVM is carried out in this research to deal with the multi-class issue of Hyperion data. Classification using the kernel functions in classification made the classifier robust against the outliers. The Land Cover Classification System (LCCS) was used to know the land cover classes. The result showed high accuracy for land cover map with machine learning classifier like SVM using hyperspectral remote sensing data. The overall classification accuracy obtained was 97.85.

---

* Corresponding Authors
        Fax: +20 2 6225800
        Email: nagwanafify6@gmail.com
[a]   Authority for Remote Sensing and Space Sciences
[b]   Soil Science Department, Faculty of Agriculture, Ain - Shames University, Egypt
[c]   Soil Water and Environment Research Institute, Agricultural Research Centre

INTRODUCTION

Land cover (LC) is very important in a lot of natural resource applications. At local and regional scale, knowledge of LC forms a basic dimension of recourses available to any political unit.[1] On a wide scale, LC information is of main importance in determining the broad patterns of climate and vegetation which form the environmental framework for human activities. Furthermore, LC maps are also a valuable contribution in the development of maintain policies particularly for ecologically protected areas and the restoration of native environments, as well as the monitoring of desertification and land degradation in regions.[2] Remote sensing has been appropriate source for LC thematic mapping.[3] Accordingly image classification[4] is the most widely used for this purpose it is the most frequently applied approach in developing land use and land cover spatial distribution maps.[5] An overview of different remote sensing classification techniques has been published.[6]

Recently, progresses in sensor technologies have directed to the launch of hyperspectral remote sensing systems. Hyperspectral sensors are able to register reflected light from land surface elements in many narrow continuous spectral bands from the visible to the shortwave infrared parts of the electromagnetic spectrum.[7] this allows hyperspectral systems to provide spectral information useful for many applications but not limited to land cover maps.[8]

The launch of the Hyperion space-borne hyperspectral sensor in 2000 under NASA's New Millennium Program on-board the Earth Observer-1 (EO-1) satellite platform.[9] Hyperion acquiring spectral information of Earth's surface objects in 242 spectral bands and at a spatial resolution of 30 m. The Hyperion sensor has two spectrometers one in the visible and near-infrared (VNIR) (bands 8–57, region 427–925 nm) and one in the shortwave infrared (SWIR) region (bands 77–224, region 912–2395 nm). The swath width of Hyperion is 7.6 km across-track, and approximately 53.6 or 80.4 km along-track.

The potential of Hyperion imagery for land cover mapping has been verified by many investigators.[10] In this context, the main objective of this study is to produce a land cover map for east Suez Canal region using hyperspectral data acquired by the EO-1 Hyperion instrument with the Support Vector Machine (SVM) classification techniques. Another goal is to use Land Cover Classification System (LCCS) to define the land cover classes.

Site selection and data source

The study area was located in El Qantra-sharq District of Ismailia Governorate east of Suez Canal covers almost 34165 feddans. It represents the new reclaimed land for the agriculture land use. The coordinates of the upper left corner are 30°38′ 20″ N and 32°23′ 20″ E, while the lower right corner coordinates are 30°30′ 0″ N and 32°28′ 20″ E (Figure 1). According to Ismailia weather station (624400), it is the nearest recording station to the study area. The climate of the study area is aridic regime, which is characterized by a short winter season and a long hot summer. The temperature sometimes varied widely through different periods of the year, as the minimum mean was 8.4 °C in January, while the maximum mean was 35.6 °C during July. The normal values of the monthly rainfall show that the average of annual rainfall was approximately 25 mm / year. The relative humidity is higher in winter than in summer, it attains a minimum average of 52.2% in May and a maximum average of 66.5% in August. The relief of the area is variable, with the average altitude varying from 0 to

200 m above sea level. Geologically, the area is belong to Quaternary deposits were divided into Holocene and Pleistocene. The vegetation cover is limited to citrus tree, clover and hordeum.

The Hyperion imagery of site selection was acquired on January 9, 2016. The imagery was received from NASA Earth Observer (EO)-1 Hyperion sensor, record as a full long scene (185-km strip) and at level 1 (L1GST) processing. This processing level product is a geo-tiff image format, and is already radiometric corrected, geometrically resampled, and registered to a geographic map projection with elevation correction applied.[9]
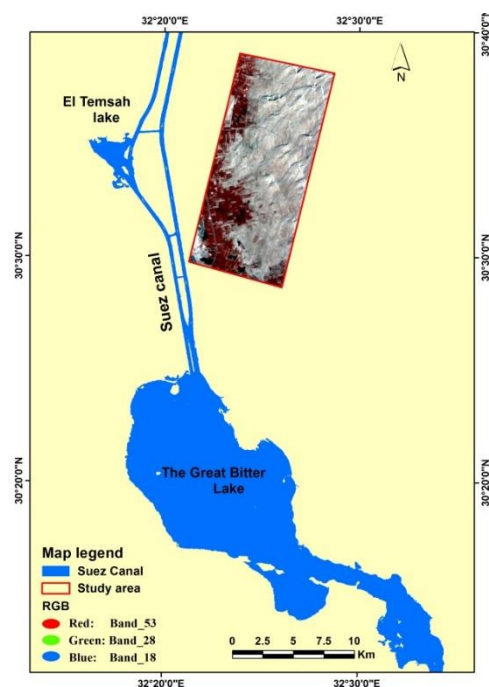
Figure 1. Location of the study area

METHODS

Summary of the methodology adopted in the study is explained in (Figure 2) and the image processing details are given in the following sections.

Linear interpolation of sensor

All pre-processing of the Hyperion imagery was carried out using ENVI (5.1). The first step in the pre-processing involved the linear interpolation of all the sensor detectors on a pixel by pixel, spectrum by spectrum, and band by band basis to a common set of wavelengths, which resulted 242-band image.

Remove bad band

The Hyperion visible and near-infrared (VNIR) spectrometer has only 50 calibrated bands, while the short-wave infrared (SWIR) spectrometer has only 148 calibrated bands. The non-calibrated bands of the Hyperion imagery (1–7, 58–76, and 225–242) were removed. The residual 198

bands cover the entire spectrum from 426 to 2395 nm therefore, the Hyperion bands sensitive to water absorption (i.e., bands 120–132, 165–182, 185–187, and 221–224) were removed in order to reduce the influence of atmospheric scattering and water vapour absorption caused by mixed gasses to the data.[11] Bands 77 and 78 were also eliminated as such bands had a low signal to noise value, and overlapped with bands 56 and band 57, respectively.[12]
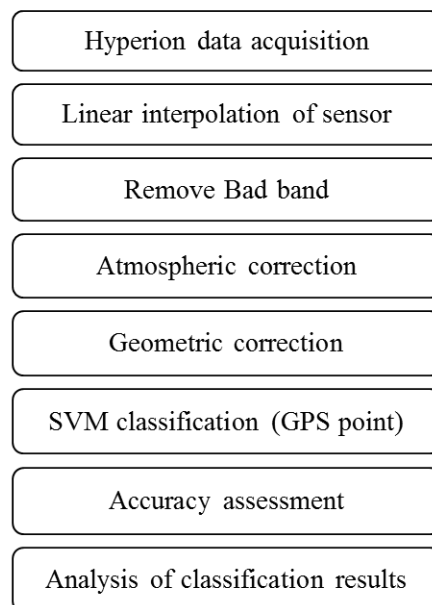
Figure 2. A flow diagram showing the processing scheme for the methodology.

Atmospheric correction

Remote sensing measurements of the Earth's surface are deeply influenced by atmosphere. Water vapour with smaller contributions from carbon dioxide, ozone and other gases dominates the absorption by atmospheric gases. To retrieve the surface reflection, the atmospheric components must be removed. In the study area, ENVI's Fast Line-of-sight Atmospheric Analysis of Spectral Hyper-cubes (FLAASH) module was applied on Hyperion data for atmospheric correction. The different parameters used in FLAASH atmospheric correction are contained in (Table 1).

Table1. Parameters used in FLAASH Atmospheric Correction

Parameter	Value
Latitude	30 29 23.28
Longitude	32 23 51.35
Sensor Altitude (km)	705
Ground Elevation (km)	0.050
Pixel Size (m)	30
Flight Date	1/9/2016
Flight Time	6:48:6
Atmospheric Model	Mid-Latitude Winter
Aerosol Model	Rural
Spectral Polishing	9 bands
CO2 Mixing Ration (ppm)	390
Zenith Angle	180
Azimuth Angle	132 57 21.96
Output Scale Factor	10000

FLAASH requires input image in BIL format and ASCII file of scale factors number. The scale factors for the VNIR and SWIR bands are 400 and 800 respectively in the case of nanometers (nm) while 40 and 80 for μm. The study area is rural and it located in winter climate. So, Mid-Latitude Winter atmospheric and rural aerosol model of FLAASH were selected and other parameters were defined based on metadata of the Hyperion image file. The change in the spectral reflectance curve of vegetation area before and after FLAASH correction can be seen in Figure 3.
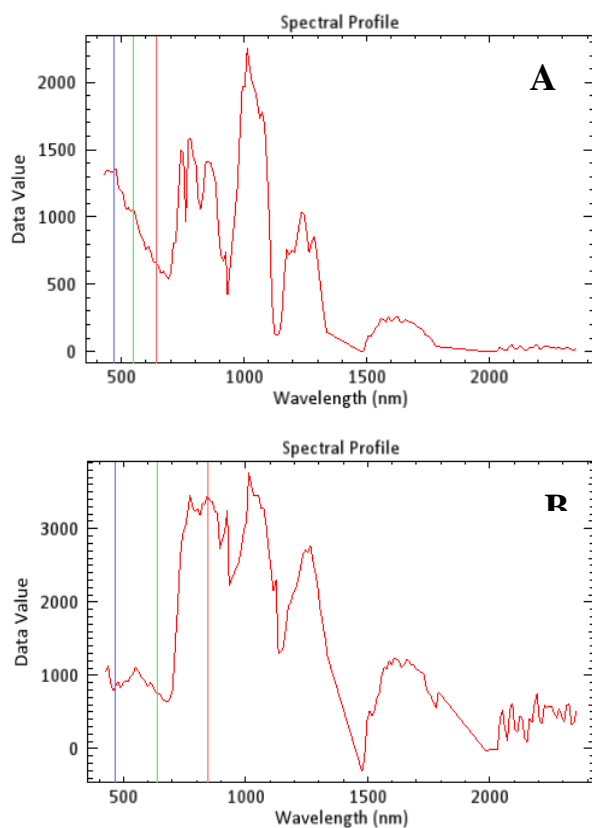
Figure 3.Spectral Curve of Vegetation (a) before FLAASH and (b) after FLAASH

Geometric correction

Geometric correction was carried out for the Hyperion image of 2016 using 40-ground control points (GCP's) obtained from a digital topographic map at a scale of 1:50,000 and Landsat ETM+ using the image- to-image technique. The geometric model used in the rectification process was three- order -polynomial and the resembling method is the nearest neighbor method.

The image was projected with Transverse Mercator projection in WGS-84 spheroid and datum. Finally, the root-mean-square error (RMSE) images were obtained as less than 0.4 pixels, which are acceptable.[13]

Support vector machine classification

Support vector machines classification (SVM) is a supervised machine learning method that performs classification based on the statistical learning.[14] Basically, SVM is based on fitting a separating hyperplane that provides the best separation between two classes in a multidimensional feature space. This hyperplane is the surface on which the optimal class separation takes place. The optimal hyperplane is the one that maximizes the distance between the hyperplane and the nearest positive and negative training. In order to represent more complex shapes than linear hyperplanes, a variety of kernels including the polynomial, the radial basis function (RBF), and the sigmoid can be used.[15] Also, a penalty parameter can be introduced to the SVM classifier to allow for misclassification during the training process.

Training data selection

It was necessary to use the training sites for the SVMs classification process which applied to the Hyperion image for land cover map. First, it has been defined for all land cover classes according to LCCS system shown in (Table 2). The classification system was based primarily on visual interpretation of the high resolution quick bird imagery acquired from Google Earth, furthermore topographic maps scale 1/ 50000. Chosen the date acquisition of the quick bird imagery was close to that of Hyperion imagery.
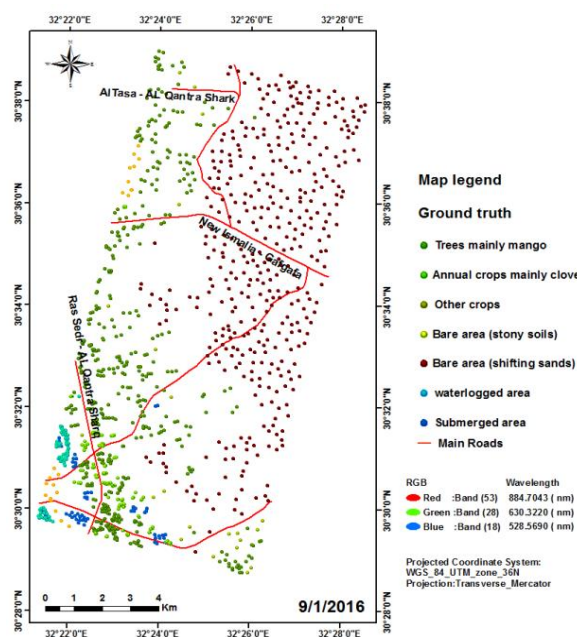
Figure 4. Training sites (GPS) for land cover classes.
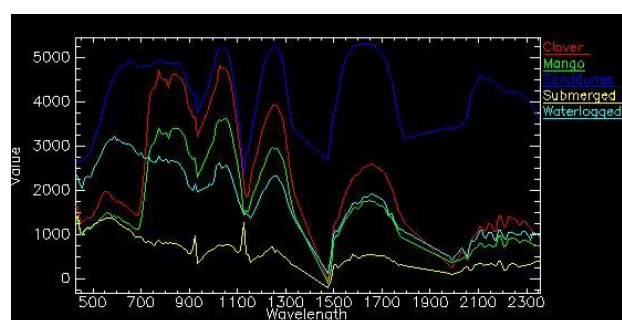
Figure 5. The component spectra for landcover classes used for SVM in test site.

Table 2. Classification key According to LCCS which was used in the land cover classes.

Class user name	LCCS code	Legend description
Permanently cropped area with surface irrigated tree crop(s) Dominant crop: fruits & mango (Mangiferaindica L.) Crop Cover: Orchard(s)	A1 = Trees A9 = Evergreen B1 = Large-Medium B5 = Continuous C1 = Single Crop D3 = Irrigated D4 = Surface D9 = Permanent S0606 = Citrus Fruits (Citrus spp.) W8 = Orchards or Other Type of Plantations	Continuous irrigated orchard of Citrus Fruits The field size varies from 2 to more than 5 fed. The class covers almost 80% of the polygon area
Permanently cropped area with small sized field(s) of surface irrigated Herbaceous crop(s) (one additional crop) (Herbaceous terrestrial crop sequentially). Dominant Crop: Clover	A3 = Herbaceous crop B2 = Small B5 = Continuous C2 = Multiple Crop C3 = 1 add. Crop C7 = Herbaceous Terrestrial C19 = Sequential D3 = Irrigated D4 = Surface D9 = Permanent Zs3 = Clover	Continuous clover crop The field size is less than 1fed. The class covers almost 80% of the polygon area
Shifting sands/Dune(s)	A2 = Unconsolidated A6 = Loose and shifting sands B1 = Dunes	Dunes
Non-perennial natural water bodies (surface aspect: sand) Scattered vegetation: scattered vegetation present	A1 = Natural Water bodies B2 = Non-Perennial B6 = Sand U1 = Scattered Vegetation	Non-perennial natural water bodies with scattered Vegetation Non-perennial natural water bodies with scattered Vegetation
Water seasonality	A23 = Waterlogged	The water table is very high and at or near the surface. These areas could be occasionally flooded but the main characteristic is the high level of the water table (e.g. bogs).

The training sites were accurately limited to include of all land cover classes. Second, training sites representative of the classes were collected from the Hyperion imagery following a stratified random sampling strategy. Third, it used for 1116 regions of interest which keeps of spectral signature from Hyperion image that has been used in SVM classification and compared it with the large spectral library of USGS are shown in (Figures 4 and 5), respectively.

Accuracy assessment

The final stage of the image classification process usually it include an accuracy assessment step.[16] Accuracy assessment is the quantification of mapping with the associate of remote sensing data, which is helpful in estimation of classification algorithms and also in limitation of the error level that might be associated with the image. The accuracy of classification is calculated in the form of an error matrix (also known as a confusion matrix).[17] Numerous methods for accuracy assessment have been explained in remote sensing. Accuracy assessment was

based on the computation of the overall accuracy (OA), user's accuracy (UA), producer's accuracy (PA), and the Kappa (Kc) statistic.[18] The OA is the ratio of the number of validation pixels that have been correctly classified to the total number of validation pixels used for all classes and is expressed as a percentage (%).

RESULTS AND DISCUSSION

Figure 6 shows the land cover thematic map produced from the SVMs classification based on the Hyperion imagery acquired for our site selection. Land cover classes were extracted: cultivated land (including mango tree and clover), sand dunes, submerged area, waterlogged area, main roads and irrigation canal. According to the table 3, the total study area is 34165 feddans, mango 9445 feddans (28%), sand dunes 22940 feddans (67 %), had the highest level of the area. In contrast, the submerged area 311feddans (1 %), clover5 47 feddans (2 %) and waterlogged area 419 feddans (1 %) had the lowest level of the area while the

main roads had 435 feddans and the irrigation canal 68 feddans. moreover,[19] studied the comparison of 2 classification methods (MLC and SVM) to extract land use and land cover in Johor Malaysia. The results showed that the SVM classification based on kappa coefficient 0.86 was the most accurate method.[20] It further concluded that SVM is better than other traditional classifiers (i.e., the ML and the SAM classifier) in respect of classification accuracy and processing time.[21] The authors evaluated various algorithms for classification in land use mapping, and concluded that the SVM algorithm in comparison with the MLC algorithms and decision trees has a higher accuracy in the preparation of land use maps.
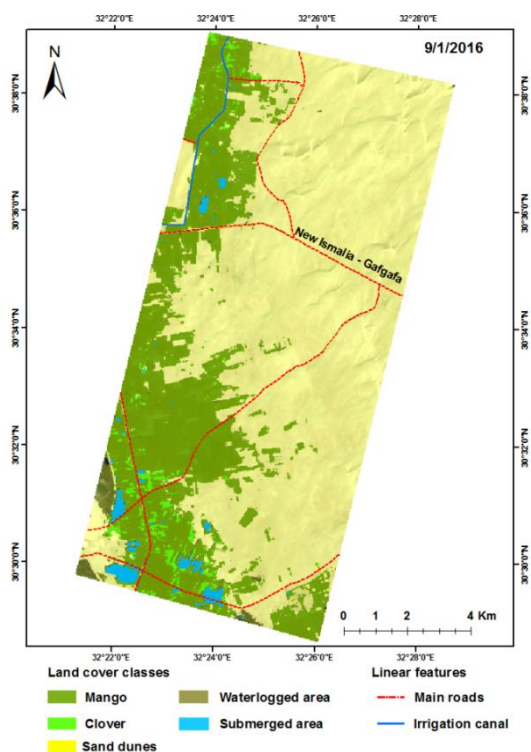
Figure 6. Land cover map for sit selection (2016) based on Hyperion image

Table 3. Land cover distribution for the study area(2016).

LC classes	Area / feddans	%
Clover	547	2%
Mango	9445	28%
Sand dunes	22940	67%
Submerged	311	1%
waterlogged	419	1%
Irrigation canal	68	0%
Main roads	435	1%
Total area	34165	100%

* Feddans = .42 hectare

Classification accuracy assessment

Classification accuracies of land cover classes using SVM classification are depicted in table 4 and table 5. A total number of 280 ground control points (GCPs) were used for accuracy assessment. 35 point of GCPs within clover, 109 point of GCPs to mango, 105 point of GCPs to sand dunes, 13 point of GCPs to submerged area and 17 point of GCPs to waterlogged area were taken. The overall classification accuracy obtained was 97.85 %. With producers and users accuracies from 92.86 % to 100 % for the individual classes, corroborating the standard accuracy of 85–90 % for land cover mapping studies as has been reported earlier.[22] The overall result showed that SVM classification process employed has got very promising potential to discriminate crops and tree classes, with high classification accuracies, when combined with high spectral resolution hyperspectral remote sensing data. The high accuracy produced by the SVM classifier may be due to the ability of the algorithm to identify the optimally separating hyperplanes for classes in comparison to other pixel-based techniques (e.g., artificial neural networks)[14] which may not be able to find such optimal hyperplanes.

Table 4. Confusion matrix for the land covers classification for the study area.

LC classes	Cl	Ma	Sa	Su	wa	Total
Unclassified	0	0	1	0	0	1
Clover	34	1	0	0	0	35
Mango	1	108	0	0	0	109
Sand dunes	0	2	103	0	0	105
Submerged	0	0	0	13	0	13
waterlogged	0	0	0	1	16	17
Total	35	111	104	14	16	280

CL=clover, Ma= Mango, Sa= sand dunes, Su= submerged, Wa= waterlogged

$$Accuracy_{Total} = \frac{38 + 108 + 1103 + 13 + 16}{280} * 100 = 97.85\ \%$$

Table 5. Accuracy totals for the classified images.

LC Classes	Producers Accuracy	Users Accuracy
Clover	97.14%	97.14%
Mango	97.30%	99.08%
Sand dunes	99.04%	98.10%
Submerged	92.86%	100.00%
waterlogged	100%	94.12%

Overall classification accuracy = 97.85 %

CONCLUSIONS

The aim of this research is to produce a land cover map for east Suez Canal area using hyperspectral data acquired by the EO-1 Hyperion instrument in conjunction with the support vector machines (SVM) classification techniques. SVM has a good generalization potentiality which stems from the selection of the hyperplane that maximizes the geometric margin between classes which helped to discriminate between the classes of land cover and various

special types of plants. The result showed that SVM classification process has got high classification accuracies, when combined with high spectral resolution hyperspectral remote sensing data. More research will be done to improving the classification accuracy and reducing the calculation time.

REFERENCES

[1] Kavzoglu, T., Colkesen, I., *Int. J. Appl. Earth Obs. Geoinf.,* **2009**, *11(5),*352-359.https://doi.org/10.1016/j.jag.2009.06.002

[2] Castillejo-González, I. L., López-Granados, F., García-Ferrer, A., Peña-Barragán, J. M., Jurado-Expósito, M., de la Orden, M. S., González-Audicana, M., *Comput. Electron. Agr.* **2009,** *68, 2,* 207-215. Doi:10.1016/j.compag.2009.06.004

[3] Chintan, A. S., Arora, M. K., Pramod, K.V., *Int. J. Remote Sens.*, **2004,***25,*481–487. doi.org/10.1080/014311603100001618040

[4] Mathur, A., Foody, G. M., *Int. J. Remote Sens.,* **2008**, *29(8),*2227-2240. http://dx.doi.org/10.1080/01431160701395203

[5] Borak, J.S., Strahler, A.H., *Int. J. Remote Sens.,* **1999**, *20,* 919–938. http://dx.doi.org/10.1080/014311699212993

[6] Lu, D., Weng, Q., *Int. J. Remote Sens.,* **2007,***28, 5,* 823–870. http://dx.doi.org/10.1080/01431160600746456

[7] Xu, D.Q., Ni, G.Q., Jiang, L.L., Shen, Y.T., Li, T., Ge, S.L., Shu, X.B., *ASR.,* **2008**, *411,*1800–1817. https://doi.org/10.1016/j.asr.2007.05.073

[8] Dalponte, M., Bruzzone, L., Vescovo, L., Gianelle, D., *Remote Sens Environ.,* **2009**, *113(11),* 2345-2355. https://doi.org/10.1016/j.rse.2009.06.013

[9] USGS, **2006**, EO1 User's Guide. http://eo1.usgs.gov

[10] Galvão, L. S., Formaggio, A. R., Tisot, D. A., *Remote Sens Environ.,* **2005**, *94(4),*523-534. https://doi.org/10.1016/j.rse.2004.11.012

[11] Beck, R., *EO-1 user guide, version 2.3*, Satellite Systems Branch, USGS Earth Resources Observation Systems Data Center (EDC).**2003**.

[12] Datt, B., McVicar, T. R., Van Niel, T. G., Jupp, D. L., Pearlman, *IEEE Trans. Geo. Sci. Rem. Sens.,* **2003**,*41(6),*1246-1259. https://doi.org/10.1109/TGRS.2003.813206

[13] Tucker, C. J., Grant, D. M., Dykstra, J. D., *Eng. Rem. Sens.,* **2004**,*70(3),*313-322. https://doi.org/10.14358/PERS.70.3.313

[14] Licciardi, G., Pacifici, F., Tuia, D., Prasad, S., West, T., Giacco, F., Gamba, P., *IEEE Trans. Geosci. Remote Sens.* **2009**. *47 (11),* 3857-3865. https://doi.org/10.1109/TGRS.2009.2029340

[15] Fauvel, M., Benediktsson, A., Chanussot, J., Sveinsson, IEEE Trans. Geosci. Remote Sens. **2008**, *46(11),* 3804–3814. https://doi.org/10.1109/ICASSP.2006.1660467

[16] Patil, M. B., Desai, C. G., Umrikar, B. N., *Int. J. Geol. Earth Environ. Sci.,* **2012**, *2,* 189-196. [17] Congalton, R. G., *RSE.,* **1991**, *37(1),* 35-46.https://doi.org/10.1016/0034-4257(91)90048-B

[18] Congalton, R. G., Green, K., *Assessing the accuracy of remotely sensed data: Principles and applications*, *CRC* press.**1999**, 137.

[19] Deilmai, B. R., Ahmad, B. B., Zabihi, H., *IOP Conf. Ser. Earth Environ. Sci.,* **2014**.*20, (1),* 012052. Doi:10.1088/issn.1755-1315

[20] Moughal, T. A., *J. Phys. Conf. Ser.,* **2013**, *439,* 012042 Doi:10.1088/issn.1742-6596

[21] Otukei, J. R., Blaschke, T., *Int. J. Appl. Earth Observ. Geoinform.* **2010**, *12,*S27-S31. https://doi.org/10.1016/j.jag.2009.11.002

[22] Anderson, J. R., *A land use and land cover classification system for use with remote sensor data*, US Government Printing Office, **1976**, 964.

SELECTION OF OPTIMAL HYPERSPECTRAL VEGETATION INDICES FOR ESTIMATING CHLOROPHYLL CONTENT OF SOME PLANT SPECIES

Ghada Khdery,*[a] Sayed Arafat,[a] Mohamed Aboelghar,[a] Mohamed Tantawy,[b] Maged Abou-El-Enain[c] and Usama Kamal[b]

Keywords: Hyperspectral; Spectral indices; Chlorophyll content.

Remote sensing enables for cost-effective, timely efficient and multi-temporal monitoring of natural vegetation. Spectral reflectance pattern either in forms of row reflectance values or form of spectral vegetation indices (SVIs) could be used as estimators of plant biophysical and biochemical parameters through statistical models. The main objective of the current study is to correlate plant chlorophyll concentration with different (SVIs) and to identify the most sufficient index to discriminate among the twenty common natural vegetation species in Sinai Peninsula. Calculated values of five hyperspectral vegetation indices (normalized difference vegetation index (NDVI); Chlorophyll Index; Chlorophyll a,b; Simple ratio index (SRI); Modified chlorophyll absorption ratio index (MCARI) for the twenty observed vegetation species were used as spectral factors in the modeling process. The result showed that the relatively high chlorophyll content was found in broad leaves plants when needle-leaved plant species showed relatively low ones. Laboratory chlorophyll estimation indicated that Asclepias sinaica had the highest chlorophyll content (79 mg cm^{-2}) when the same plant specious showed the highest chlorophyll index value. It was found that plants of family *Zygophyllaceae* have low chlorophyll content. Among observed SVIs, NDVI was the most correlated index with chlorophyll. At the same time, it was the optimal index to differentiate the different species.

* Corresponding Authors
    Fax: 26225832
    E-Mail: ghada.ali@narss.sci.eg
[a]   National Authority for Remote sensing and Space Sciences (NARSS), 23, Josef Broz Tito St. Elnozha Elgedida - P.O. Box 1564 Al-Maskan Cairo, Egypt.
[b]   Botany Department, Faculty of Science, Ain Shams University, Cairo, Egypt.
[c]   Biological and Geological Sciences Department, Faculty of Education, Ain Shams University, Cairo, Egypt.

INTRODUCTION

Evolution in hyperspectral remote sensing can provide more exact information on structural and biochemical properties of plant species.[1] Most of the work on hyperspectral remote sensing of biophysical and biochemical prosperities has been achieved through the evolution of new hyperspectral indices.[2,3,4] Spectral indices are mathematical processing of spectral reflectance to promote vegetation signal.[5,6] Vegetation indices might supply new capabilities for discriminate plant species or communities that differ in vegetation structure.[7] NDVI (normalized difference vegetation index) calculation is based on the difference in canopy reflectance at red and near-infrared wavelengths.[8,9] NDVI has been used to differentiate plant species consisting of structurally featured formations, e.g., shrubland and forest (Table 1)[10,11] or phenological featured formations.[12] New hyperspectral indices that supply correlation with the biochemical properties of canopies have been developed. Several studies show that narrow band vegetation indices involving visible reflectance near 550 and 700 nm can estimate leaf chlorophyll content such as chlorophyll a and b[13] and carotenoids.[14,15] These pigments play important roles within the process of photosynthesis, and their concentrations can depend on some factors such as phenology, the degree of canopy development and type of environmental stress.[16] Spectral vegetation indices constitute a simple and restful approach to evolve information from remotely sensed data, due to their facility of use, which facilitates the processing and analysis of huge amounts of data obtained by satellite platforms.[17,18] Increasing efforts have focused on comprehension the relationships between vegetation optical properties and photosynthetic pigments concentrations within green leave tissues such as chlorophylls and carotenoids.[19,20,21]

Table 1. Uses of vegetation indices

Vegetation indices	Uses
NDVI (normalized difference vegetation index)	Used to estimate vegetation biomass, vegetation productivity, and biochemical properties.[21] Have the best correlation with leaf chlorophyll concentrations.[22]
Chlorophyll Index	Chlorophyll concentration in the leaf.
Chlorophyll a and b	Chlorophyll a and b concentration in leaf.
SRI (simple ratio index)	Used to estimate biochemical properties at the species, canopy and landscape level, reasonably predict canopy level chlorophyll content.[21]
MCARI (modified chlorophyll absorption ratio index)	Responsive to chlorophyll variation in the first place.[23]

Our objective in this study was to assess spectral indices for prediction of leaf chlorophyll content that is relatively insensitive to plant species and leaf structure variation.

MATERIAL AND METHODS

Flowering shoots of 20 plant species of wild Egyptian plants belonging to 19 genera were collected from natural habitats in Sinai Penninsula. A SPAD-502 Leaf Chlorophyll Meter (Minolta Inc.) was used to estimate the leaf chlorophyll content in each site. The chlorophyll meter (SPAD) provides a simple, quick, method for asses leaf chlorophyll content.[24] SPAD values express relative amounts of chlorophyll in leaves by measuring transmittance in the red (650 nm) and NIR (920 nm) wavelength regions. A total of 20 leaves representing each dominant species were randomly selected in each site. Chlorophyll concentration was measured 3 times at different leaf location and their SPAD readings were recorded. From the 20 individual SPAD measurements, the average was calculated according to Ref.[25] (Table 4). Field spectroradiometer was used to measure the reflection of the twenty plant species under investigation. Measurements were acquired in Visible, Near Infrared and Short Wave Infrared from 350 nm to 2500 nm with 1 nm interval output data. However, the ASD device Software interpolates the final output data with interval 1nm for all spectrum range 350 - 2500 nm (table 2). The intervals which ASD spectroradiometer is capturing the reflectance is 1.4 nm at visible and near-infrared ranges, while it is 2 nm at the shortwave infrared spectral range. The spectrum characteristics of the device are shown in Table 3. Spectral response for different targets was acquired according to ASD Spectroradiometer measurements protocol, where the reference spectral measured as radiance from a Spectralon® panel to ensure standardized environmental conditions for the reflectance measurement. Moreover, the flexibility of fiber-optic cable provides instrument adaptation for a wide range of applications. The measurements were performed by holding the pistol grip by hand. The Bare fore optic 25 degrees used for outdoor measurements resulting circular field of view with 3 cm diameter as measurements were taken at 3 cm height in nadir position (90 degrees) over the measured plants.

Table 2. The ASD field Spec 3 specifications.

Spectral range	350 - 2500 nm
Spectral resolution	3:700 nm 8.5:1400 nm 6.5:2100 nm
Sampling interval	1.4:350 - 1050 nm 2:1000 - 2500 nm

Considerations of spectroscopy measurements, ASD, field spectrometer

The sources of information pertinent to the issues affecting spectral measurements are fragmented. Further, there are no such documents or manuals that synthesize all the factors influencing spectral measurements and the methods used to minimize and account for extraneous factors in spectral measurement. Issues to be considered when designing a spectral library database have been summarized.[26] The factors that affect standardized measurements can be summarized to include: environmental conditions.

Vegetation indices and chlorophyll content

The values of VIs that calculated from spectroscopy measurements for each plant in the field, it is based on the contrast between maximum absorption of the red spectrum by chlorophyll and pigments followed by maximum reflectance in near infrared spectrum by leaf cellular structure as presented in Table 3. The correlation between five different (VIs) and chlorophyll content was observed and expressed through mathematical correlations as explained in Table 3.

Table 3. Summary of vegetation indices, algorithms and sources for vegetation indices. where R_x is the reflectance at the given wavelength (nm)

Index description	Formation	Ref.
NDVI (Normalized difference vegetation index)	$(R_{800} R_{680})/(R_{800}+R_{680})$	7
SR (Simple ratio)	R_{750}/R_{710}	27
Cab (Leaf Cab Concentration)	$(R_{750}-R_{705})/(R_{750}+R_{705})$	15
CL (Chlorophyll Index)	$[R_{750}/(R_{700} + R_{710})]-1$	15
MCARI (Modified chlorophyll absorption ratio index)	$(R_{700}-R_{670})-0.2(R_{700}-R_{550})-R_{700}/R_{670}$	23

RESULTS AND DISCUSSION

Extraction of some biophysical parameters from remote sensing data

Asclepias sinaica showed the highest chlorophyll content (79 mg cm^{-2}) followed by *Phlomis aurea* (73 mg cm^{-2}) while the lowest chlorophyll content was found in *Fagonia glutinosa* (4mg cm^{-2}). The correlation between chlorophyll content and remotely sensed data was presented in forms of vegetation indices-chlorophyll correlations as shown in the Figure 1a-1e, Table 5 and 6 and equations.

Results for the regression analysis showed that all of the vegetation indices in the present study positively correlated with the chlorophyll content as follows.

A strong correlation (R^2= 0.94) has been found between Normalized Difference Vegetation Index (NDVI) and chlorophyll Content as presented in (Figs. a) and the subsequent equation:
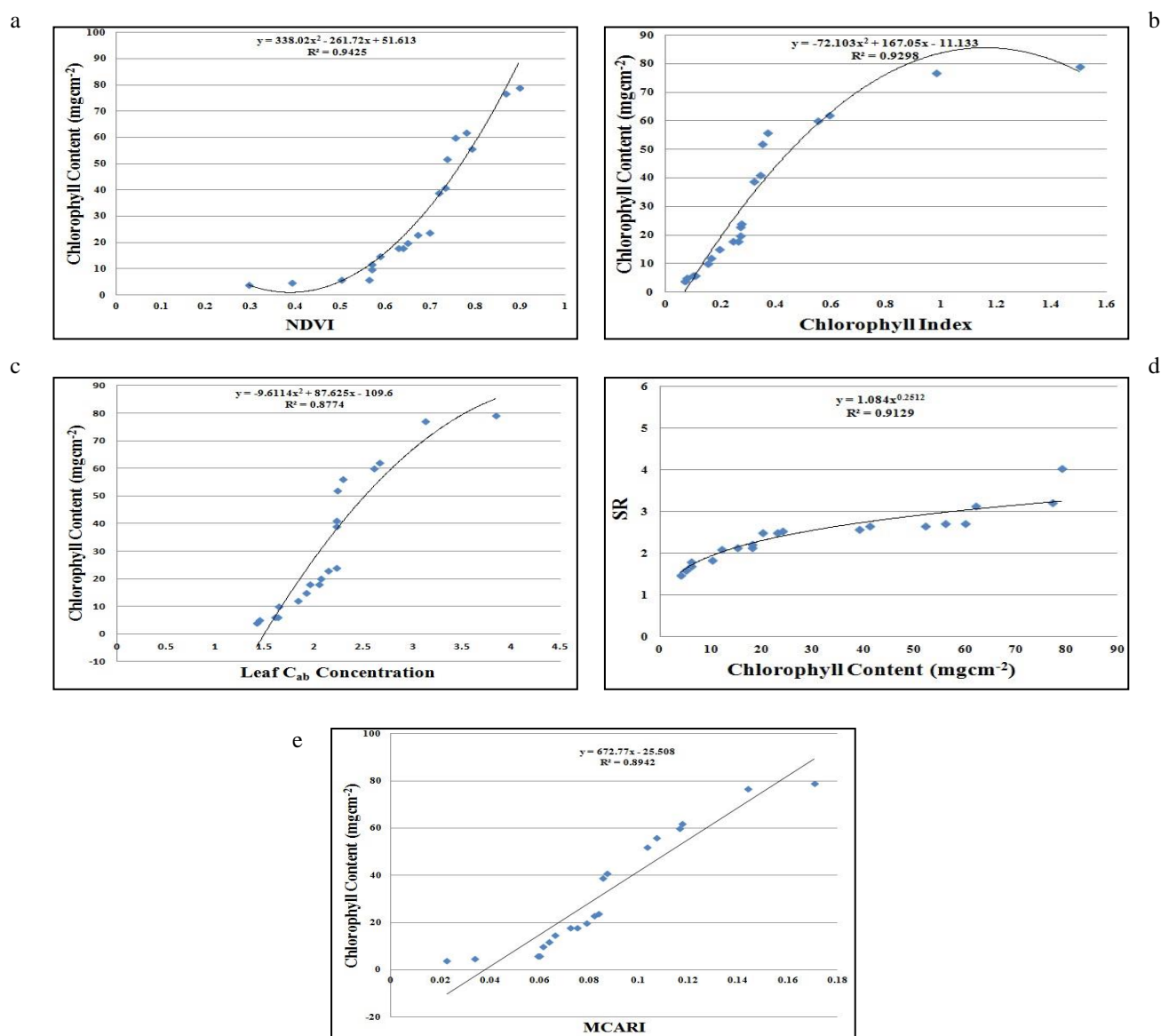
$$Y= 338.0x^2 - 261.72x - 51.613$$

A strong correlation (R^2= 0.92) was also found between Chlorophyll index and chlorophyll content as shown in (Figs. b) and the subsequent equation:

$$Y= 72.103x^2 - 167.05x - 11.133$$

A good correlation (R^2= 0.87) was observed between leaf (Cab) concentration and chlorophyll content as shown in (Figs. c) and the subsequent equation:

a

b

c

d

e

Figure 1a-e. The correlation between chlorophyll content and difference vegetation indices **a.** The relation between (NDVI) and chlorophyll content to differentiate between studied taxa, **b:** Relation between chlorophyll index and chlorophyll content, **c.** The relation between leaf C_{ab} concentration and chlorophyll content, **d.** Relation between simple ratio (SR) and chlorophyll content and **e**. Relation between (MCARI) and chlorophyll content

$$Y = 9.6114x^2 - 67.625x - 109.6$$

A strong correlation ($R^2 = 0.91$) was also found between the normalized simple ratio (SR) and chlorophyll content as shown in (Fig. 1d) and the subsequent equation:

$$Y = 1.084x^{0.2512}$$

A good correlation ($R^2 = 0.89$) was found between the modified chlorophyll absorption ratio index (MCARI) and chlorophyll content as shown in (Fig. 1e) and the subsequent equation.

$$Y = 672.77x - 25.508$$

Table 4. Chlorophyll content of studied taxa.

Plant	Chlorophyll content (mg cm^2)
Achillea fragrantissima	10
Aerva tomentosa	18
Alkanna orientalis	52
Asclepias sinaica	79
Astragalus sieberi	15
Ballota kaiseri	39
Echinops spinosus	73
Fagonia glutinosa	4
Hyoscyamus muticus	41
Matthiola arabica	23
Matthiola longipetala	24
Origanum syriacum	74

Peganum harmala	6
Phlomis aurea	77
Pyrethrum santolinoides	12
Stachys aegyptiaca	18
Teucrium polium	20
Verbascum sinaiticum	56
Zilla spinosa	6
Zygophyllum simplex	5

Table 5. Correlation coefficients between the original indices and chlorophyll content of studied taxa.

Plant	NDVI	MCARI
Fagonia glutinosa	6.973	0.0749
Peganum harmala	8.962	0.0853
Zygophyllum simplex	7.521	0.1440
Matthiola arabica	0.715	0.0614
Matthiola longipetala	5.852	0.0662
Zilla spinosa	0.499	0.0787
Achillea fragrantissima	3.891	0.0226
Echinops spinosus	5.671	0.0835
Origanum syriacum	7.772	0.1707
Pyrethrum santolinoides	7.301	0.0819
Phlomis aurea	0.647	0.0593
Stachys aegyptiaca	0.294	0.0336
Teucrium polium	6.692	0.0722
Verbascum sinaiticum	6.251	0.0871
Aerva tomentosa	0.735	0.0600
Alkanna orientalis	6.361	0.1032
Asclepias sinaica	0.561	0.1173
Astragalus sieberi	5.673	0.0637
Ballota kaiseri	7.401	0.1071
Hyoscyamus muticus	8.654	0.1165

Table 6. Spectral indices related to biochemical and biophysical vegetation parameters: NDVI, normalized difference vegetation index; MCARI and the modified chlorophyll absorption ratio index

Vegetation indices	R^2
NDVI	0.94
Chlorophyll index	0.92
Cab	0.87
SR	0.91
MCARI	0.89

Regarding chlorophyll content analysis, showed that generally, the high chlorophyll was found in these plant species with broad leaves when needle-leaved plant species showed low chlorophyll content also noticed that plant of family Zygophyllaceae has low chlorophyll content. Results for the regression analysis showed that all of the observed vegetation indices positively correlated with the chlorophyll content. It was found that Strong correlation between, NDVI and chlorophyll content ($R^2= 0.94$) and also a good correlation ($R^2= 0.91$) between simple ratio and chlorophyll

index. This agreed with Ref.[14] who reported the strong correlation between vegetation indices and chlorophyll content. High values of these indices and their strong correlation with chlorophyll content indicated the high capability of the VIs as indicators for plant status and physiological condition. The strong correlation ($R^2= 0.88$) between chlorophyll content and the calculated leaf Cab concentration also showed the method in which remote sensing tools could be used to estimate plant biophysical parameters instead of the other time consuming and costly traditional methods. This agreed with Refs.[28,29]

Table 7. Spectral indices related to biochemical and biophysical vegetation parameters: SR, simple ratio; Cab, Chlorophyll a, b.

Plant	Chloro-phyll Index	Leaf Cab Concen-t-ration	SR
Fagonia glutinosa	0.319	2.223	0.319
Peganum harmala	0.368	3.836	2.576
Zygophyllum simplex	0.241	2.046	4.033
Matthiola arabica	0.550	2.602	2.498
Matthiola longipetala	0.104	1.947	2.510
Zilla spinosa	0.0986	1.621	3.2296
Achillea fragrantissima	0.151	1.595	1.480
Echinops spinosus	0.0736	1.635	2.539
Origanum syriacum	0.162	2.058	0.162
Pyrethrum santolinoides	0.346	2.284	2.667
Phlomis aurea	0.339	2.233	2.655
Stachys aegyptiaca	0.260	1.416	2.713
Teucrium polium	0.267	2.132	2.721
Verbascum sinaiticum	0.2732	2.221	3.149
Aerva tomentosa	0.590	2.654	1.599
Alkanna orientalis	1.498	1.829	1.704
Asclepias sinaica	0.191	1.439	1.804
Astragalus sieberi	0.069	1.909	1.849
Ballota kaiseri	0.267	2.215	2.104
Hyoscyamus muticus	0.979	3.120	2.147

CONCLUSION

The result showed that Normalized Difference Vegetation Index (NDVI) was the most correlated index to chlorophyll content. Also, it was the optimal vegetation index to differentiate among the different species. It was found that plants of family Zygophyllaceae have low chlorophyll content as also indicated by chlorophyll spectral index. The study showed high compatibility between spectral index and biochemical parameters of the natural vegetation. The study succeeded in generating statistical correlation to retrieve chlorophyll from spectral reflectance data with high accuracy.

REFERENCES

[1]Blackburn**, G. A.**, Spectral indices for estimating photosynthetic pigment concentrations: A test using senescent tree leaves. *Int. J. Remote Sensing*, **1998**, *19(4),* 657–675. DOI:10.1080/014311698215919

[2]Chappelle, E. W., Kim, M. S., Murtrey, M. C., Ratio analysis of reflectance spectra (RARS): An algorithm for the remote estimation of the concentrations of chlorophyll A, chlorophyll B, and carotenoids in soybean leaves. *Remote Sensing Environ.*, **1992,** *39(3),* 239-247. DOI:10.1016/0034-4257(92)90089-3

[3]Carter, G. A., Ratios of leaf reflectances in narrow wavebands as indicators of plant stress. *Int. J. Remote Sensing*, **1994,** *15:* 697–703. DOI:10.1080/01431169408954109

[4]Gitelson, A., Merzlyak, M., Remote Estimation of Chlorophyll Content in higher Plant Leaves. *Int. J. Remote Sensing,* **1997**, *18(12),* 291-298. DOI:10.1080/014311697217558

[5]Huete, A. R., Jackson, R. D., Soil and atmosphere influences on the spectra of partial canopies. *Remote Sensing Environ.,* **1988**, *25(1),* 89-105. DOI: 10.1016/0034-4257(95)00034-X

[6]Qi, J., Moran, M. S., Cabot, F., Dedieu, G., Normalization of sun/view angle effects using spectral albedo-based vegetation indices. *Remote Sensing Environ.,* **1995** *52(3),* 207-217. DOI: 10.1016/0034-4257(95)00034-X

[7]Nagendra, H., Benefits of hyperspectral remote sensing for tracking plant invasions. *Diversity and Distributions*, **2011,** *17*, 381–392.

[8]Rouse, J. W, Haas, R. H, Schell, J. A., Deering, D.W., Harlan, J. C., Monitoring the Vernal Advancement of Retrogradation of Natural Vegetation. NASA/GSFC, Type III, *Final Report, Greenbelt, MD*, **1974**

[9]Tucker, C. J., Garrett, M. W., Leaf optical system modeled as a stochastic process. *Appl. Optics*, **1977,** *16,* 1151–1157. DOI:10.1364/AO.16.000635

[10]Achard, F., Estreguil, C., Forest classification of South East Asia using NOAA AVHRR data. *Remote Sensing Environ.,* **1995**, *54,* 198-208. DOI: 10.1016/0034-4257(95)00153-0

[11]Saney, G. B., Elliott, R. L., Capacity of AVHRR data in discriminating rangeland cover mixtures. *Int. J. Remote Sensing*, **2002**, *23,* 299-312.

[12]Van Wagtendonk, J. W., Root, R. R, The use of multitemporal normalized difference vegetation index (NDVI) data for mapping fuel models in Yosemite National Park, USA. *Int. J. Remote Sensing,* **2003,** *24,* 1639-1651. DOI:10.1603/0022-2585(2005)042[0075

[13]Gitelson, A. A., Merzlyak, M. N., Signature analysis of leaf reflectance spectra: Algorithm development for remote sensing of chlorophyll. *J. Plant Physiol.,* **1997,** *148,* 494-500 DOI: 10.1046/j.1469-8137.1999.00424.

[14]Gamon, J. A., Surfus, J. S., Assessing leaf pigment content and activity with a reflectometer. *New Phytol.,* **1999,** *143,* 105-117. 494-500 DOI: 10.1046/j.1469-8137.1999.00424.x

[15]Gitelson, A. A.; Zur Y.; Chivkunova, O. B. , Merzlyak, M. N., Assessing carotenoid content in plant leaves with reflectance spectroscopy. *Photochem. Photobiol.,* **2002**, *75,* 272-281.DOI:10.1562/0031-8655(2002)075

[16]Blackburn, G. A., Pitman, J. I., Biophysical controls on the directional spectral reflectance properties of bracken (Pteridium aquilinum) canopies: results of a field experiment. *Int. J. Remote Sensing*, **1999,** *20(11),* 2265-2282. DOI:10.1080/014311699212245

[17]Govaerts, Y. M., Verstraete, M. M; Pinty, B., Gobron, N., Designing optimal spectral indices: feasibility and proof of concept study. *Int. J. Remote Sensing*, **1999**, *20(9),* 1853-1873. DOI.10.1080/014311699212524

[18]Myneni, R. B.; Hall, F. G.; Sellers, P. J., Marshak, A. L., The meaning of spectral vegetation indices. *IEEE Trans. Geosci. Remote Sensing*, **1995**, *33,* 481 – 486.

[19]Demarez, V., Gastellu-Etchegorry, J. P., A modeling approach for studying forest chlorophyll content. *Remote Sensing Environ.*, **2000**, *71,* 226–238. DOI: 10.1016/S0034-4257(99)00089-9

[20]Zarco-Tejada, P. J., Miller, J. R., Noland, T. L., Mohammed, G. H., Sampson, P. H., Scaling-up and model inversion methods with narrow-band optical indices for chlorophyll content estimation in closed forest canopies with hyperspectral data. *IEEE Trans. Geosci. Remote Sensing*, **2001**, *39,* 1491–1507. DOI: 10.1109/36.934080

[21]Sims, D. A., Gamon, J. A., Relationships between leaf pigment content and spectral reflectance across a wide range of species, leaf structures and developmental stages. *Remote Sensing Environ.*, **2002**, *81,* 337–354. DOI: 10.1016/S0034-4257(02)00010

[22]Gu, Y., Brown, J. F., Verdin, J. P., Wardlow, B., A five-year analysis of MODIS NDVI and NDWI for grassland drought assessment over the central Great Plains of the United States, *Geophys. Res. Lett.,* **2007**, *34,* L06407. DOI: 10.1029/2006GL029127.

[23]Daughtry, C. S. T., Walthall, C. L., Kim, M. S., Brown de Colstoun, E., McMurtrey III, J. E., Estimating corn leaf chlorophyll concentration from leaf and canopy reflectance. *Remote Sensing Environ.,* **2000,** *74,* 229–239. DOI: 10.1016/S0034-4257(00)00113

[24]Minolta, Chlorophyll meter SPAD-502. Instruction Manual, Minolta Camera BeNeLux BV. Maarssen, The Netherlands, **2003.**

[25]Nakano, M., Nomizu, T., Mizunashi, K., Suzuki, M.,Mori, S., Kuwayama, S., Hayashi, M., Umehara, H., Oka, E., Kobayashi, H., Asano, M., Sugawara, S., Takagi, H., Saito, H., Nakata, M., Godo, T., Hara, Y. and Amano, J., Somaclonal variation in Tricyrtis hirta plants regenerated from 1-year-old embryogenic callus cultures. *Scientia Horticult.,* **2006**, *110(4),* 366–371. DOI: 10.1016/j.scienta.2006.07.026

[26]Pfitzner, K., Field-based spectroscopy – do we need it? *North Australian Remote Sensing and GIS Conference* (NARGIS), **2005**, July 4–7 2005, Charles Darwin University, Darwin.

[27]Slater, P. N., Jackson, R. D., Atmospheric effects on radiation reflected from soil and vegetation as measured by orbit sensors using various scanning directions. *Appl. Optics*, **1982,** *21,* 3923. DOI: 10.1364/AO.21.003923

[28]Demarez, V., Gastellu-Etchegorry, J. P., A modeling approach for studying forest chlorophyll content. *Remote Sensing Environ.*, **2000**, *71,* 226–238. DOI: 10.1016/S0034-4257(99)00089-9

[29]Zarco-Tejada, P. J., Miller, J. R., Morales, A., Berjon, A., Aguera, J., Hyperspectral indices and model simulation for chlorophyll estimation in open-canopy tree crops. *Remote Sensing Environ.*, **2004**, *90,* 463–476. DOI:10.1016/j.rse.2004.01.017 ·